An investigation of mechanics in nanomachining of Gallium Arsenide

Pengfei Fan

A thesis submitted for the degree of Doctor of Philosophy

Centre for Precision Manufacturing

Department of Design, Manufacturing and Engineering Management

University of Strathclyde

May 2021

Declaration Statement

This thesis is the result of the author’s original research. It has been composed by the author and has not been previously submitted for examination which has led to the award of a degree.

The copyright of this thesis belongs to the author under the terms of the United Kingdom Copyright Acts as qualified by University of Strathclyde Regulation 3.50. Due acknowledgement must always be made of the use of any material contained in, or derived from, this thesis.

Signed:

Date:

Abstract

The first two decades of the 21st Century have seen a wide exploitation of Gallium Arsenide (GaAs) in photoemitter device, microwave devices, hall element, solar cell, wireless communication as well as quantum computation device due to its superior material properties, such as higher temperature resistance, higher electronic mobility and energy gap that outperforms silicon. Ultra-precision multiplex two dimensional (2D) or three dimensional (3D) free-form nanostructures are often required on GaAs-based devices, such as radio frequency power amplifiers and switches used in the 5G smart mobile wireless communication. However, GaAs is extremely difficult to machine as its elastic modulus, Knoop hardness and fracture toughness are lower than other semiconductor materials such as silicon and germanium. This PhD thesis investigated the mechanics of nanomachining of GaAs through molecular dynamics (MD) simulation combined with single point diamond turning (SPDT) and atomic force microscope (AFM) based experimental characterization in order to realise ductile-regime nanomachining of GaAs, which is the most important motivation behind this thesis. The investigation of mechanics of nanomachining of GaAs included studies on cutting temperature, cutting forces, origin ductile plasticity, atomic scale friction, formation mechanism of sub-surface damage, wear mechanism of diamond cutting tool. Machinability of GaAs at elevated temperature was also studied in order to develop thermally-assisted nanomachining process in the future to facilitate plastic material deformation and removal. This thesis contributed to address the knowledge gaps such as what is the incipient plasticity, how does the sub-surface damage form and how does the diamond cutting tool wear during nanomachining of GaAs.

Firstly, this thesis investigated the cutting zone temperature, cutting forces and origin of plasticity of GaAs material, including single crystal GaAs and polycrystalline GaAs during SPDT process. The experimental and MD simulation study showed GaAs has a strong anisotropic machinability. The simulation results indicated that the deformation of polycrystalline GaAs is accompanied by dislocation nucleation in the grain boundaries (GBs) leading to the initiation of plastic deformation. Furthermore, the 1/2<110> is the main type of dislocation responsible for ductile plasticity in polycrystalline GaAs. A phenomenon of fluctuation from wave crests to wave troughs in the cutting forces was only observed during cutting of polycrystalline GaAs, not for single-crystal GaAs.

Secondly, this thesis studied the atomic scale friction during AFM-based nanomachining process. a strong size effect was observed when the scratch depths are below 2 nm in MD simulations and 15 nm from the AFM experiments respectively. A strong quantitative corroboration was obtained between the MD simulations and the AFM experiments in the specific scratch energy and more qualitative corroboration with the pile up and the kinetic coefficient of friction. This conclusion suggested that the specific scratch energy is insensitive to the tool geometry and the speed of scratch used in this investigation but the pile up and kinetic coefficient of friction are dependent on the geometry of the tool tip.

Thirdly, this thesis investigated formation mechanism of sub-surface damage and wear mechanism of diamond cutting tool during nanomachining of GaAs. Transmission Electron Microscope (TEM) measurement of sub-surface of machined nanogrooves on GaAs and MD simulation of dislocation movement indicated the dual slip mechanisms i.e. shuffle-set slip mechanism and glide-set slip mechanism, and the creation of dislocation loops, multi dislocation nodes, and dislocation junctions governed the formation mechanism of sub-surface damage of GaAs during nanomachining process. Elastic-plastic deformation at the apex of the diamond tip was observed in MD simulations. Meanwhile, a transition of the diamond tip from its initial cubic diamond lattice structure sp3 hybridization to graphite lattice structure sp2 hybridization was revealed. Graphitization was, therefore, found to be the dominant wear mechanism of the diamond tip during nanometric cutting of single crystal GaAs.

Finally, in MD simulations study of cutting performance at elevated temperature, hotter conditions resulted in the reduction of cutting forces by 25% however, the kinetic coefficient of friction went up by about 8%. While material removal rate was found to increase with the increase of the substrate temperature, it was accompanied by an increase of the sub-surface damage in the substrate. Moreover, a phenomenon of chip densification was found to occur during hot cutting which referred to the fact that the amorphous cutting chips obtained from cutting at low temperature will have lower density than the chips obtained from cutting at higher temperatures.

Acknowledgments

First and foremost, I wish to express my extremely grateful to my primary supervisor, Professor Xichun Luo, who has been inspiring me with his invaluable expertise since my first set foot in nanomanufacturing research. His insightful feedback pushed me to sharpen my thinking and brought my work to a higher level. I could not have completed this dissertation without the continuous support of him. I also would like to express my immense appreciation to my co-supervisor, Dr. Saurav Goel, who is a great thinker and has made plentiful suggestions at each step of my work. I also wish to thank my co-supervisor, Professor Yi Qin, for his support and valuable suggestions.

I would also like to acknowledge Professor Yongda Yan and Professor Yanquan Geng from HIT in China for their valuable supports, giving me access to their laboratory facilities and providing me accommodations during the epidemic situation. I am thankful to Dr. Yang He, Mr. Yuzhang Wang, Mr. Zhuo Fang, Mr. Jiqiang Wang, Mr. Zihan Li for their suggestions on my research work in HIT.

My keen appreciation also goes to the friends and colleagues Dr. Wenlong Chang, Dr. Yukui Cai, Dr. Wenbin Zhong, Dr. Fei Ding, Mr. Zhengjian Wang, Mr. Jian Gao as well as all members of the Centre for Precision Manufacturing for their kind hospitality and help.

I also extend my sincere thanks to Dr. Vitor Magueijo, Dr. Simon Shilton, Dr. Jun Li, Dr. Wenhan Cao and Mr. Jixiang Zhang from Chemical Process Engineering Department, University of Strathclyde for their generous support during my life in Glasgow.

Finally, words would be few to express my gratitude towards my parents and parents-in-law for their endless patience, understanding and support in my growth. In addition, I must thank my beloved wife, Dr. Hui Mao. She makes me feel like the luckiest man in the world every single day and raises me up to more than I can be. I also need to thank my sweet heart, Yunjia Fan, who supply happy distractions to rest my mind outside of my research.

List of Publications

Journal papers:

1. **Fan P.,** Ding F., Luo X., Yan Y., Geng Y., and Wang Y., ‘A Simulated Investigation of Ductile Response of GaAs in Single-Point Diamond Turning and Experimental Validation,’ *Nanomanufacturing and Metrology*, (2019).

2. **Fan P.,** Goel S., Luo X., Yan Y., Geng Y., and Wang Y., ‘An atomistic investigation on the wear of diamond during atomic force microscope tip-based nanomachining of gallium arsenide,’ *Computational Materials Science*, (2020).

3. **Fan P.,** Goel S., Luo X., Yan Y., Geng Y., and He Y., ‘Origins of ductile plasticity in a polycrystalline gallium arsenide during scratching: MD simulation study,’ *Applied Surface Science*, (2021).

4. **Fan P.,** Goel S., Luo X., Yan Y., Geng Y., He Y., and Wang Y., ‘Molecular dynamics simulation of AFM tip-based hot scratching of nanocrystalline GaAs,’ *Materials Science in Semiconductor Processing*, (2021).

5. **Fan P.,** Goel S., Luo X., and Upadhyaya H., ‘Atomic scale friction studies on single crystal GaAs using AFM and molecular dynamics simulation,’ *Nanomanufacturing and Metrology*, (2021).

6. Wang J., Yan Y., Li Z., Geng Y., Luo X., and **Fan P.,** ‘Processing outcomes of atomic force microscope tip-based nanomilling with different trajectories on single-crystal silicon,’ *Precision Engineering*, (2021).

7. Wang J., Geng Y., Li Z., Yan Y., Luo X., and **Fan P.,** ‘Study on the vertical ultrasonic vibration-assisted nanomachining process on single-crystal silicon,’ *Journal of Manufacturing Science and Engineering (ASME)*, (2021).

Conference papers:

1. **Fan P.,** and Luo X., ‘Scanning Probe Lithography (SPL) Nanofabrication Approach,’ In: 24th International Conference on Automation & Computing (ICAC), Newcastle, 2018 (**Best Paper Award**).

2. **Fan P.,** Fan D., Goel S., and Luo X., ‘Molecular dynamics simulation of AFM tip-based nanoscratching of multi-layer graphene,’ In: Proceedings of the 21st EUSPEN International Conference, Copenhagen, 2020. (**HEIDENHAIN Award**).

Table of Contents

List of Tables

List of Figures

Nomenclature

E	System total energy
V_{ij}	Bond energy
f_C	Smooth cutoff function
f_R	Two-body term
r_{ij}	Length function of the i and j bond
b_{ij}	Bond order term
f_A	Attractive pair potential
δ_{ij}	Atom number
θ	Bond angle and inclination angle
$\varphi_{ij}(r_{ij})$	Repulsive energy
$\beta_{\sigma,ij}(r_{ij})$	Bond integrals
$\theta_{\sigma,ij}$	Specific bond-orders
U_{prom}	Promotion energy
ϵ_0	Electrical permittivity of vacuum
e	Electron charge
Z_i	Nuclear charges of atom *i*
$S(r_{ij})$	Switching function
$K.E.$	Kinetic energy
N	Atoms quantity
K_b	Boltzamn constant
ρ	Dislocation density

L	Total length of dislocation lines
V	Volume of workpiece
F_x	Lateral force
F_y	Normal force
e_c	Specific cutting energy
R	Resultant force
b	Width of cut
t	Depth of cut
η_i	Green-Lagrangian strain tensor matrix
J_i	Local deformation gradient tensor matrix
I	Initial gradient tensor matrix
η_{ij}	Six gradient tensor components
r	Chip ratio
r_0	GSP reference radius
r_c	GSP characteristic radius
m	GSP attractive exponent
n	GSP repulsive exponent
n_c	GSP decay exponent
r_l	Spline start radius
r_{cut}	Spline cutoff radius
φ_0	Repulsive energy prefactor
$\beta_{\sigma,0}$	σ bond integral prefactor
$\beta_{\pi,0}$	π bond integral prefactor

c_σ	Empirical θ_σ parameter
c_π	Empirical θ_π parameter
K_N	Spring constant

Abbreviations

AFM	Atomic Force Microscope
ACSM	Atomic and close-to-atomic scale manufacturing
SPDT	Single Point Diamond Turning
GaAs	Gallium arsenide
BDT	Brittle-ductile transition
DXA	Dislocation extraction algorithm
MD	Molecular dynamics
PC	Polycrystalline
SC	Single Crystal
SEM	Scanning Electron Microscope
LAMMPS	Large-scale Atomic/Molecular Massively Parallel Simulator
GB	Grain Boundary
BOP	Bond Order Potential
FIB	Focused Ion Beam
HPC	High Performance Computer
NVE	Microcanonical Ensemble
OVITO	Open Visualization Tool
SSD	Sub-surface Damage
COF	Coefficient of Friction
STM	Scanning Tunneling Microscope
SPM	Scanning Probe Microscope
SPL	Scanning Probe Lithography

MFM	Magnetic Force Microscopy
EFM	Electrostatic Force Microscopy
PFM	Piezoresponse Force Microscopy
EBL	Electron Beam Lithography
FIB	Focused Ion Beam
NIL	Nanoimprint Lithography
O-SPL	Oxidation- Scanning Probe Lithography
t-SPL	Thermal-Scanning Probe Lithography
tc-SPL	Thermochemical-Scanning Probe Lithography
PMMA	Polymethyl Methacrylate
D-SPL	Dip-pen Scanning Probe Lithography
B-SPL	Bias induced-Scanning Probe Lithography
M-SPL	Mechanical-Scanning Probe Lithography
ASI	Artificial Spin Ices
TB-EBID	Tip-based Electron Beam Induced Deposition
PDMS	Polydimethylsiloxane
MOSFET	Metal-oxide-semiconductor Field-effect transistor
FinFET	Fin Field-effect Transistor
SET	Single Electron Transistor
RT	Room Temperature
β-SiC	Cubic Silicon Carbide
SiC	Silicon Carbide
MODFET	Modulation-doped Field effect transistor
ZBL	Ziegler-Biersack-Littmark

CAT	Crystal Analysis Tool
ZB	Zinc Blende
Amp	Amorphous
HD	Hexagonal Diamond
SF	Stacking Faults
HRTEM	High Resolution Transmission Electron Microscopy
OBCDS	Oblique Cutting with Double Sides
OBCSS	Oblique Cutting with Single Side
ORC	Orthogonal Cutting
ISF	Intrinsic Stacking Fault
EUV	Extreme Ultraviolet

Chapter 1　Introduction

1.1　Background

Recently, 5th generation mobile networks (5G) technology is rolling out globally and is seen as one of the key enabling technologies to deliver a new era of VR (Virtual Reality)/AR (Augmented Reality), connecting virtually everyone and everything together including machines, objects, and devices [1]. As reported by a landmark 5G economy study, "5G effect" will support a wide variety of industries and is expected to bring promising goods and services worth up to 13.1 trillion US dollars by 2035 [2]. Only time will tell us what the full economic impact of 5G will be. The fact is, in 5G technology, the multi-Gbps peak data transmission speed (100 times than 4G technology) is required. In other words, this extremely high data transmission speed proposes new demand for the material properties of key components for the power amplifier [3], radio frequency (RF) switch [4] and low noise amplifier [5] in smart phones. This material needs to have wider band gap, higher critical breakdown electric field, higher electron saturation rate and electron mobility rate than conventional semiconductor material, i.e. silicon. Table 1.1 shows Gallium Arsenide (GaAs) has superb material properties to meet the above requirements. As a result, the demand for complex and flexible 2D or 3D nanostructures on GaAs is sharply rising.

Table 1.1 Comparison of material properties of Si and GaAs [6][7].

	Band gap (eV)	Critical breakdown electric field (MV/cm)	Electron saturation rate (10^7cm/s)	Electron mobility rate ($cm^2 \cdot V^{-1}s^{-1}$)	Elastic modulus (GPa)	Knoop hardness (kg/mm^2)	Fracture toughness ($MPa/m^{1/2}$)
Si	1.1	0.3	1.0	1350	168	1020	0.82
GaAs	1.4	0.4	2.0	8500	83	750	0.46

Table 1.1 also shows GaAs is indeed an extremely challenging highly brittle material to machine which is attributed to the much lower elastic modulus and fracture toughness than silicon. To date methods such as chemo-mechanical polishing (CMP) [8] and lapping [9] have been employed to achieve nanoscale material removal in GaAs. However, these approaches are particularly suited for planar nanostructures and are still very time-consuming [10][11]. Additionally, focused ion beam (FIB) has also been utilized to fabricate 3D hemispherical cavity on GaAs substrate [12]. However, FIB presents the risk of ion contamination to the finished machined surface. Also, FIB is not viable for mass production for future commercialization due to the low material removal rate. Extreme ultraviolet (EUV) lithography has also been employed for the fabrication of GaAs-based microelectronic devices [13]. However, this method requires very costly light source and plasma treatment or reactive ion etching to remove the residual layer of resist, which make it extremely expensive and time-consuming [14]. More recently, the method of single point diamond turning (SPDT) was used to machine GaAs as a purely mechanical method and a relatively high material removal rate was achieved [7]. SPDT is capable of mass production of 2D

and 3D nanostructures with high form accuracy in a single pass. Significantly, since the invention of the scanning probe microscopy (SPM), the scanning probe lithography (SPL) approach has widely been applied for low cost fabrication of high quality nanostructures to obtain nano/atomic scale accuracy. A mix-and-match lithography approach by combining SPL with etching techniques will be a potential hybrid technology meeting the demand of mass production in the near future. Through comparing the SPDT with SPL methods, SPDT is a candidate for manufacturing 2D/3D nanostructures in large area but the attainable nanostructures are limited by the size of diamond tool, while SPL approach can overcome this limitation.

In nanomachining of GaAs, the issues of nanometric mechanics i.e. cutting temperature, cutting forces, origin ductile plasticity, atomic scale friction, formation mechanism of sub-surface damage and wear mechanism of diamond cutting tool, are still unclear which hamper the development of ductile-regime nanomachining process to obtain satisfactory dimensional precision and surface integrity. Filling these knowledge gaps, therefore, becomes the key motivation behind this thesis. MD simulation methodology and single point diamond turning (SPDT) and scanning probe lithography (SPL) methodology are implemented to address the above knowledge gaps.

1.2 Aim and objectives

As discussed in section 1.1, the aim of this PhD thesis is to provide an atomistic insight of the mechanics of nanomachining of GaAs, including cutting temperature, cutting forces, incipient plasticity, tool wear and sub-surface damage.

In order to achieve this aim, the principal objectives are:

- To review the state-of-the-art nanomachining approaches and identify the knowledge gap of nanomachining GaAs.

- To explore the initial ductile plasticity of GaAs during nanomachining process.
- To reveal the formation mechanism of sub-surface damage of GaAs in nanomachining.
- To investigate diamond tool wear mechanism in nanomachining of GaAs through a new MD simulation model considering the diamond tool as a deformable body.
- To reveal the machinability of GaAs under high temperature.
- To carry out experimental work to validate MD simulation results.

1.3 Thesis overview

This work is divided into 9 chapters. The background, aims & objectives of this thesis are introduced in Chapter 1.

- Chapter 2 will present a comparative assessment of SPDT and SPL techniques. It also reviews previous MD simulation studies on nanometric cutting.
- Chapter 3 will systematically introduce MD simulation models, potential functions and visualization tools.
- Chapter 4 discusses the results of MD simulation of nanometric cutting of single crystal GaAs during SPDT and its experimental validation from the aspects of cutting forces, temperature distribution, and influence of crystalline orientation.
- Chapter 5 presents results of MD simulation study of SPDT of polycrystalline GaAs. The influence of grain boundaries (GBs) and phenomenon of dislocation nucleation are revealed.
- Chapter 6 provides a fresh perspective and new insights on the nanoscale friction in nanomachining of GaAs from aspects of kinetic coefficient of friction and

specific scratch energy. Both MD simulation and AFM nanoscratch experiments are performed in this study.

- Chapter 7 presents a comparison study of orthogonal and oblique AFM nanoscratching of GaAs by using experiments and MD simulations. The chip flow behavior and formation mechanism of sub-surface damage (SSD) are investigated. Additionally, the wear mechanism of diamond tip during AFM tip-based nanomachining of GaAs is revealed.
- Chapter 8 performs MD simulation study of machinability of GaAs under three representative temperatures, i.e. 600 K, 900 K and 1200K respectively. Results of cutting forces, friction coefficient, temperature distribution, shear plane angle, sub-surface damage depth, shear strain in the cutting zone, and stress on the diamond tip are benchmarked to those at 300 K.
- Lastly, Chapter 9 contains conclusions of this thesis and contribution to knowledge. Additionally, possible future research directions and recommendations are also provided.

Chapter 2 Literature Review

2.1 Introduction

Nanotechnology was firstly coined by Taniguchi in 1974 [15], which refers to the branch of technology that deals with dimensions and tolerances of less than 100 nanometers, especially the manipulation of individual atoms and molecules. Its development is inextricably linked to the downscaling of nanostructures with feature dimensions from 1-100 nm. Various nanometric structures, such as nano-dot arrays, nano-grooves and even three-dimensional (3D) nanostructures [16], have been explored for nano-products and electronic devices, nanophotonics [17], and even for biomedical science research [18].

Many nanomachining approaches have been used to process GaAs, including lapping, chemical-mechanical polishing, focused ion beam (FIB), single point diamond turning (SPDT) and SPL. Lapping [16][17] and chemical-mechanical polishing [18][21] can only machine planar GaAs wafer. They are not suitable for the machining of complex 2D or 3D nanostructures. In addition, the lapping and chemical-mechanical polishing processes are time-consuming [10][11]. FIB is capable of machining 3D nanostructures. It has been used to machine a GaAs hemispherical cavity with highly directional emission as quantum emitter [21]. However, FIB is not viable for mass production for future commercialization due to the low material removal rate. Moreover, it requires vacuum operational environment. Extreme ultraviolet (EUV) lithography is able to machine microelectronic GaAs-based devices [13]. However, this method is extreme expensive due to the usage of costly light source and plasma treatment or reactive ion etching for post-processing [14]. Single point diamond turning (SPDT) can generate nano-smooth surfaces on GaAs with a single pass, which is regarded as a viable mechanical nanomachining process for industry. Scanning probe lithography (SPL) technique can pattern nanostructures with feature size less than 10 nm. It is extremely suitable for processing high-precision nanostructures on GaAs surface [22].

Therefore, this chapter concentrates on reviewing both SPDT and SPL techniques. SPDT and SPL will be compared from the aspects of machining capability, attainable resolution and tool wear. MD simulation investigations on nanometric cutting in the literature will be reviewed in this chapter as well.

2.2 Single point diamond turning

Initially, single point diamond turning (SPDT) was utilized to machine ductile materials, including copper and aluminium material. However, the ductile material components, ranging from the planar structures to complicated 2D/3D shapes, are not suitable in the advanced optical, photovoltaic and semiconductor fields due to the poor material properties. However, the hard-to-machine materials such as silicon, germanium and gallium arsenide, are capable of being applied the above fields due to their superb material properties. Therefore, an extension of SPDT technique has been developed to machine hard-to-machine materials.

The machining model developed by Black and Scattergood [23] in the 1990’s shows that diamond turned hard brittle materials surfaces are produced by a combination of brittle fracture and ductile mode removal mechanisms. Basically, diamond turning of hard brittle materials utilizes a “controlled damage” process for material removal. Figure 2.1 shows generation of cutting chip and machined surface of ductile-regime machining process in single point diamond turning. The chip thickness at the "brittle-ductile transition" (BDT) point is called the critical chip thickness (d_c). d_{max} is the maximum chip thickness, which can be calculated by:

$$d_{max} = R - \sqrt{R^2 + f^2 - 2f\sqrt{2Ra_p - a_p^2}} \tag{2-1}$$

Where R is cutting tool nose radius, f refers to feed rate and a_p represents nominal depth of cut during single point diamond turning process.

Above the transition point, the maximum chip thickness d_{max} is bigger than d_c, micro-fracture damage occurs and the removal is by brittle fracture. Below the transition point, the maximum chip thickness d_{max} is smaller than d_c, plastic deformation takes place and ductile regime removal is achieved. Some micro-fracture damage can be removed by subsequent cutting. If the depth of the micro-fracture damage does not propagate below the machined surface then a surface free of fracture and pitting can be obtained.

More recently, SPDT was used to machine the GaAs as a purely mechanical method and a relatively high material removal rate was achieved [7]. Through establishing machining parameters to meet brittle-to-ductile transition condition, some researchers [6], [7], [24] have already successfully obtained nano-smooth machined surfaces in all the orientations on GaAs surface without cracks in the subsurface layer. These works have proved that SPDT is an effective candidate for nanomachining of GaAs.

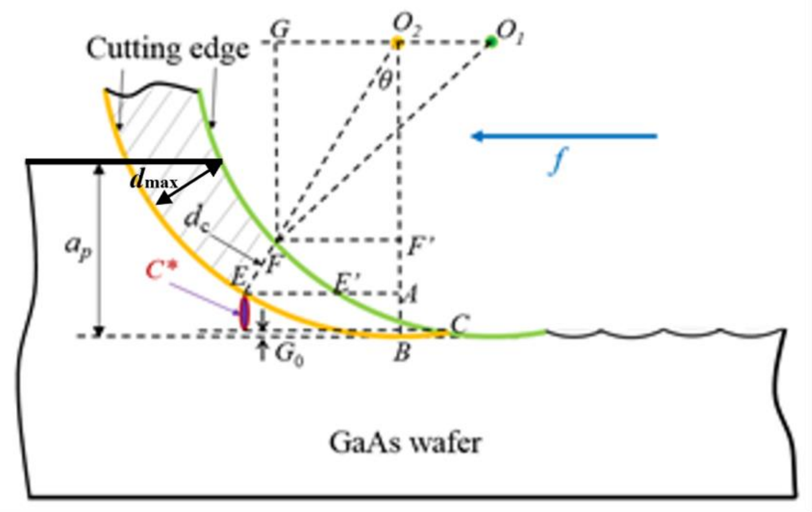

Figure 2.1 The schematic diagram of ductile-regime machining process in SPDT [7].

2.3 Scanning probe lithography

2.3.1 *History of scanning probe lithography*

The generic scanning probe microscope (SPM) is a branch of microscopy which employs a physical tip to scan the workpiece surface to detect the topography of the workpiece surface. SPM is an absolutely versatile instrument that has been thriving since its invention in 1981 at IBM by Gerd Binning and Heinrich Rohrer, who thereafter gained the Noble Prize in Physics in 1986 [25]. The invention of SPM can not only mark the birth of a new technology field of imaging and analyzing the material surface at the nanoscale but also trigger an unprecedented approach innovation to carry out the maskless nanomachining or even atomic and close-to-atomic scale manufacturing via the two most popular family members of SPMs: scanning tunneling microscope (STM) and atomic force microscope (AFM). The precedent of atomic and close-to-atomic scale manufacturing can date to 1990. As we all known, D. M. Eigler and E. K. Schweizer posited an image of IBM by manipulating Xe atoms on the Ni workpiece for the first by employing STM [26]. Thereafter, AFM was firstly utilized as a powerful machine tool to modify material surface, such as polycarbonate surface in 1992 [27] and gold surface in 1997 [28]. Undergoing nearly 30 years of development, the family group of SPMs has been extremely expanded, such as the invention of electrostatic force microscopy (EFM) [29], magnetic force microscopy (MFM) [30], fluidic force microscopy (FluidFM) [31], piezoresponse force microscopy (PFM) [32]. Consequently, a variety of SPL techniques are also created and developed through various mechanisms including atomic manipulation, electric field emission, chemical diffusion, electrochemical reaction, thermal deposition and mechanics scratching. To date, the SPL technique has been deemed as a practical method to implement the nanomachining and atomic and close-to-atomic scale manufacturing.

2.3.2 Atomic and close-to-atomic scale manufacturing

2.3.2.1 Fabrication mechanism

This atomic and close-to-atomic scale manufacturing (ACSM) grows out of SPL work principle. In terms of STM work principle, as shown in Figure 2.2 (a), when a sharp metal tip with a bias voltage is approaching to a conductive surface within 1 nm vacuum gap, a electrons quantum tunneling can be created with a ranging from several picoamperes to nanoamperes magnitude electron current that shows a monotonic exponential variation with tip-surface distance. Subsequently, a resolving down scale to individual atom topography of workpiece can be mapped. When the distance between tip and workpiece is decreasing to hundreds of pm continuously, an existing force exerted by tip can cause the workpiece atom within adsorption site to hop to adjacent empty site of tip to complete once single atom machining. Additionally, the measurement of threshold force has been realized. Although AFM and STM were invented almost simultaneously, the machining capability of AFM and STM is in different pace. AFM based machining has various versatile machining approaches depending on AFM own scanning type, which is far beyond STM based machining. In terms of AFM work principle, as shown in Figure 2.2 (b), there are three modes (contact, tapping and non-contact) in AFM that are categorized in terms of the exiting force type between probe and sample surface. The typing mode-based machining approach in AFM can carry out atom manipulation at room temperature. The fundamental cause of the capability of atom manipulation in AFM is AFM has atomic scale resolution. The atomic scale resolution of AFM can be appreciable by detecting and precise quantifying the short-range bonding interaction forces (normally tens of piconewtons to nanonewtons) between the headmost atom of tip and workpiece surface atom which is closest to tip headmost atom. Therefore, in the tapping mode, a high and powerful sensitive detector which can accurately tune the interaction forces by regulating the oscillation of cantilever results in atom manipulation.

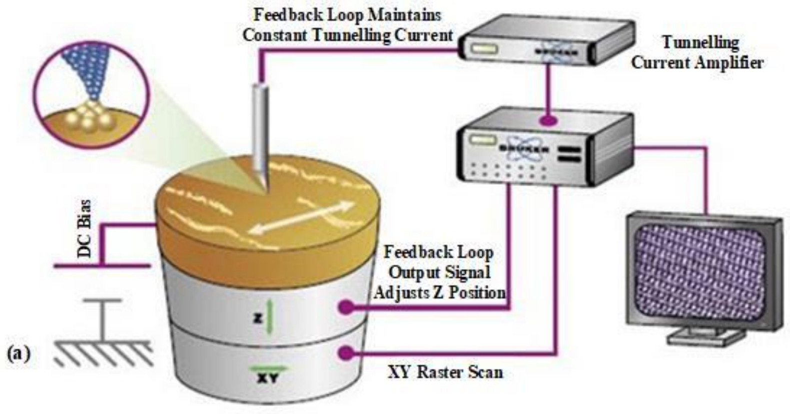

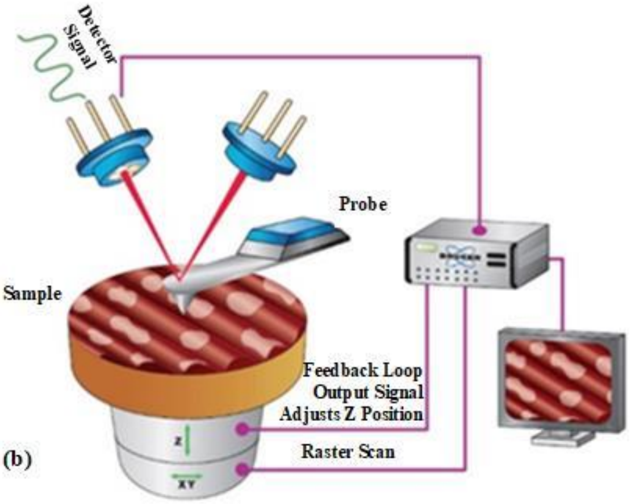

Figure 2.2 (a) The principle of STM. (b) The principle of AFM [33].

2.3.2.2 Research status

Ternes et al. [34] succeeded to manipulate a single cobalt atom 160 pm on Pt and Cu surface via 210pN, as shown in Figure 2.3 (a). Therefore, many efforts have been performed for moving single atom onto the desired workpiece surface with atomic-scale resolution, such as quantum corrals constructed by 48 iron atoms on Cu surface [35] which is illustrated in Figure 2.3 (b). After decade-old, Repp et al. [36] realized the manipulation of turning neutral charge state gold atom into negative charge state gold ion using a tungsten tip at between 5 and 60 kelvin temperature, as demonstrated in Figure 2.3 (c) and Figure 2.3 (d). This breakthrough makes storing each bit information according to each atom possible for memory devices. Additionally, ACSM technique has also been extended to molecular manipulate. Quek et al. [37] employed STM with a gold tip to touch gold surface adsorbing 4,4’-bipyridine and found a single-molecule junction could be created which could be turned on and turned off with stretching or compressing operation of gold tip. This discovery gives a fundamental understanding of molecular resistance that can be applied in future molecular electronic device as a molecular switcher, which is shown in Figure 2.3 (e).

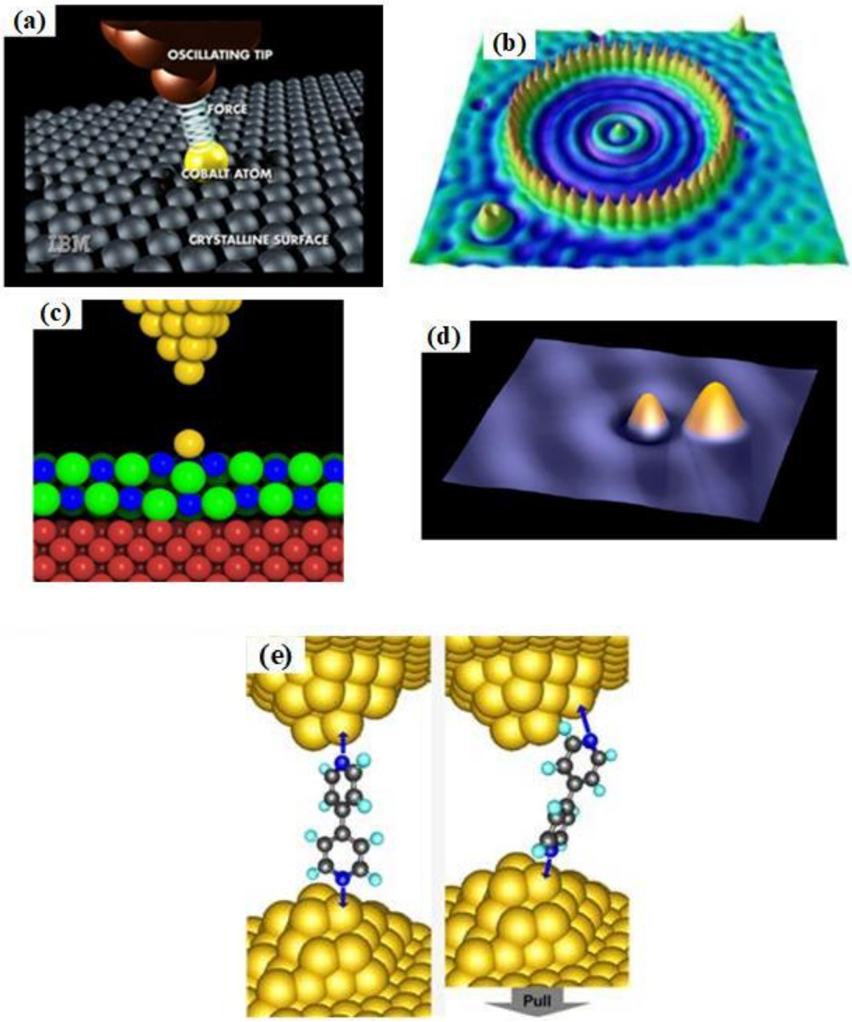

Figure 2.3 (a) The force measure model to move a single cobalt atom [34] (b) STM image of nanometre-scale quantum corrals structure [35] (c) The scheme of machining gold atom into ion (d) The STM image of two gold atoms on NaCl film surface. The left place atom is a machined gold ion with a negatively charge [36]. (e) A single-molecule junction switcher [37].

The ACSM technique has been applied in various research aspects, such as quantum dots machining and single atom data storage device machining. For example, Stefan et al. [38] employed STM to create quantum dots of single atom precision fixed by 2×2 In-vacancy reconstructive InAs (111) template surface, that was effective to control the position of quantum dots with zero error. The specified location quantum dots were consisting of a chain of ionized In adatoms moving by using vertical atom manipulation of STM, which is shown in Figure 2.4.

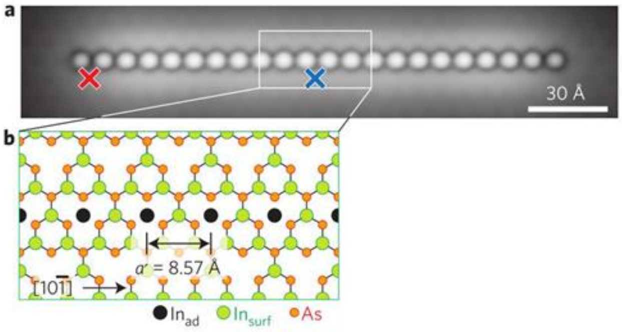

Figure 2.4 (a) The quantum dots constructed by a chain of 22 ionized In adatoms. (b) The reconstructive InAs template lattice including black In adatoms, green In, and red As [38].

Another example is that Cyrus et al. [39] succeeded to store data in bits in one magnetic atom. They used STM atom manipulation technique to place an Fe or Mn atom on the non-magnetic copper-nitride film surface and created a structure of single Fe or Mn atom with magnetic surrounded by non-magnetic atoms, which could align the magnetic moment along one direction and overcome superparamagnetic limit, as shown in Figure 2.5. Additionally, the magnetic anisotropy in just one atom was also observed in the first time.

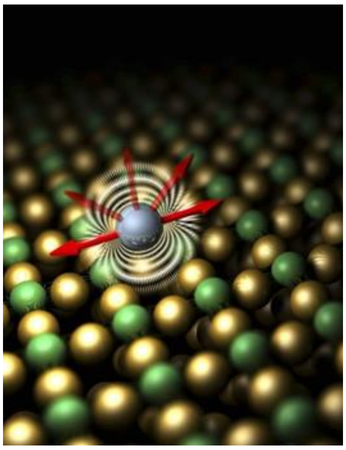

Figure 2.5 The Fe atom surrounded by non-magnetic copper nitride atoms surface indicates its magnetic moment alignment along one direction [39].

Kawai et al. employed AFM to [40] perform the Br^- ion, as a defect on the NaCl (100) surface, lateral and vertical manipulation. With regards to lateral manipulation, as shown in Figure 2.6. The Br^- ion was manipulated three times totally (remarked number 1, 2, and 3) which are exchanging between Br^- and Cl^- on the NaCl (100) surface along with [100], diagonal exchanging between Br^- and Cl^- on the NaCl (110) surface along with $[\bar{1}10]$, moving Br^- to unimaged area along with [110], respectively. This Br^-lateral manipulation is more complicated atom removal process comparing with generally adatom lateral moving which has been reviewed [41].

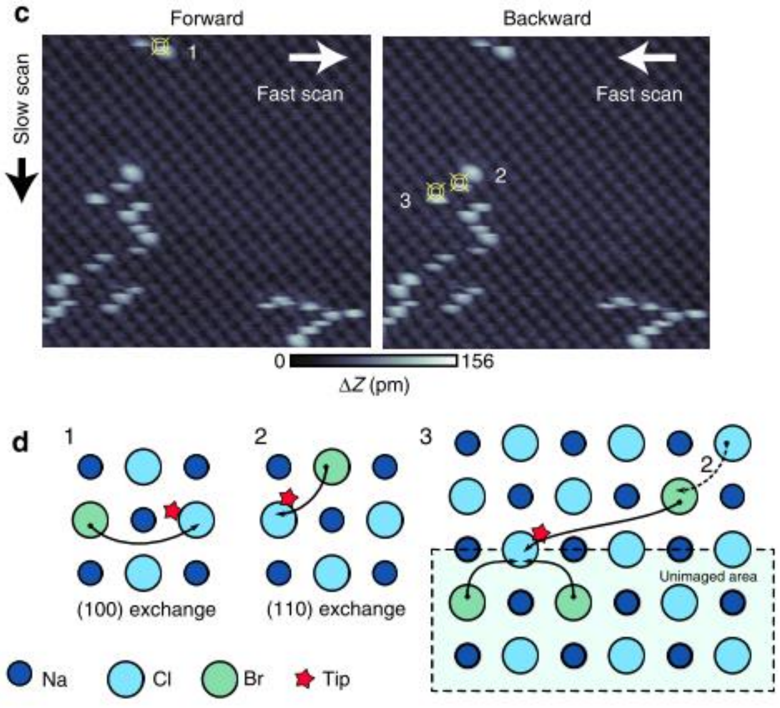

Figure 2.6 The real forward and backward scanning Br^{-} manipulation sequence event and theory model. The Br^{-} is surrounded by bright topographic features [40].

The Br^{-} vertical manipulation was transferred via picking up process and subsequent implanting process, as shown in Figure 2.7. The Br^{-} was picked up indicated by oscillation frequency signal changing abruptly when tip was implementing approach-retraction operation. Then the tip carrying Br^{-} was moved to desired position and the Br^{-} was implanted into NaCl surface confirming by the decreasing of oscillation frequency signal suddenly. Finally, a ’swiss cross’ atomic scale structure consisting of 20 Br^{-} ions was created by repeated operation that is demonstrated in Figure 2.8.

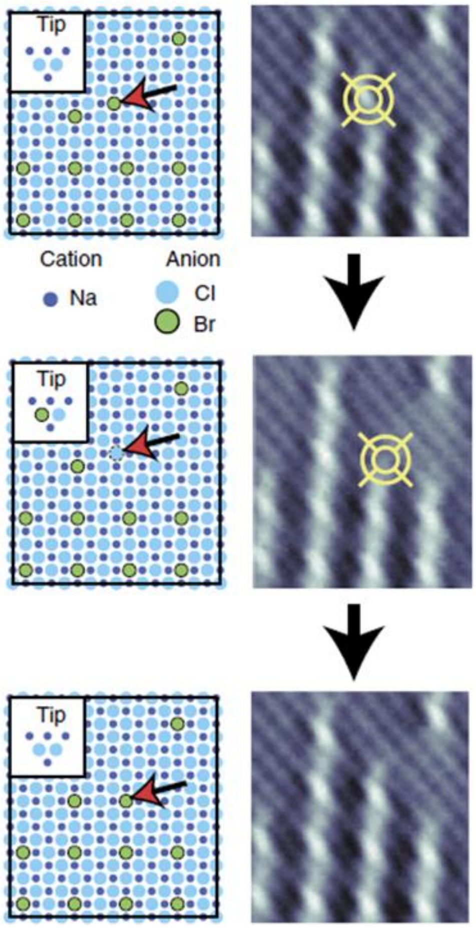

Figure 2.7 The vertical atom manipulation image process including: before manipulation (top), after picking up Br^- (middle), and after implanting Br^- (bottom) [40].

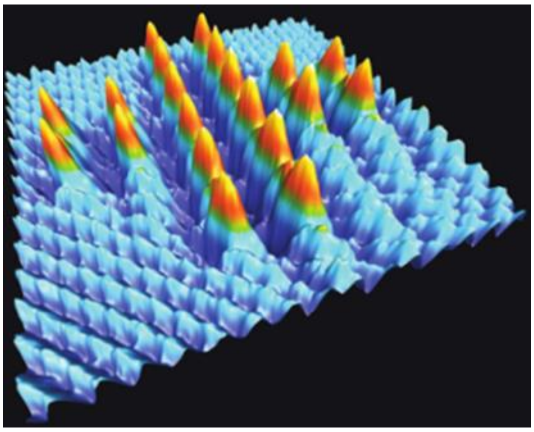

Figure 2.8 A 'swiss cross' atomic scale structure image consisting of 20 Br^- ions [40].

AFM is not only a powerful atoms manipulation tool at room temperature but also can monitor and track single electron in the defined artificial atoms structure. For example, Mohammad et at. [42] first erased the hydrogen atom using AFM on the hydrogen terminated silicon surface to create six silicon dangling bonds, as shown in Figure 2.9. Then they observed how electron jump between the defined artificial atom structure. This technique took its first step to develop atomic circuits in the future.

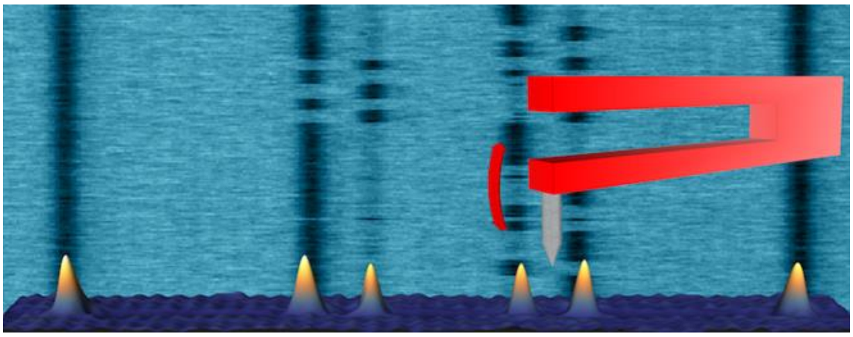

Figure 2.9 The artificial atomic structure with six silicon dangling bonds [42].

2.3.2.3 Merits and drawbacks

In summary, ACSM technique shows excellent capability in changing mechanical, electronic and chemical properties of specimen surface to achieve local repair of the workpiece without destruction via simple single atom manipulation and molecular transformation process, which lights the future atomic scale machining research direction. However, it has extremely high requirement for conductive tip and workpiece, vacuum operation environment and fixed temperature.

2.3.3 Oxidation scanning probe lithography

2.3.3.1 Fabrication mechanism

The O-SPL approach was firstly conducted in 1989 by the National Institute of Standards and Technology. Figure 2.10 illustrates the machining mechanism of O-SPL.

It is based on an anodizing reaction between the probe and the substrate surface to form a nanoscale oxidation structure. During the oxidation process of the sample surface, the AFM probe is the cathode (negative) of electrochemical anodic reaction, the surface of the sample is anode (positive). The H_2O water molecule adsorbed on the surface of the sample acts as the electrolyte in the electrochemical reaction providing the OH^- ions (hydroxyl ions) needed in the oxidation reaction [43]. A key characteristic of O-SPL is the achievement of a liquid meniscus bridge between probe and substrate surface. In fact, the process involves the formation of multiple water bridges. Molecular dynamic simulations have demonstrated the transformation process of water bridge from a water droplet on the silicon surface and shown the formation is quick [44]. The liquid bridge size can be increased by increasing the voltage strength from 20 to 30 voltages or the pulse duration from 10 μs to 10 s [45]. Accordingly, the size of the meniscus bridge determines the resolution of the structures achieved by this method. O-SPL can be carried out under contact mode or non-contact mode between the probe and the substrate surface.

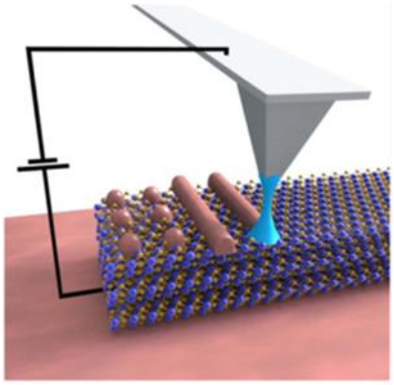

Figure 2.10 Scheme of nanopatterning using O-SPL [46].

2.3.3.2 Research status

O-SPL is considered to be an important technology to support the development of nanoelectronics industry in the future. It has received great attention and developed rapidly. This technology has been widely used in resist masks [47], graphene, semiconductors, polymers, metals and thin conductive films for nanoscale patterning [48] and has been fabricated to nanoscale functional devices such as field-effect transistors, single-electron transistors, and single-electronic memory device [49]. For example, graphene nanoribbons with neat edges can directly be prepared by O-SPL, as illustrated in Figure 2.11. The reason of neat edges of graphene nanoribbons is attributed to the created oxidized graphene forming gas oxide diffusion in the air [50].

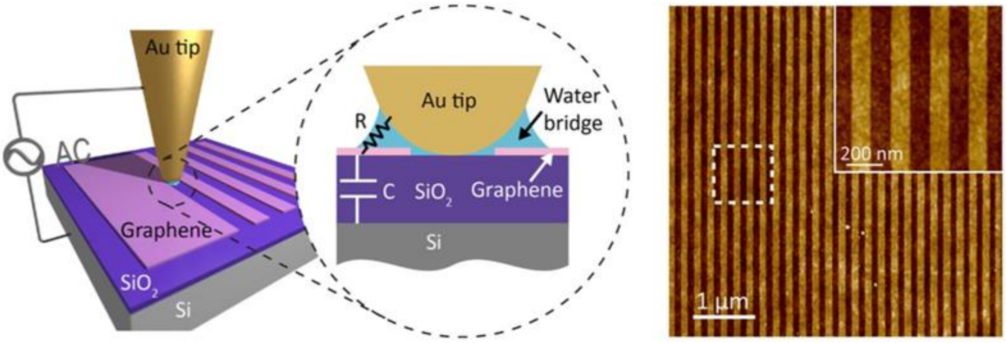

Figure 2.11 Fabrication of graphene nanoribbons using O-SPL [50].

Ramses V Martinez et al. [51] utilized O-SPL to accomplish single crystal silicon field effect transistor using nanoline nanostructure as shown in Figure 2.12 (a). It shows the partial cross section of the silicon nanoline transistor and electrodes on both sides of transistors and the width of the nanoline is nearly 9.5 nm. Figure 2.12 (b) shows the achieved various high accuracy sub-20 nm straight and round nanoline structures. The nanoline transistor has succeeded in immunological examination application and the on/off current ratio is up to be 10^5.

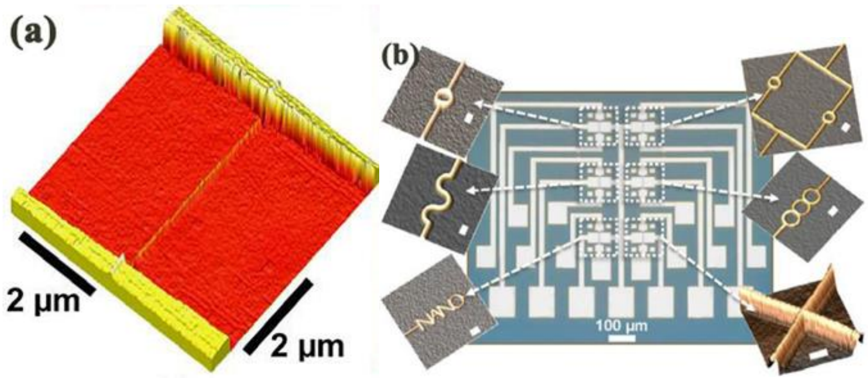

Figure 2.12 (a) The topography of single crystal silicon field effect transistor using nanoline nanostructure. (b) The image of various sub-20nm straight and round nanoline structures [51].

Additionally, the qualitative investigation is developed for dichalcogenides of transition metal application. Espinosa et al. [52] carried out the fabrication on MoS_2 substrate and obtained a 200 nm nanochannel successfully with the barriers of around 30 nm as demonstrated in Figure 2.13. The electrode and base were gold and silicon dioxide, respectively. The result shows the electrons can flow in the fixed nanochannel. More importantly, the overall conductivity of the MoS_2 is not weakened. It means the size of the conductive channel is downscaling from micrometers scale to nanometers scale. Additionally, the transistors depending on MoS_2 have had a wide application in the nonvolatile memory cells [53] and medical biosensors for cancer sensitive identification [54]. Another example is Dago et al. [55] obtained 1 nm height and sub-20 nm width and 40 periodicity nanodots structures on the multiple layers WSe_2 as shown in Figure 2.14. These results indicate that the O-SPL is envisaged a straightforward approach for the 2D transition metal fabrication.

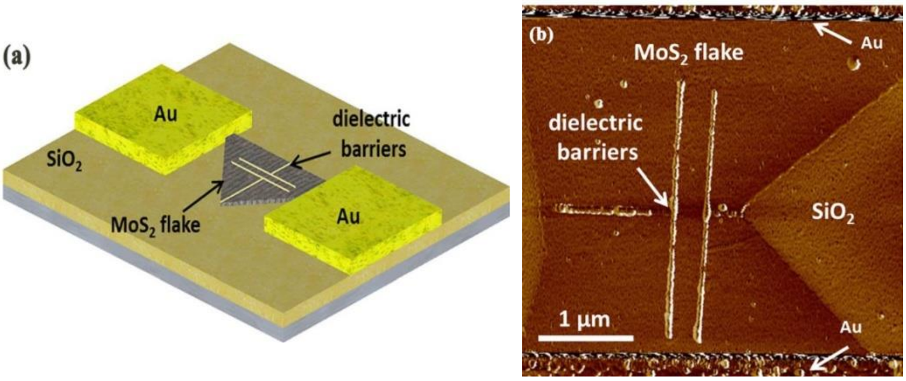

Figure 2.13 (a) The theory model of transistors depending on MoS_2. (b) The achieved nanochannel pattern on the MoS_2 flake between electrodes [52].

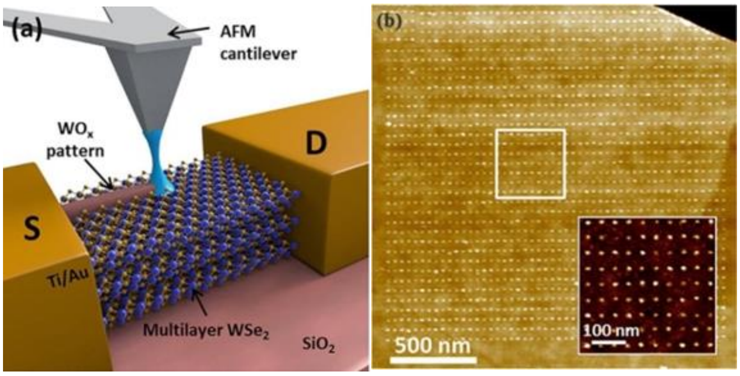

Figure 2.14 (a) The mechanism scheme of the multiple layers WSe_2. (b) The achieved nanodots oxide structure [55].

A key study in terms of the slight possibility of 3D fabrication was reported by Lorenzoni et al. [56]. Figure 2.15 shows the obtained high aspect ratio array nanodots and even the highest nanodot is above 100 nm via changing voltages up to 10 V and selecting pulse time between the conductive tip and 6H-SiC substrate. The fruit illustrates the new fabrication possibility for 3D nanostructures.

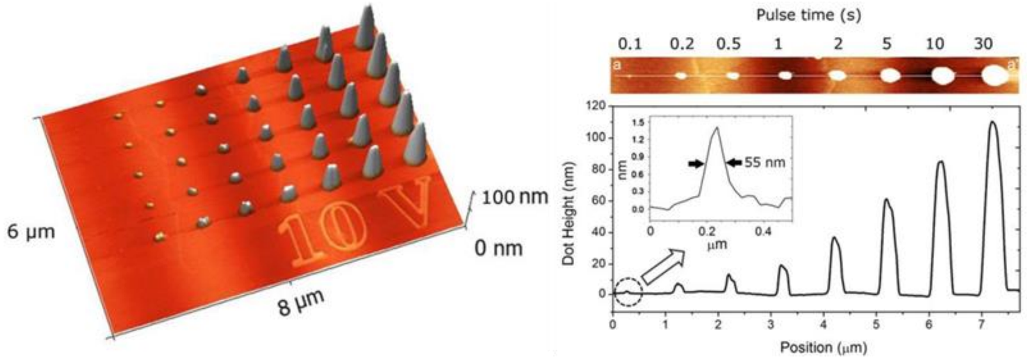

Figure 2.15 The image of nanodots geometry and height profile [56].

Much more interestingly, the O-SPL can be used to perform a coating silicon surface by embedding nanoparticles by Cavallini et al. [57]. Figure 2.16 (a-d) shows the entire embedded nanoparticles process. The $CoFe_2O_4$ nanoparticles are successfully embedded into the SiO_2 layer by using O-SPL and eventually dots and lines structures are obtained as shown in Figure 2.16 (e) and Figure 2.16 (f).

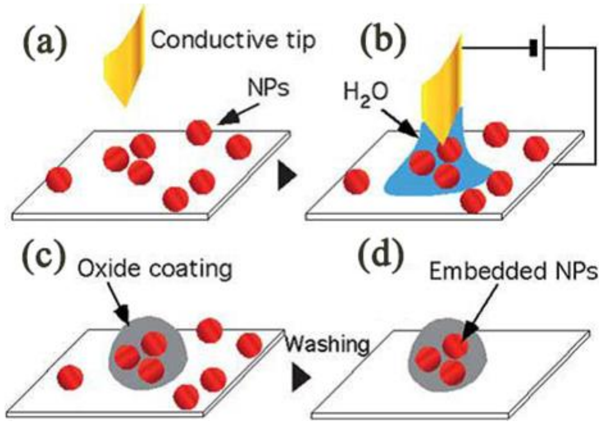

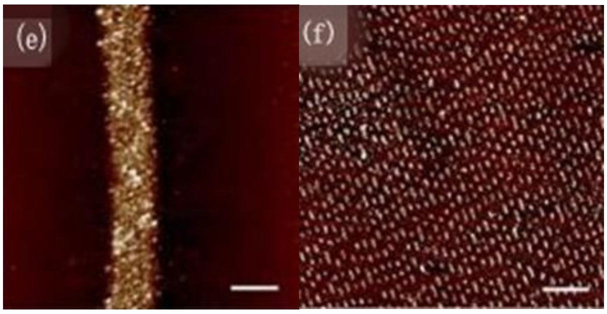

Figure 2.16 (a-d) Scheme of nanoembedding. (e) Single stripe of CoFe2O4 nanoparticles embedded. (f) The 11 cm^2 area patterning of a structure containing dots and lines [57].

2.3.3.3 Merits and drawbacks

The oxidation process is simple and easy to use and the achieved structure is extremely stable and robust. The achieved oxide material has the characteristics of insulation and corrosion resistance and thus is able to be compatible with the existing nanoelectronics machining process. This method can create a mask with high hardness and operate in low pressure range which can effectively avoid the proximity effect of electron beam machining. Additionally, the widespread academic use of O-SPL is from metals to semiconductors and more recently to graphene and polymers. Moreover, the technical operation is under room temperature and atmospheric pressure, making O-SPL appealing for academic research. In spite of material patterning diversity, the O-SPL has high requirements on the oxidizability of the sample material, which limits the application scope of this technology to some extent. Additionally, it is difficult to obtain large area high accuracy nanostructures due to the drift, hysteresis lag and nonlinearity problems of the piezoelectric actuator of the SPM itself. Finally, to date, it is to the point hard to fabricate complex 3D nanostructures with controllable depth.

2.3.4 Thermal/thermochemical scanning probe lithography

2.3.4.1 Fabrication mechanism

Thermal scanning probe lithography fabrication (t-SPL) and thermochemical scanning probe lithography fabrication (tc-SPL) are conceptually simple, yet potentially very flexible scanning-probe lithography methods. If the thermal process leads to effective material removal in order to create topographic structures, the fabrication method is referred to t-SPL which is illustrated in Figure 2.17 (a). This method can usually modify a polymer mechanically. For example, researchers have utilized a transparent polymethyl methacrylate (PMMA) as the substrate to carry out nanoindentation aiming to fabricate high density data storage device [58]. Additionally, the t-SPL does not need conductive materials surface [59]. If the fabrication process is completely thermochemical essentially and the achieved structures consist of a kind of material having a different conformation and chemical composition from the original structure, we call tc-SPL which is illustrated in Figure 2.17 (b). In this method, the resistance-heated SPM cantilever incurs a clear chemical reaction and changes surface functionality of work material. We can note that, in the t-SPL and tc-SPL methods, the heat acts as a pivotal function part. Especially for the tc-SPL method, the rate of chemical reaction raises by exponential rate along with the increase of temperature. For the early experiments, the laser was used to heat the cantilever. But it was very difficult to integrate a heating laser source into an SPM system. Today, cantilevers with integrated resistive heaters are emerging as a solution as it is easier to integrate into an SPM system. Silicon SPM cantilevers with integrated resistive heaters, as shown in Figure 2.17 (c), can reach a temperature of over 1000˚C depending on the type of dopant. In addition, the thermal time constant can be fast up to 10 µs [60].

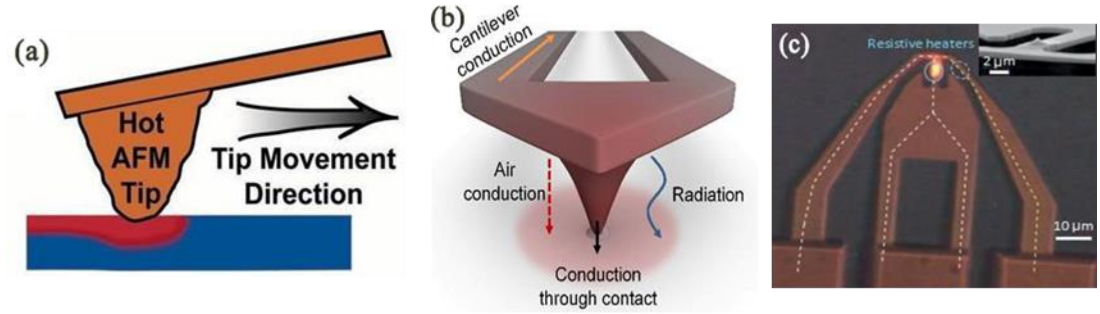

Figure 2.17 (a) Experiment installation displaying a resistance-heated silicon AFM cantilever scanning on a polymeric compound substrate using t-SPL [61]. (b) The chemical stuff is induced by heated tip [62]. (c) A resistive heating AFM cantilever with two highly doped silicon legs [63].

2.3.4.2 Research status

The t-SPL and tc-SPL can fabricate a wide variety of materials, such as molecular glass resist [64], biomaterials, organism [65], 2D materials [66][67], metals, carbon nano-tube [68], nano-particles and polymer including supramolecular polymer [69], polycarbonate [70][58], polystyrene [71], block copolymers [72], polyethylene [73]. Preliminary work on the t-SPL was undertaken in the early 1990s and it was firstly exploited for data storage purposes. In that work, a variety of heated tips were employed to pattern pits structures into a polymeric compound substrate surface. Figure 2.18 (a) shows data bits written in a polycarbonate substrate spaced less than 200 nm apart with a patterning time of 5 ms per bit. In addition, t-SPL has been used to create nanostructure with 55 nm pitch line on the Si substrate with high resolution. It also has demonstrated a lower line edge roughness, as shown in Figure 2.18 (b). Furthermore, Ryu Cho et al. [74] revealed the optimal mechanical force 25 ± 6 nNs and the best heated tip temperature 550−700 °C when fabricating nanopatterns on Si substrate, respectively.

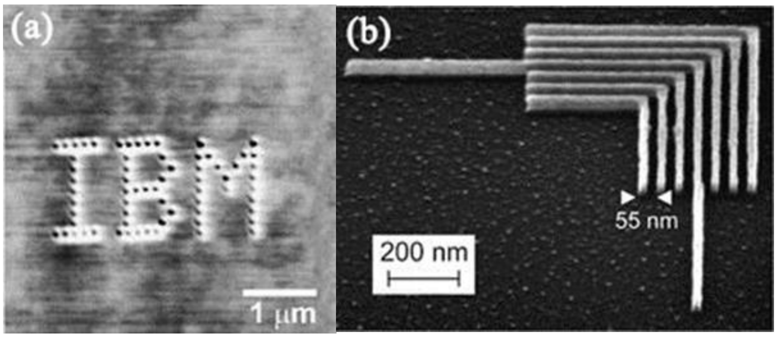

Figure 2.18 (a) Thermomechanical data bit written on polycarbonate [58]. (b) L-lines structures at 27-nm half-pitch [75].

To date, the t-SPL has been used in the fabrication process of quantum nanoscale electronic components. For example, Rawlings et al. [76] employed a hybrid method including t-SPL and laser machining to obtain a single electron transistor with 50 nm insulated gate. Figure 2.19 (a-b) shows the process of the polypthalaldehyde (PPA) is patterned by t-SPL with 15 nNs scratching force under 950°C and the patterned result, respectively. Figure 2.19 (c) demonstrates the final achieved nanostructure after t-SPL and laser machining. Additionally, t-SPL is as a rapid and flexible approach to fabrication arbitrary structures of nanofluidic channels. For example, Hu et al. [77] utilized t-SPL to directly fabricate an etch mask by depositing polymer nanowires on Si surface. The nanostructures on the Si surface by single step etching were employed as a mold for mass production of polydimethylsiloxane (PDMS) nanofluidic channel. Furthermore, the PDMS nanofluidic channel with both straight and curvilinear structures was fabricated by utilizing t-SPL, as illustrated in Figure 2.20.

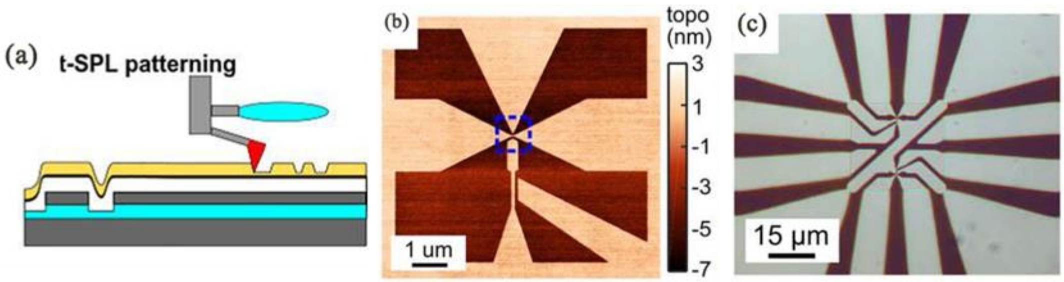

Figure 2.19 (a) The process of the polypthalaldehyde (PPA) is patterned by t-SPL. (b) The patterned result after t-SPL. (C) The final achieved nanostructure after t-SPL and laser machining [76].

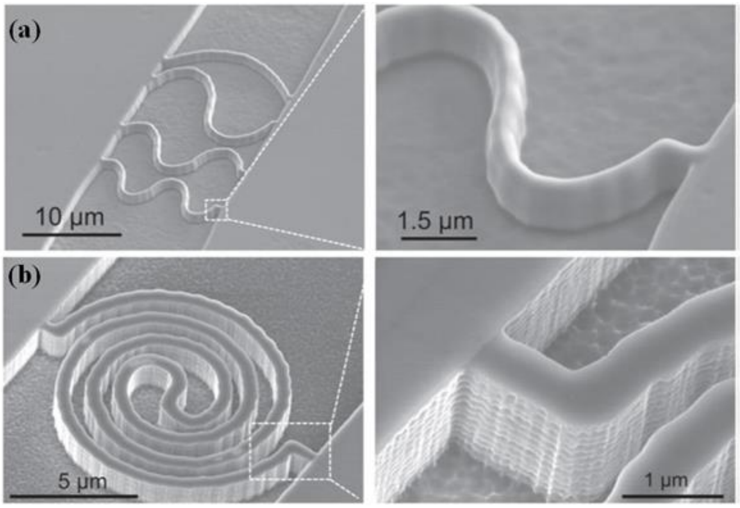

Figure 2.20 Images of nanofluidic channels (a) four wavy shapes, (b) spiral-shaped [77].

In fact, the t-SPL is a clock concept pairing with heating the tip of the SPM. Conversely, what will be achieved if we heat the substrate as well? Shaw et al. [78] made the experiments heating the tip up to 500°C and substrate simultaneously for fabricating PMMA and Pentacene at 120°C, 140°C and 160°C, respectively. The relationship of the substrate temperature and maximum scanning speed is shown in Figure 2.21. These selective high temperatures did not make the substrate material be conversion and phase transformation. They found out the fabrication speed was fast up to 19 times than conventional fabrication only heating the tip of SPM. Recently, another important application of the t-SPL is in the anti-counterfeit symbol field. Samuel et al. [69] explored fluorescence features nanostructure, which could apply in the counterfeit security, on the supramolecular polymer with thermochromism due to the thermal tip characteristic of t-SPL. The color of the supramolecular polymer could change from red to green when the heated tip contacted onto the local area. Figure 2.22 presents the fabrication mechanism for a supramolecular polymer with thermochromism and 40 × 40 μm^2 and 86 nm resolution nanostructure with fluorescence characteristic.

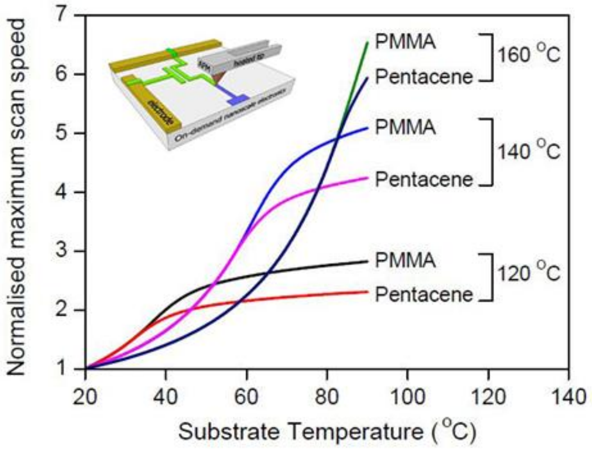

Figure 2.21 The relationship of the selective substrate temperature and maximum scanning speed [78].

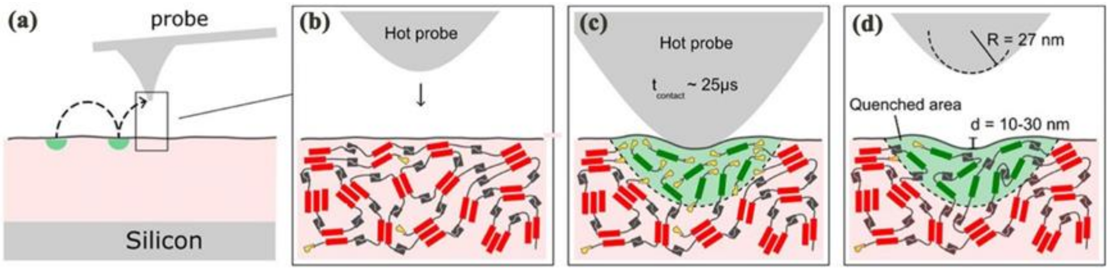

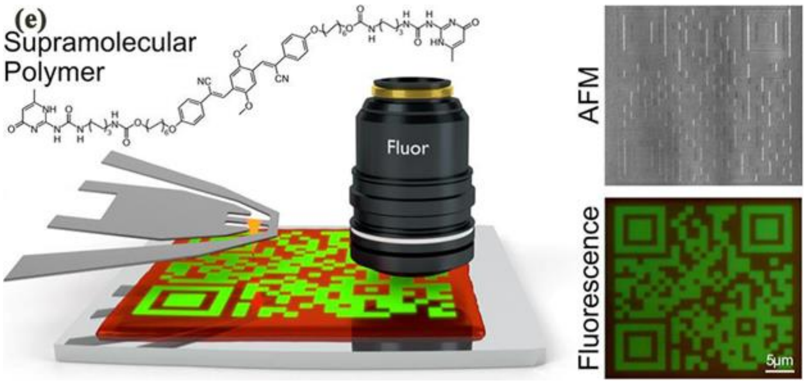

Figure 2.22 (a-d) Fabrication mechanism for supramolecular polymer substrate. (e) 40 × 40 μm2 and 86 nm resolution nanostructure with fluorescence characteristic [69].

As for tc-SPL, a kind conjugated polymer of *p*-phenylene vinylene (PPV) is quite an active substrate due to its electroluminescent feature among this approach, which is widely applied in the field nanophotonics and Light Emitting Diodes (LEDs) [79]. For example, Wang et al. [59] used tc-SPL to obtain a 70 nm width nanoline structure on the 100 nm thichness PPV substrate with a 240°C heatable tip. The scanning speed and vertical load are 20 μm/s and 30 nNs, respectively, as shown in Figure 2.23. What's more, Oliver et al. [80] succeeded in running the finite element model simulation process of thermal tip approaching the PPV surface and indicated the nanoline could be further achieved more accurate when the PPV layer became thinner and the radius of the tip was smaller.

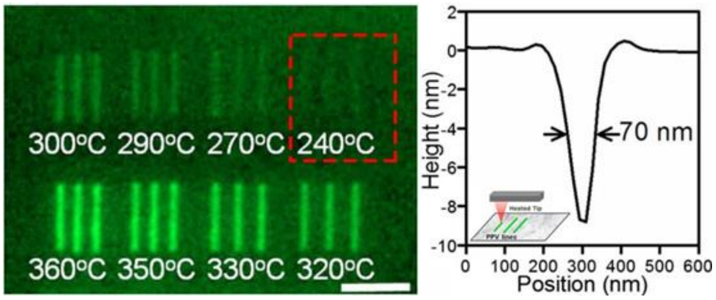

Figure 2.23 The fluorescence picture of the nanoline structure with 70 nm width under 240°C hot AFM tip [59].

2.3.4.3 Merits and drawbacks

In general, t-SPL and tc-SPL are simple, direct and extremely rapid fabrication methods. The methods can not only achieve the sub-20 nm fabrication accuracy [81] but also can effectively reduce the probe wear. In particular, the tc-SPL method is able to work in the liquid circumstance as a water film structure of several nanometers could be performed in the humidity environment. However, the methods are only suitable for the patterning of highly thermosensitive materials for high resolution. The existing fundamental challenge of the two methods is how to estimate heat flow through the tip and to assess the interface temperature between the probe and the substrate. Simultaneously, thanks to the use of thermal effect to produce nanostructures, it is difficult to break through the limit of the tip's apex size if the fabrication precision needs to be further improved.

2.3.5 Dip-pen scanning probe lithography

2.3.5.1 Fabrication mechanism

Dip-pen scanning probe lithography fabrication (D-SPL) is a novel method that employs a kind of ‘ink’-coated AFM probe to machine the substrate by way of electrostatic interaction [82] or electrochemical reaction [83]. Dip-pen SPL is a direct-writing nanomachining method that is able to pattern soft and hard materials from scanning probe onto a sample surface with accurate position and sub-100nm resolution [84], just as ink moving from a visible ink pen to paper. Figure 2.24 (a) demonstrates the mechanism of the approach. Importantly, D-SPL is compatible with various inks, such as organic molecules [85], polymers [86], proteins [87][88], inorganic nanoparticles [89], DNAs [90] and metal ions [91]. Much significantly, the ink molecules can be transported to the tip through a microfluidic channel so that the ink needed in the process can be supplied continuously, as illustrated in Figure 2.24 (b).

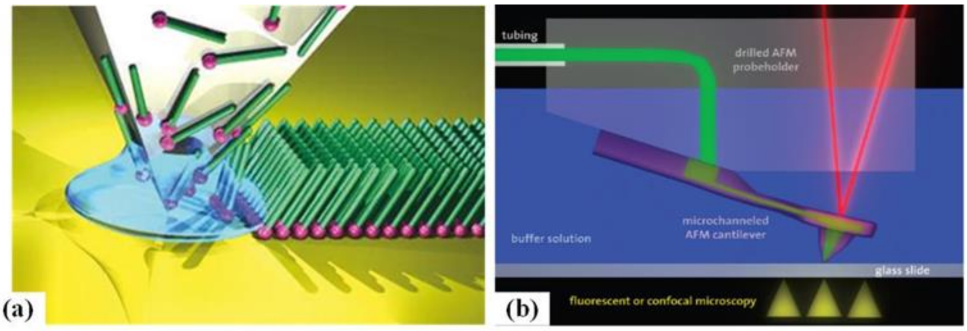

Figure 2.24 (a) The mechanism schematic of D-SPL [92]. (b) Nanofluidics delivery system [93].

2.3.5.2 Research status

To date, the D-SPL has been undoubtedly developed to be multiplex [94]. Firstly, based on the above-mentioned prototype method, scholars directly deposit target material onto the substrate surface by solvent instead of transferring by water meniscus, where the target material is usual small molecular material and only can be soluble in the water meniscus. This improved approach enlarges the inks kind range enormously. For example, Hung et al. [95] reported the Ag nanoline structures height ranging from 120 nm to 260 nm with around 30 μΩ·cm averaging resistor was accomplished by depositing the containing Ag material nanoparticle solvent onto the SiO_2 substrate. The process mechanism schematic and the image of Ag nanoline structures are exhibited in Figure 2.25 (a-b) and Figure 2.25 (c), respectively. This method offers a specific metal nanoparticle deposition technique, which can be widely applied in the field of printable electronic and electronic invalidation analysis.

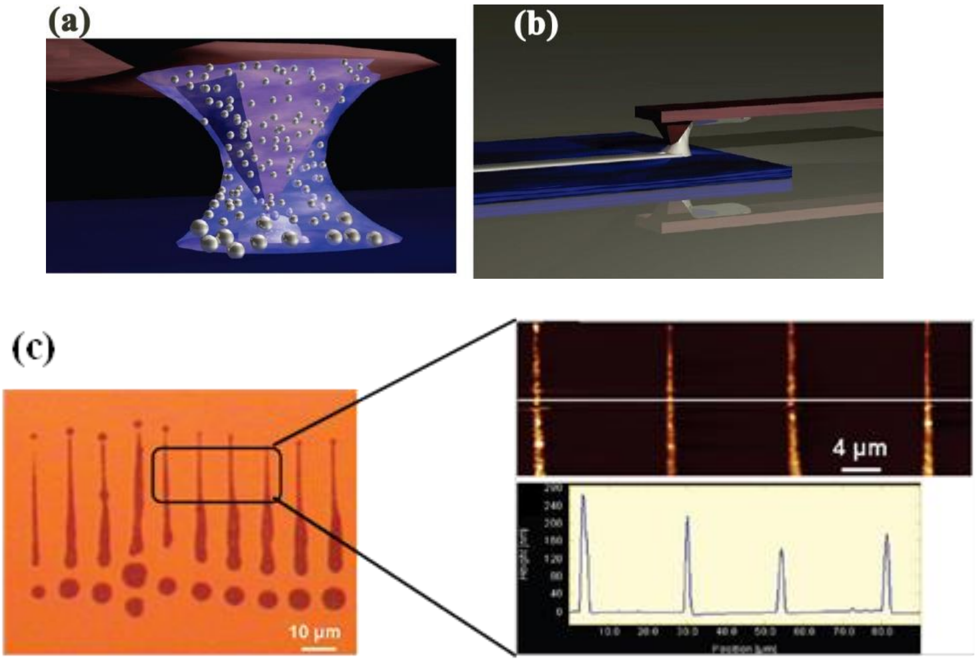

Figure 2.25 (a-b) The process mechanism schematic of depositing the containing Ag material nanoparticle solvent onto the SiO_2 substrate. (c) The Optical image and AFM image of the Ag nanoline structures [95].

Secondly, a matrix can be exploited to assist target material to deposit onto the substrate surface through water meniscus or solvent, in which the matrix is as a carrier. For example, Chen et al. [96] have made a contribution to developing a precursor for the formation of multimetallic nanoparticles downscaling to the nanometer level. In this work, the PEO-*b*-P2VP was made as the matrix carrying the five kinds of the metal nanoparticle, which is Au, Ag, Cu, Co and Ni, respectively, or the mixture of them and then a sub-10 nm polymetallic alloy hemisphere nanostructure was created. Finally, the PEO-*b*-P2VP could be decomposed. The process schematic is shown in Figure 2.26.

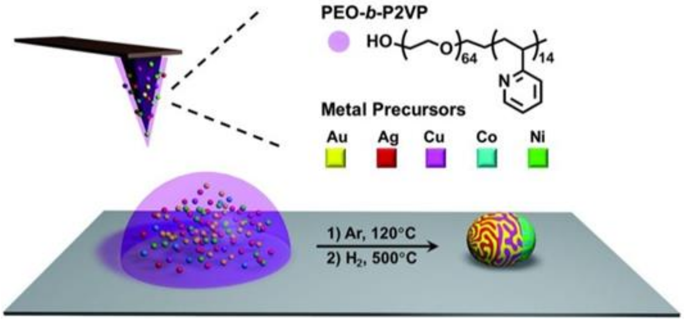

Figure 2.26 The fabrication process of polymetallic alloy hemisphere nanostructure by using D-SPL [96].

Additionally, Nelson et al. [97] expanded the D-SPL to the thermal D-SPL by means of heating the tip similar to the t-SPL and tc-SPL was exploited to obtain the sub-80 nm width line structure on the glass substrate mixed with borosilicate. The local deposition of the line structure is indium metal coating in the tip, as demonstrated in Figure 2.27 (a). This technique provided a novel approach for the circuit repair, such as the around 500 nm gap distance could be repaired by thermal D-SPL between both sides gold electrode, as shown in Figure 2.27 (b). The aim of the thermal application is to control the ink, indium metal, melt when achieving the metal melting point or not. Therefore, the deposition could be controlled easily. Similarly, a 6 nm high consisting of Fe_3O_4 nanoparticles was achieved by Lee et al. [98] using the thermal D-SPL.

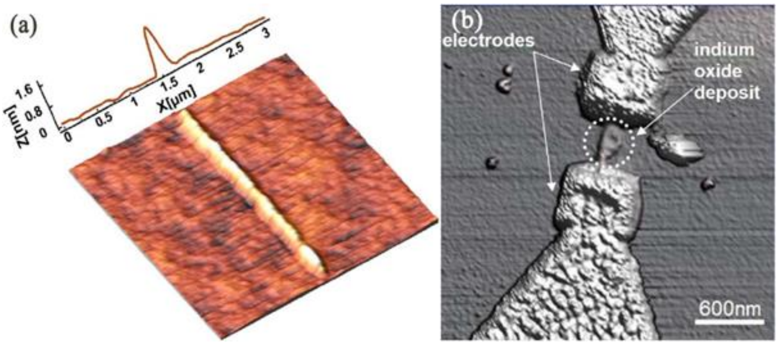

Figure 2.27 (a) The image of indium metal deposition on the glass substrate mixed with borosilicate. (b)The image of the repaired gold electrodes of around 500nm gap distance [97].

2.3.5.3 Merits and drawbacks

The D-SPL can not only deposit a variety of nanoparticles and nanocomposites but also is a real maskless nanomachining approach because the achieved substrates do not require retreatment, such as further tailor and solution technology process. Moreover, in this method, the achieved line width is independence with the speed of the tip and the contact force. Therefore, when a parallel and multiple tip fabrication system carried out [99][100], only one tip is controlled by the feedback control system and other tips can perform the same actions. Correspondingly, a large number of nanoline structures and even extend to a wide range of 2D nanostructures are able to be created and the fabrication efficiency can be improved rapidly while at the cost of fabrication accuracy. What is more, the local deposition has the drawback of inhomogeneous and inconsecutive, especially for nanolines structures. In addition, during filling the nanoparticles into the polymer, there is a composite thermodynamically stable problem causing by the radius of the nanoparticle when its radius is bigger than the radius of the polymer [101]. That is to say, the approach has the limitation for the size of the inks.

2.3.6 Bias induced scanning probe lithography

2.3.6.1 Fabrication mechanism

Bias induced scanning probe lithography (B-SPL) is derived from applying a bias voltage between the SPM tip's apex and substrate surface. The implemented voltage, which is usual from 0 V to 20 V, plays a pivotal role in the fabrication process. When applying about from 0 V to 20 V voltages, the real electric field is up to be from 10^8 Vm^{-1} to 10^{10} Vm^{-1} between the tip and substrate surface. The B-SPL can generate different chemical and physical fabrication results on different substrate material. For example, Figure 2.28 [102] shows the mechanism of generation of nanoscale structures on the extra thin polymer film substrate surface by employing a high electricity conductive tungsten carbide tip. Accordingly, the focused electron current brought by the high electric field will achieve a gradient distribution electric field configuration and make the polymer film surface to be turbulence and polarization. Furthermore, the current density can almost vary linearly with the applied bias voltages. The Kaestner et al. [103] discovered that when a tip with a less than 30 nm radius was approaching the polymer surface, in which the distance was less than 5 nm between tip and polymer surface. The surface of the polymer would raise bulge that the height could be formed from 10 nm to 50 nm [104]. Subsequently, nanoline structures and diverse 2D nanostructures could be accomplished with the tip moving. Therefore, it is a physical fabrication process for processing polymer materials. In addition, the B-SPL is also utilized to disintegrate gas or liquid molecules to form sediments to modify substrate surface, which is a local nanochemistry reaction deposit process motivating by focused electron current.

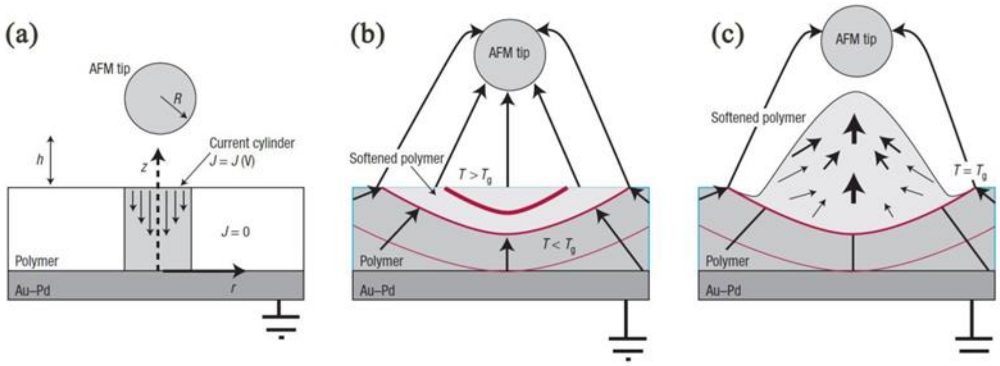

Figure 2.28 The schematics of mechanism of B-SPL [102].

2.3.6.2 Research status

To date, B-SPL technique has been widely implemented to fabricate a variety of polymers with accuracy ranging from 10 nm to 100 nm nanostructures for versatile application in the aspect of molecular electronics [105], numerous nanoscale sensors [106], and compute data storage [107]. Apart from this, the B-SPL method has been expanded to other samples, such as NaCl thin film coverd on the Au substrate surface [108][109], achieved GaAs/AlGaAs nanoline heterostructure on the Si substrate surface [110], and various solvent liquids including alcohol, dioxane and octane [111][112][113]. Additionally, an electronic current created by bias voltage is used to limit various chemical reactions and to decompose the deposition of gases or liquid molecules or the growth of materials on the surface. For example, the Garcia et al.[114] obtained a sub-25 nm accuracy carbon nanodots structure on Si substrate surface by employing the B-SPL method to transfer the CO_2 gas under voltages ranging from 10

V to 40 V, as shown in Figure 2.29 (a). Figure 2.29 (b-c) shows the achieved nanodots structure under different processing time with 21 V and different voltages under 0.1 ms, repectively. Moreover, the nanodots structure could be extended to the scale of the square centimeter area. Another key example of this method is the periodic lines with a pitch of 1 μm, 80 nm width and 0.32 nm height have been observed by employing a high conductivity tungsten carbide K-TEK tip across a thin polymer film and applying 18 voltages [102].

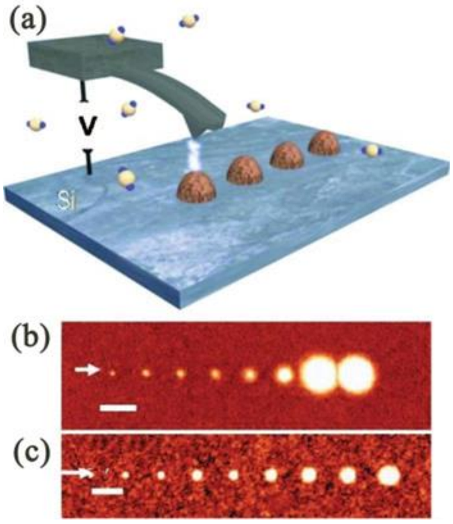

Figure 2.29 (a) The schematic of B-SPL for carbon nanodots structure. (b) The achieved nanodots structure under different processing time 0.1 ms, 0.5 ms, 1 ms, 10 ms, 50 ms, 100 ms, 1s and 2s with 21 V, respectively. (c) The achieved nanodots structure under different voltages 20 V, 22 V, 24 V, 26 V, 28 V, 30 V, 34 V, and 36 V under 0.1 ms, respectively [114].

2.3.6.3 Merits and drawbacks

In terms of the merit, the B-SPL method has the capability to employ the electric field to realize the nanoscale fabrication of polymer film surface topography. For processing polymers, it is a physical fabrication process and no chemical reaction exist. The polymer will not be degraded and have any abrasion. The polymer is only to be transported under the effect of high electric field and then achieves the nanostructure without the external thermal source. The B-SPL method is quite suitable for creating the nanostructures in the polymer film surface, yet the achieved product is not stable and homogeneous easily. Due to decomposition of gas and solution molecules, this process has expanded itself to nanochemistry domain. The deposit induced by electrochemical reactions can be created on various substrate surfaces and is more stable and robust. In spite of this advantage, the deposit process is time consuming and the throughput is low. Furthermore, the mechanism of control nanochemistry reactions and bias voltage between tip's apex and substrate surface has not been fully understood yet.

2.3.7 Mechanical scanning probe lithography

2.3.7.1 Fabrication mechanism

Mechanical scanning probe lithography (M-SPL) prompts the selective removal of materials from the substrate surface by several nanonewtons mechanical force applied at the probe by means of plowing and cutting via atomic force microscope (AFM) [115]. To sum up, this technique can be categorized into two work types depending on AFM scanning mode. When AFM works in the contact mode, the interaction force between tip and substrate surface with a magnitude ranging from 10^{-8} to 10^{-11} N will be enlarged through adapting a larger cantilever deflection. The tip will act as a cutting tool. With enough normal force it is capable of inducing plastic deformation of substrate surface and then remove material thorough further shearing.

During this nanomachining process, the tip is kept in a translational motion by presetting the normal force and program. This process is named as static plowing lithography, as shown in the left side in Figure 2.30. When AFM works in the tapping mode, as illustrated in the right side of Figure 2.30, a bigger amplitude will be applied in the cantilever and makes the cantilever achieve approximately to its resonant frequency. Subsequently, the substrate surface can be modified by continuous hammering or indenting process comparing to shearing nanomachining in the static plowing lithography. This process is, therefore, called dynamic plowing lithography. Both AFM working modes enable the M-SPL approach easy to operate through directly writing on the workpiece surface.

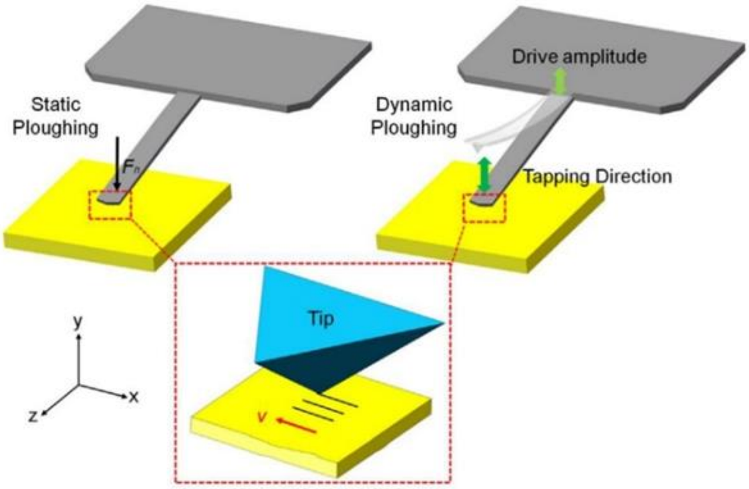

Figure 2.30 The schematics of the static ploughing lithography (left side) and dynamic ploughing lithography (right side) material removal [116].

2.3.7.2 Research status

To date, the M-SPL approach is innumerably applied in patterning metals, semiconductors, and polymers. Researchers can employ this method to obtain 2D and even 3D nanostructures. At present, static plowing lithography working under AFM scanning mode has been broadly employed to early nanoscratching experiments investigations, in which the diamond tip with high elastic spring constant up to 100-300 N/m and range of 30-50 nm [117] probe radii is usually used to fabricate nanoscale structures. For example, in terms of 2D patterns, many scholars initially employ piezoelectric actuator and so-called closed-loop system of the AFM itself to fabricate arbitrary nanostructures by means of controlling different feedback gain and scanning speed. Hyon et al. [22] achieved a sub-20 nm width nanoline with nearly 1nm depth on the GaAs surface. Wendel et al. [118] succeeded in ambient conditions and prepared 16 nanoscale holes array with 55 nm periodicity GaAs/AlGaAs heterostructure substrate as shown in Figure 2.31 (a). Furthermore, they also accomplished a smaller down to 35 nm nanoscale holes array. The diameter of these holes could be several nanometers. Afterwards, Schumacher et al. [119] continued to use this approach to machine GaAs/AlGaAs heterostructure with 50 ~ 100 μN contact force under 100 μm/s scanning speed for obtaining a channel barrier and insulated gate which is illustrated in Figure 2.31 (b). These works opened up the application market for single-electron transistor fabrication with single-gate and quantum electronic nanocomponents integration production. The M-SPL approach can not only pattern on the target substrate surface directly but also can combine with other nanolithography techniques, such as lift off process, wet chemical etching, and dry etching, reaching the purpose of machining nanostructures on the various material surface, such as Figure 2.31 (c) shows a single-electron transistor fabrication process using the mixture of M-SPL approach, dry etching and lift off process [120].

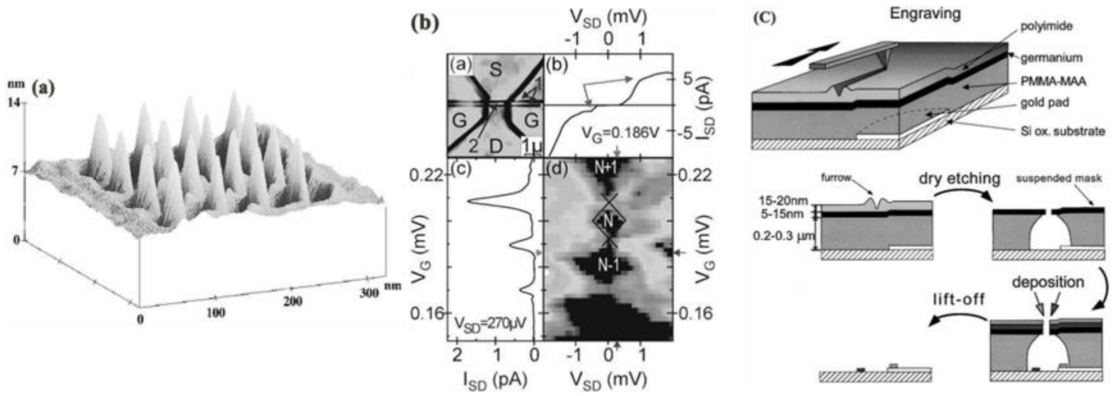

Figure 2.31 (a) The inverted topography of the 16 nanoscale holes array with 55 nm periodicity. (b) The image of the channel barrier and insulated gate. (c) The process of a single-electron transistor fabrication using the mixture of mechanical based on AFM fabrication approach, dry etching and lift off [118].

However, it is very challenging to realize the aforementioned complicated 2D and 3D nanostructures fabrication by using AFM or similar platform. For example, Lee et al. put forward a system which was the same with the AFM system and could use the diamond tip to scratch the material surface achieving regular and complex structures. However, these structures have low form accuracy of micrometer level owning to the large several milli newton force exerted by the system and the large tip radius up to several micrometers [121][122]. In view of this, one longitudinal study by Yan et al. came up with a CNC nanoscale 3D worktable which was based on commercial AFM and a high precision stage. The high precision stage is controlled accurate movement by another external computer. During the fabrication process, the tip is fixed into the substrate surface with a preset force and then the high precision stage starts to move according to the preset requirement. As a consequence, the complicated 2D and 3D nanostructures can be accomplished[123].

A seminal study in this research area is the work of 3D patterns and the M-SPL is similar to the traditional cutting process, which can realize the processing of 3D nanostructures. The specific characteristic of the M-SPL is its capability to precisely control the machining parameters at the nanometer scale and microsecond timescale during the pattering process. A 3D polymer bundle structure similar to traditional sinusoidal structure, as shown in Figure 2.32, has been obtained using a single crystal silicon cantilever with an elastic spring constant of up to 200 N/m on the polycarbonate (PC) surface through a single scanning. Additionally, a greyscale 3D human face within a frame size of 20 μm×20 μm was written on a polished Al disk sample with a 9.8 nm Ra and the time consumed was less than 10 mins [124]. Moreover, Mao et al. [125] accumulated the sample material on one side by controlling the trace of the probe to form a 3D structure. Based on this method, a 3D micro-Taiwan island pattern was successfully fabricated, as shown in Figure 2.33.

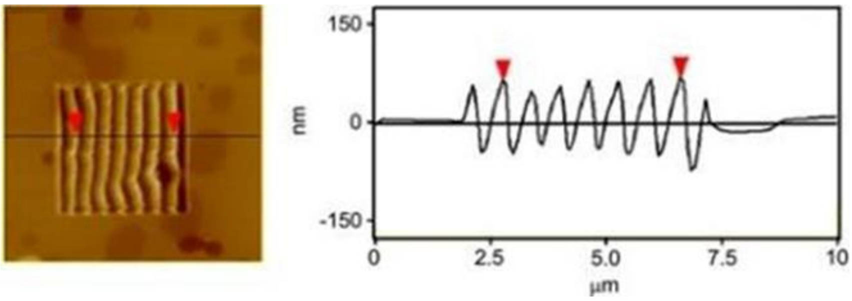

Figure 2.32 Morphology and the intersecting surface of the substrate under one time scanning with a normal load of 13.6 μN [126].

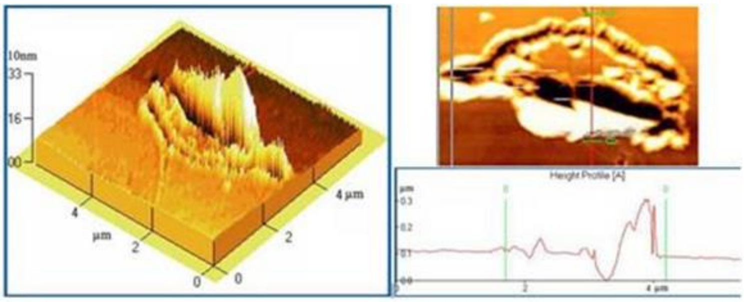

Figure 2.33 The 3D Taiwan island image [125].

In contrast to static plowing lithography, dynamic ploughing lithograph has drawn more researcher's interest in recent years for creation of 3D features and repair of advanced lithographic masks as it eliminates lateral force effect that can cause subsurface damage and has the advantage of non-ridge for nanogrooves fabrication. So far, this technique has been focusing on the polymer, graphene and metal pattern by using silicon or silicon nitride cantilever with the elastic spring constant of 10-100 N/m and the probe's radii on the order of 10-30 nm. For example, Figure 2.34 demonstrates various 3D nanodots can be fabricated on the soft PMMA thin film by employing dynamic plowing lithography approach [127][128]. In addition, Borislav et al. [129] used dynamic plowing lithography to tailor and manipulate the geometry of graphene avoiding the disadvantages of uncontrollable crumbing, dragging, and ripping from static plowing lithography. Meanwhile, Yan et al. [130][16] carried out dynamic ploughing lithography experiments on single crystal Cu and found that the machining direction of tip significantly influences for the obtained achieved depth and pile-up sidewalls of nanogrooves. Furthermore, Xiao et al. [116] compared static plowing lithography and dynamic ploughing lithography for machining Cu and revealed that less chip formation and smaller feature size were observed in the dynamic ploughing process.

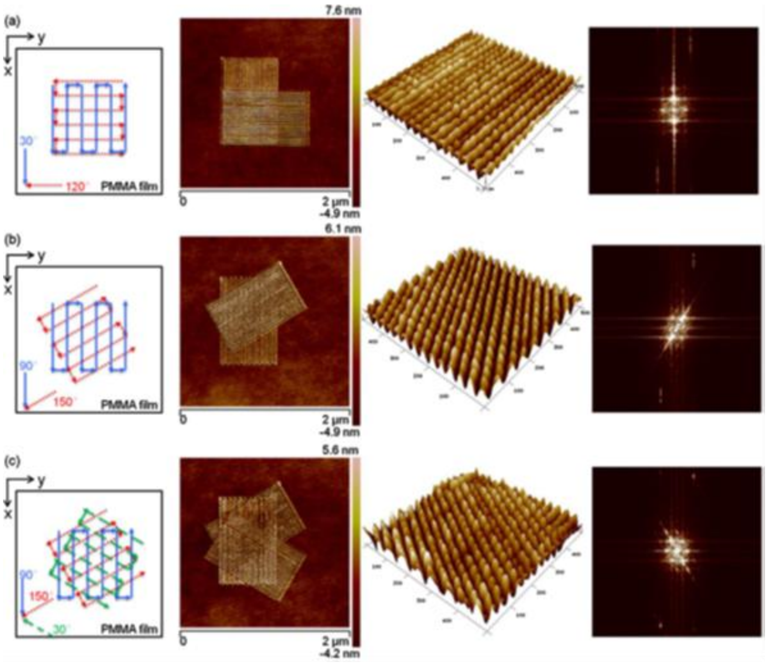

Figure 2.34 The image of various nanodots and FFT images. (a) Checkerboard nanodots from 30◦ and 120◦ machined directions. (b) Diamond-shaped nanodots from 90◦ and 150◦ machined directions. (c) Hexagonal nanodots from 30◦, 90◦ and 150◦ machined directions [128].

2.3.7.3 Merits and drawbacks

In brief, M-SPL is a promising method in the advanced nanomachining based on AFM. The method is simple to use and possesses excellent control ability under own nanomachining software package for achieved patterns and can be performed under the conditions of ultra-vacuum, atmosphere, liquid, low temperature, normal temperature and high temperature and does not require complicated machines. In addition, the size of mechanical machined structures can approach nanoscale. Nonetheless, the limitation in making consistent structures is the stability of the probe, which is subject to deformation and contamination by the debris of the removed material. Inevitably, The M-SPL, as a mechanical machining approach, will result in the subsurface damage (SSD) in the cutting zone which will degrade the component life. Normally, a following post machining operation is required to remove the SSD, such as chemical etching and chemo-mechanical polishing. What’s more, when certain nanostructures need to be produced in mass production or require a more smooth surface, such as refined 3D sphere surface, the M-SPL requires to combine with other nanomachining methods, like electron beam lithography (EBL), nanoimprinting lithography technique (NIL), and focused ion beam fabrication (FIB). Moreover, the probe of AFM will go along with fast wear when machining some semiconductor metals, particularly for the silicon or silicon nitride probe. Finally, the mechanism of material atom scale removal still demands further study.

2.3.8 New scanning probe microscope tip-based nanomachining approaches

The flexibility and versatility of scanning probe microscopy to direct writing and deposit surfaces have created some other methods such as dispensing approach by SPM tip-based, ultrasonic vibration assisted approach by SPM tip-based and magnetic approach by SPM tip-based. Dispensing based on SPM fabrication utilizes a cantilevered nanopipette, which is hollow, to replace the probe of a scanning probe microscope. The jet-flow tube can directly deliver soluble molecules to any surface. For example, protein featuring as small as 200 nm [131] and single living cells under physiological conditions [93] can be dispensed to sample surface by using dispensing by SPM tip-based fabrication method. What’s more, the Deng et al. [132][133] employed the ultrasonic vibration technique to assist the nanomachining by SPM tip-based. They kept the high frequency vibration in the XY work stage and high ultrasonic vibration in the Z tip direction. Then, the 3D concave and stair-stepping nanostructures could be obtained within several minutes on the PMMA surface. Recently, a magnetic approach by SPM tip-based is to use the magnetic force microscope (MFM) to realize the microstates accessing of the artificial spin ices (ASI) and relevant noninteracting nanomagnets arrays by writing the topological defects into magnetic nanolines directly [134]. Much more interestingly, a novel tip-based electron beam induced deposition (TB-EBID) technique has most recent proposed to fabricate single electron devices with the low energy beam [135].

2.4 Comparison

Table 2.1 summarizes the comparison of the machining capabilities of the SPDT and SPL approaches. SPDT is an excellent candidate for mass production with excellent control ability of machining accuracy in large area. However, the SPDT process struggled to achieve sub-10 nm resolution due to limitation on the attainable size of the diamond tools. Given the fact that the feed mark left by the tool on the machine surface can cause interference pattern, SPDT can only be used as a manufacturing protocol for IR optics and some electronic devices. ACSM technique is capable of machining atoms with atomic scale resolution. However, the ACSM technique is time consuming and requires complex machining environment. O-SPL has achieved sub-5 nm fabrication resolution among these techniques. Due to its high reliability and sub-5 nm fabrication resolution, the fabricated nanostructures can be used as key nanocomponents of electronic devices and templates in subsequent etching or deposition work processes. However, the O-SPL concentrates on the pattern of high oxidizability of substrate materials, which confines the application scope of this technology to a certain extent. In terms of tip wear, the ACSM, O-SPL, D-SPL and B-SPL have relatively long tip life. However, the D-SPL is more complicated fabrication technology with very limited control ability [92] to deposit polymer materials or biomolecules onto substrate. Meanwhile, B-SPL involves the physical process for polymer modification and nanochemical process for decomposing gas and solution molecular. The throughput of B-SPL is very low because the material transformation and chemical reactions are very time consuming under high electric fields. In addition, both t-SPL and tc-SPL have less tip wear than M-SPL because the heat effect can soften the substrate material and make it easier to cut. In particular, the t-SPL and tc-SPL are more effective to process thermosensitive materials. As opposed to t-SPL and tc-SPL, M-SPL has the capability to fabricate more wide and diverse material and breaks through the thermosensitive material limitation in the nanolithography with high control ability. However, the sub-surface damage (SSD) in the cutting zone during M-SPL process can cause fatigue and creep of the obtained component. Therefore, a second post machining operation is requirement to eliminate the SSD, e.g., chemical etching and chemo-mechanical polishing. Moreover, inevitable tip wear of M-SPL is still a long-standing challenge to overcome.

Table 2.1 Comparison of machining capabilities of SPDT and SPL approaches.

Items	**SPDT**	**ACSM**	**T/tc-SPL**	**O-SPL**	**M-SPL**	**D-SPL**	**B-SPL**
Resolution	~60 nm [141]	Atomic scale [17]	<10nm [74]	<5nm [139]	<10nm [138]	<50nm [63]	<10nm [136]
Throughput	一	一	~10^4μm^2 h^{-1} [140]	~10^2μm^2 h^{-1} [55]	~2.4×10^3μm^2 h^{-1} [100]	<10^4μm^2 h^{-1} [87]	<10μm^2 h^{-1} [137]
Machining capability	2D,3D	一	2D,3D	2D, 3D	2D, 3D	2D	2D
Machinable materials	Soft material, Semiconductors	Molecular, Atoms, Electrons	PMMA, PC PPV film, Copolymer film	Metal, Semiconductors, Graphene, Polymer	Polymer, Metal, Ceramics and Semiconductors, Graphene	Polymers, DNA, Proteins and Metal ions	Graphene, Metal, Semiconductors, Polymer
Environment	Air	Vacuum	Liquid, Air	20%-80% relative humidity	Air	34% relative humidity	High electric fields
Speed	Fast	Slow	Fast	Fast	Fast	Fast	Slow
Control	Excellent	Difficult	Good	Excellent	Excellent	Complicated	Difficult
Principle	Physical process	Physico-chemistry process	Physico-chemistry process	Chemical process	Physical process	Chemical process	Physico-chemistry process
Tip wear	Serious	Negligible	Not serious	Negligible	Serious	Negligible	Negligible

Looking beyond, SPL technique has already demonstrated remarkable fabrication capabilities for 2D/3D nanostructures, nanocomponents and even single atom memory device. It has been successfully applied to quantum computing, nanoelectronics and nanofluidics devices. However, there are still two major challenges which hamper on the commercialization of SPL technique.

The first challenge is the low processing efficiency. SPL technique is based on an SPM platform which is basically designed for measurement purpose in the lab environment. Due to the high precision requirement, SPL technique is only used for proof-of-principle experiments so far instead of mass industrial production. For example, researchers manufactured quantum wells and single electron transistors (SET), which only proved that the machining precision of the SPL technique can meet the requirement of the above-mentioned nano-electronic device. In order to move toward industrial application, a necessary prerequisite is to enhance the processing efficiency dramatically. To solve this problem, the concept of “millipede” has been proposed using a parallel microcantilever-probe array (1024×1024) to achieve ultra-high-density nanodots[142][143]. Second, a mix-and-match lithography approach by combining SPL technique and existing nanomachining techniques [144], such as wet etching, dry etching, lift-off process, NIL, FIB and EBL, will be a better choice to approach mass industrial production[76]. Another challenge is the smallest achievable feature. The processing structure is restricted by the size of the tip radius of the microscope tip. With regards to the achieved nano-dot/line, nano-groves and 3D nanostructures, albeit the height or depth of the nanostructure is small, only up to 1-2 nm. The width is confined to the tip radius that is currently around 30-50 nm and it is difficult to further reduce its size. In response to this problem, some researchers have proposed to use even sharper tips. However, the wear of sharp tips increased dramatically during the machining process. More importantly, this method only improved the machining precision of single nanostructures without any improvement of the processing efficiency. Therefore, on the premise of ensuring the processing efficiency, the further reduction of the lateral dimension of the nanostructure is a thought-provoking question to realize industrial scale production.

2.5 Previous MD simulation investigations on the nanometric cutting

With the rise in the developments of parallel computing and the latest advances in high-performance computing, Molecular Dynamics (MD) simulation has been establishing new horizons in the field of precision solid freeform fabrication and can reveal details that are not easily accessible from the experiments [145]. MD simulation method, as a significant theoretical calculation technique, can provide a fundamental understanding for AFM-based machining material removal mechanism and tremendously facilitate the development of nanomachining high quality structured surface. These built tip models which are generally set diamond lattice, such as conical shape, square pyramid shape, triangular pyramid shape, and classic sphere shape. Up to now, MD simulation investigation of AFM-based machining has been focusing on two aspects mimicking practical machining: (1) indentation simulation, (2) scratching simulation. The indentation simulation is normally used to study the relationship of indentation force and indentation depth. While more information can be extracted in the scratching simulation, e.g. machining zone temperature, cutting zone stress, coordination number data, dislocation data, bond-angle data, and common neighbor data. Numerous works reported MD simulation of AFM-based machining on metal (such as copper [146], aluminum [147], iron and silver [148], gold [149]), semiconductor materials (Si [150], SiC [151]), polymer (PMMA) [152], and muti-layer graphene [153].

In terms of metal copper of AFM-based machining, Geng et al. [154] simulated constant normal force mode-based AFM-based machining process, as shown in Figure 2.35 (a), and studied anisotropic effect on the (010), (110), and (111) and found that the dislocation slip was the main deformation phenomenon of plastic deformation zone and the (110) achieved the highest copper atoms pile-up size. Furthermore, Xiao et al. [116] emulated the tapping mode AFM-based (dynamic ploughing lithography), as shown in Figure 2.35 (b), and constant height mode-based AFM-based (static ploughing lithography) discovered the dynamic ploughing machining could achieve smaller feature size nanogroove, as shown in Figure 2.35 (c). All these works have been validated by experiments.

Specifically, Yan et al. [130] implemented the tapping mode AFM-based simulation to investigate the effect of tip orientation during single crystal copper machining. They concluded the tip orientation played a pivotal role for machining depth, cutting force and material pile-up in the dynamic ploughing lithography. Much more interestingly, they uncovered the face forward machining had more intensive backwards slipping phenomenon than edge forward machining and side face forward machining. Additionally, Zhang et al. [155] investigated the deformation twining mode of nanocrystalline copper during static scratching process and found that nucleation and interaction between dislocation slip and grain boundary were the dominant deformation mechanism for nanocrystalline face centered cubic (FCC) copper material.

The grain boundary could not only inhibit the dislocation motion but also assimilate achieved dislocation.

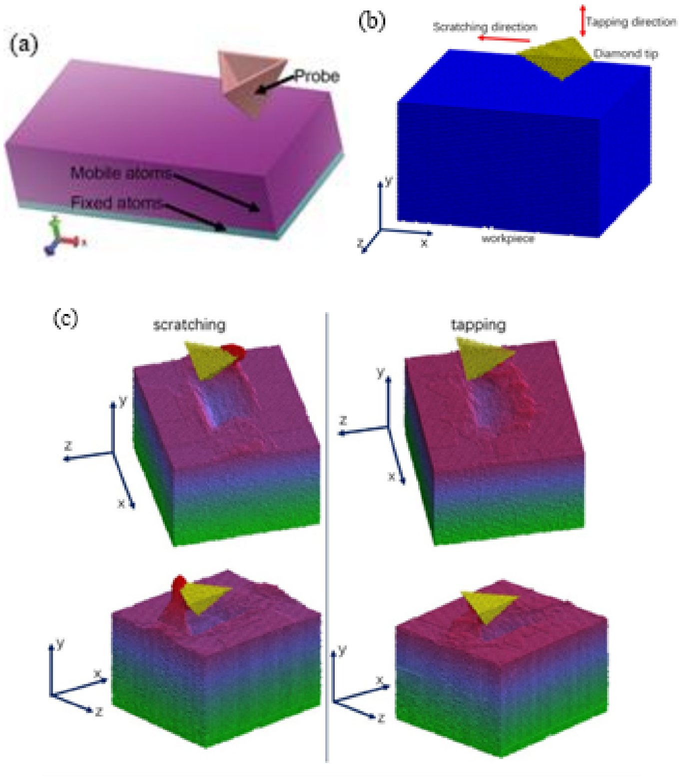

Figure 2.35 (a) constant force mode-based model [154] (b) tapping mode-based model [116] (c) nanogroove image for the static and dynamic machining.

With regards to semiconductor Si materials, Dai et al. [150] carried out constant height mode-based MD experiments with different angle conical shape tip tool (see Figure 2.36 (a)) and found a larger tip angle could create larger chip volume and cause larger subsurface damage and lead to higher cutting forces. Meanwhile, Si workpiece temperature distribution and atom stress, including hydrostatic stress and von Mises stress, were also investigated, which are indicated in Figure 2.36 (bcd). These spatial distribution analysis techniques can effectively demonstrate evolution process with tip tool machining and validate the correctness of simulation by mutual contrast.

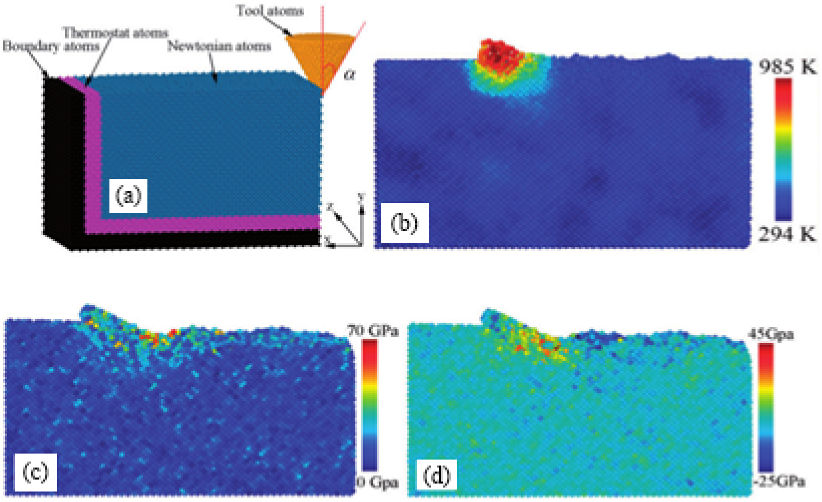

Figure 2.36 (a) MD simulation model (b) The machined Si workpiece temperature distribution (c) The machined Si workpiece hydrostatic stress distribution (d) The machined Si workpiece von Mises stress distribution.

Additionally, various MD investigations have been conducted for silicon carbide material. Noreyan et al. [156] simulated nanoindentation process of diamond tip on the cubic silicon carbide (β-SiC) model surface and found that the critical depth of elastic-plastic transition had very weak relation with indenter velocity and workpiece temperature and critical pressure experienced decline with tip width rising. Furthermore, Yao et al. [151] carried out scratching MD experiments of polycrystalline silicon carbide established by Vornoni site-rotation method using a diamond grit similar to sphere shape tip and revealed the removal mechanism of polycrystalline silicon carbide including amorphous transition, intergranular crack transition, and transgranular crack transition. Also, they discovered that hexagonal diamond structure and some dislocations were created around the grain boundary with scratching.

According to constant height mode-based PMMA machining simulation, Yuan et al. [152] revealed the removal mechanism of PMMA was a ductile plastic deformation manner as machining zone temperature was larger than the glass transition temperature of PMMA. Additionally, Zhang et al. [153] studied the multi-layer graphene frictional mechanism by changing machining depth and concluded that the machining depth 5.3 Å was the frictional behavior turn point. When machining depth was less than 5.3 Å, the graphene demonstrated super easy machining characteristic. Thus, it can be seen that lots of material properties and deformation and removal mechanism investigations have been presented by MD simulation. To sum up for static and dynamic simulation, a larger machining depth parameter can cause more subsurface damage, material deformation and chip pile-up and lead to larger cutting forces which is due to contact with more substrate atoms. Meanwhile, a higher machining speed can lead to higher machining resistance. While the achieved surface underneath tip tool can obtain less subface damage which is attribute to the elastic deformation of the subsurface recovering apace with high machining speed. However, these works consider diamond tip as a rigid body and neglect tip wear which is not according to the actual situation.

With regarding to MD simulation study of hot machining, it has primarily concentrated on silicon (Si) and silicon carbide (SiC). For example, a comparison study of hot machining of SiC with conventional machining was investigated and revealed that the hot machining could lead to lower tangential cutting forces, lower shear stress and von Mises stress acting on cutting tool edge, however, the shear plane angle stayed invariant. A major concern related to the hot machining is the likelihood of graphitization of the diamond tool which can accelerate its wear [157]. Moreover, dislocation nucleation and amorphization-based plasticity mechanisms were proposed during hot machining of SiC at temperatures up to 3000 K. A variation in the dislocations behaviour including the formation of multi-junction, Frank-type sessile and stair-rod partials were found when cutting was carried at temperatures above 900 K [158]. Furthermore, specific cutting energy of SiC showed an increase at cutting temperatures up to 1400 K and a gradual decrease at higher temperatures of 1700 K and 2000 K. Hot nanometric cutting of SiC on different crystal orientations was also investigated. A phenomenon of cleavage was observed in all cases during the cutting of the (111) oriented SiC [159]. During the hot machining of Si, the rotational flow of Si underneath the diamond tool similar to the vorticity became more pronounced [160]. Moreover, the depth of sub-surface damage and the volume of cutting chips (number of atoms) became more significant with higher pre-heating temperature [161], in the meanwhile, the atomic von Mises shear strain zone in the primary shear zone became wider [162]. Furthermore, few stacking faults were seen to grow during the hot machining of Si [163].

It is commonly known that GaAs (Zinc blende lattice structure) has a different lattice structure from Si (diamond lattice structure) and SiC (hexagonal lattice structure) due to different order of atoms stacking. The research so far on GaAs has remained focused on the experimental study of room temperature machining for nanogrooves [22], single-electron transistor [164] or modulation-doped field effect transistor (MODFET) [165] and to explore the origins of ductile-mode machining of GaAs [7]. To date, there exists no evidence from the literature describing the nanocutting performance of GaAs.

2.6 Summary

High-throughput and high-accuracy nanomachining methods have been of the great demand for the ever-increasing needs of nanoelectronics, high density data storage devices, nanophotonics, quantum computing, molecular circuitry and scaffolds in bioengineering used for cell proliferation applications. This chapter has provided readers with an overview of SPDT and SPL technique. In particular, this chapter introduced ACSM technique, which is one of the critical nanomachining methods with great potential to evolve into a disruptive atomic scale fabrication technology to meet the future demand. The effects of thermal, chemistry, electric field, magnetic and mechanics between the functionalized tip and substrate within SPL technique are the key focuses of this review chapter. The overall status can be summarized as follows:

- SPDT is a superb candidate for ductile-regime nanomachining of GaAs and can be utilized for mass production.
- In terms of atomic scale machining, ACSM technique is one of the critical nanomachining methods with great potential to evolve into a disruptive atomic scale fabrication technology to meet the future demand for atomic devices. However, ACSM has not been competent for achieving complex functional atomic structures. The research has been focusing on the atomic manipulation and molecular transformation aspects.
- SPL technique is a simple and unique technique, which is positioned with low cost, nano/atomic scale precision and maskless straightforward writing on the substrate by means of various chemical, physical, diffusive and deposition mechanisms.

- SPL technique has been restricted to laboratory level to fabricate the fast prototyping of nanodevices and nanoscale components, which is long standing challenge to enable commercialization of SPL technique.
- A mix-and-match lithography approach by combining SPL technique and existing nanomachining techniques is extended as a significantly cost-effective manner for contemporary mass nanomachining production.

Additionally, the research status of MD simulation on nanometric cutting was also described in detail. The previous study has mainly concentrated on cutting of silicon, silicon carbide and copper. The GaAs, which resides in a Zinc-blende structure, is worthy of investigation to perform in a MD simulation platform. Significantly, knowledge gaps were discovered such as what is the incipient plasticity, how does the sub-surface damage form, and the diamond cutting tool wear during nanomachining of GaAs and how is the machinability in thermally-assisted nanomachining. These knowledge gaps are urgently to be addressed in order to guide ductile regime nanomachining of GaAs.

Chapter 3 Modelling and Simulation of Nanomachining Process

3.1 Introduction

With the rise in the developments of parallel computing and the latest advances in high-performance computing, MD simulation has been establishing new horizons in the field of precision solid freeform fabrication and can reveal details that are not easily accessible from the experiments [145]. Furthermore, Molecular dynamic (MD) simulation has been proved to be a reliable theoretical approach to overcome the restriction of experimental observation to study ultra-precision machining of brittle materials [166]. It is capable of simulating structural characteristics of the work material at the atomic scale, which makes it possible to predict the motion and behavior of material atoms. Therefore, this thesis employed MD approach to systematically elucidate an atomic insight of GaAs compound semiconductor. In this chapter, the generic scheme of performing MD simulation is described in detail, such as boundary conditions, ensemble, workpiece and tool geometry definition, selection of potential function, post processing tools.

3.2 MD simulation model

This thesis established the MD simulation model for AFM tip-based nanomachining and MD simulation model for SPDT of single crystal/polycrystalline GaAs, as shown in Figure 3.1 (a) and Figure 3.1 (b). For AFM tip-based nanomachining model, the diamond tip with (1 0 0) crystallographic plane was set as a non-rigid body aiming to study the wear mechanism of diamond tip during nanomachining of GaAs. For SPDT model, the diamond cutting tool has a negative rake angle of -25°, a clearance angle of 10° and a tool nose radius of 2 nm. The polycrystalline GaAs workpiece was built by employing the Atomsk software [167] using the Voronoi algorithm [168]. The Voronoi site-rotation method generates a polycrystalline structure by joining the normals of the line of random discrete points at the crystal boundary and containing the growing random oriented crystal seeds [169]. The single crystal/polycrystalline GaAs consists of newton atoms, thermostat atoms and boundary atoms, whose initial temperature was maintained at 300 K by using the Nose-Hoover method [170] running for 50 ps. Periodic boundary condition was applied in the X and Z directions and shrink-wrapped boundary condition was set for Y direction. It should be noted that the force components along the X, Y and Z directions referred to as tangential cutting (*Fx*), thrust or normal force (*Fy*) and axial force (*Fz*), respectively. In order to make the MD simulation consistent with the real situation as much as possible, the model is usually simulated under certain environmental conditions, e.g. ensemble. The MD simulations was controlled under the NVE ensemble with constant the number of atoms (N), volume (V) and conserved total energy (E). The MD simulations were implemented in the open source code, named as “Large-scale atomic/molecular massively parallel simulator” LAMMPS [171]. The MD simulations were performed on the ARCHIE-WeSt High-Performance Computer and ARCHER2 High-Performance Computer (HPC) of the UK [145] with about 12800 cores (each node on ARCHER2 has about 128 cores). Additionally, the typical crystallographic planes of GaAs substrates e.g. (0 0 1), (1 1 0) and (1 1 1) were selected to investigate the influence of crystalline orientation during nanomachining process. Schematic of various crystallographic planes and the cutting directions is shown in Figure 3.2. The elevated temperature of GaAs substrate was set from 300 K to 1200 K below the melting point (1511 K) of GaAs. The simulation parameters are shown in detail in Table 3.1.

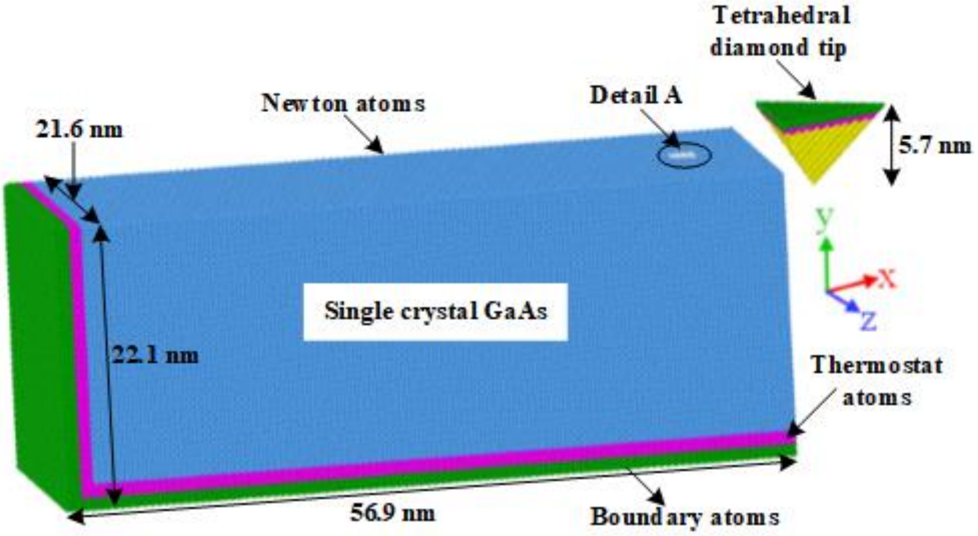

(a) MD simulation model for AFM tip-based nanomachining of single crystal GaAs.

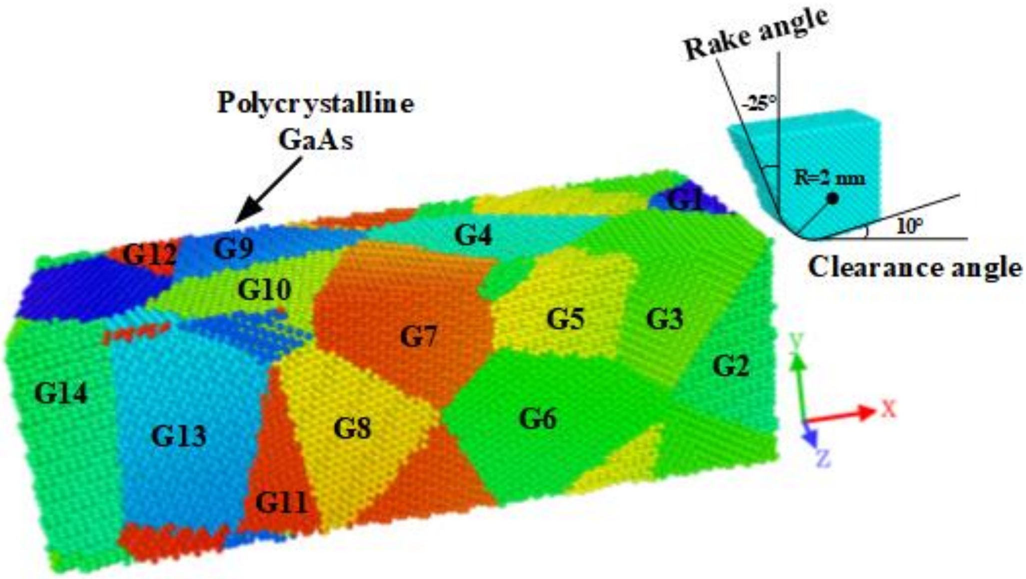

(b) MD simulation model for SPDT of polycrystalline GaAs.

Figure 3.1 Nanoscratching model showing single crystal/polycrystalline GaAs and tool description.

Table 3.1 MD simulation model and conditions.

Substrate material	Single crystal GaAs (SC GaAs) Polycrystalline GaAs (PC GaAs)
Substrate dimensions	SC GaAs: 56.9 × 22.1 × 21.6 nm^3 PC GaAs: 30.8 × 10.0 × 13.4 nm^3
Machining tool material	Single crystal diamond
GaAs lattice constant	5.65 Å (Zinc blende lattice structure)
Diamond lattice constant	3.57 Å (Diamond cubic lattice structure)
Depth of cut	3 nm
Width of cut	1.7 nm
Crystallographic plane of GaAs substrate and cutting direction	Case 1: (0 0 1) along [1 1 0] Case 2: (1 1 0) along [0 0 1] Case 3: (1 1 1) along [1 $\bar{1}$ 0]
Cutting velocity of the tool	50 m/s
Substrate initial temperature before cutting	300 K, 600 K, 900 K, 1200 K
Temperature of the diamond tip	300 K in all MD simulation cases
Boundary conditions	Periodic, shrink-wrapped and periodic along the X, Y, and Z directions respectively
Timestep of MD calculation	1 fs

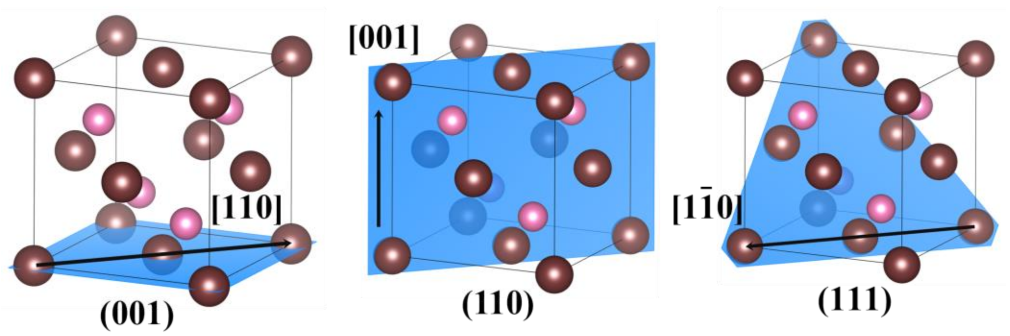

Figure 3.2 Schematic of various crystallographic planes and the cutting directions.

3.3 Potential function

In this thesis, the force field consisted of a hybrid scheme such that the Tersoff potential function (C-C interactions), updated Bond-Order Potential (BOP) function (Ga-As interactions) and Ziegler-Biersack-Littmark (ZBL) potential function (for cross interaction between carbon with GaAs atoms) were respectively employed. The classical Tersoff potential function [172] was selected to describe the C-C interactions in the diamond machining tool [166]. The calculations of a Tersoff potential function are shown in below equations [150].

$$E = \sum_{i=j} V_{ij} \tag{3-1}$$

$$V_{ij} = f_C(r_{ij})[f_R(r_{ij}) + b_{ij} F_A(r_{ij})] \tag{3-2}$$

$$f_R(r_{ij}) = Aexp(-\lambda r_{ij}) \tag{3-3}$$

$$f_A(r_{ij}) = -Bexp(-\mu r_{ij}) \tag{3-4}$$

$$f_C(r_{ij}) = \begin{cases} 1 & r_{ij} < R \\ \frac{1}{2} + \frac{1}{2}\cos\left[\pi \frac{r_{ij}-r}{S-R}\right] & R < r_{ij} < S \\ 0 & r_{ij} > R \end{cases} \tag{3-5}$$

$$b_{ij} = (1 + \beta_i^n \delta_{ij}^n)^{-1/2n} \tag{3-6}$$

$$\delta_{ij} = \sum_{k\neq i.j} f_c\left(r_{ij}\right) g(\theta_{ijk}) \tag{3-7}$$

$$g\left(\theta_{ijk}\right) = \frac{(1+c^2)/(d^2-c^2)}{\left[d^2+\left(h-\cos\theta_{ijk}\right)^2\right]} \tag{3-8}$$

Where E represents the system total energy, the V_{ij} refers to bond energy in the whole atomic bonds, i, j, and k mean the atomic label of the system, f_C is a smooth cutoff function to restrain the range of the potential, f_R is a two-body term, r_{ij} represents the length function of the i and j bond, b_{ij} means the bond order term, F_A consists of the three-body interactions, f_A and f_c are the attractive pair potential and smooth cutoff function, respectively. δ_{ij} refers to the atom number in which the atoms i besides the ij bond. The θ stands for the bond angle.

The interaction of the GaAs workpiece (Ga-Ga, As-As, and Ga-As) was calculated by using the updated Bond-Order Potentials (BOP) potential function based on quantum mechanical theory. BOP potential function, as shown in equation (3-9) is especially suitable to govern gallium arsenide system. Because it considers an electron counting potential which is used to address the distribution of electrons on the GaAs surface. Additionally, the prediction of the structural changes and binding energy trends through BOP potential function matches experimental observations well [173][174]. The repulsive and bond integral terms were calculated by Goodwin-Skinner-Pettifor (GSP) function [175]. The detailed BOP potential function parameters used in this thesis are shown in appendix B.

$$\mathrm{E} = \frac{1}{2}\sum_{i=1}^{N}\sum_{j=i_1}^{i_N}\varphi_{ij}\left(r_{ij}\right) - \sum_{i=1}^{N}\sum_{j=i_1}^{i_N}\beta_{\sigma,ij}\left(r_{ij}\right)\cdot\theta_{\sigma,ij} - \sum_{i=1}^{N}\sum_{j=i_1}^{i_N}\beta_{\pi,ij}\left(r_{ij}\right)\cdot\theta_{\pi,ij} + U_{prom} \tag{3-9}$$

Where the r_{ij} is the distance function for interatomic i and j, $\varphi_{ij}\left(r_{ij}\right)$ is the repulsive energy and short-range two-body function, $\beta_{\sigma,ij}(r_{ij})$, and $\beta_{\pi,ij}(r_{ij})$ presents bond integrals, $\theta_{\sigma,ij}$ and $\theta_{\pi,ij}$ refer to specific bond-orders, U_{prom} determines the promotion energy about sp-valent systems. Following the BOP potential function, the cutoff was modified to 11.1 Å which could effectively speed up the inter-processor communication.

As Ziegler-Biersack-Littmark (ZBL) potential function [176] is suitable to calculate high-energy collisions accurately among C, Ga, and As atoms, it is employed to describe the occurrence of diamond cutting tool collision with GaAs workpiece edge, as follows in equation (3-10).

$$E_{ij}^{ZBL} = \frac{1}{4\pi\epsilon_0}\frac{Z_i Z_j e^2}{r_{ij}}\varphi(r_{ij}/a) + S(r_{ij}) \tag{3-10}$$

$$\mathrm{a} = \frac{0.46850}{Z_i^{0.23} + Z_j^{0.23}} \tag{3-11}$$

Where ϵ_0 refers to the electrical permittivity of vacuum, e means the electron charge, Z_i and Z_j are the nuclear charges of the two types of atom, r_{ij} is identical to mentioned above, $S(r_{ij})$ is a switching function which can limit the energy, force, and curvature down to zero smoothly within cutoff range. Moreover, the inner cutoff and outer cutoff were set to 3.0 Å and 4.0 Å, respectively.

3.4 Visualization tools

The visualization tools, such as OVITO and ParaView [177][178], are required to analyse the raw data of atomic configuration. OVITO is a scientific visualization and analysis software for atomistic and particle simulation data. It helps scientists gain better insights into materials phenomena and physical processes as a powerful tool to analyze, understand and illustrate simulation results. ParaView is a multi-platform data analysis and visualization application. It can make users quickly build visualizations to analyze their data using qualitative and quantitative techniques in the real time scale. The Dislocation Extraction Algorithm (DXA) [179][180] and Crystal Analysis Tool (CAT) [181][182] were employed to analyze the sub-surface defect cluster. The DXA transforms the original atomistic representation of a dislocated crystal into a line-based representation of the dislocation network. It determines the Burgers vector of each dislocation and identifies dislocation junctions. Crystal Analysis Tool was developed to analyze the output of atomistic simulations of solids (primarily crystals). The code implements algorithms to identify lattice structures and defect structures formed by atoms. It can compute the atomic level elastic and plastic deformation gradient fields to quantify plastic deformation and elastic lattice strains. Additionally, CAT can generate a geometric representation of the free surfaces of a solid and identify internal voids, measure surface area, porosity.

3.5 Post processing

In MD simulations, temperature is an ensemble property and cannot be calculated directly in LAMMPS. In this thesis, Equations (3-12) [183]–[185] was employed to compute the temperature of the diamond tip by conversion of average kinetic energy:

$$K.E. = \frac{3}{2} N K_b T \tag{3-12}$$

where $K.E.$ refers to the kinetic energy of the GaAs substrate atoms, *N* is the number of atoms, K_b is the Boltzmann constant.

In addition, the virial stress computation method [166] was used to compute the stress components of the GaAs substrate and diamond tip. It can be described as follows [186]–[188]:

$$\sigma_{ab}(i) = \frac{1}{N_A}\sum_i \left[\frac{m_i v_i^a v_i^b}{V_i} + \frac{1}{2V_i}\sum_j F_{ij}\frac{x_{ij}^a x_{ij}^b}{r_{ij}}\right] \tag{3-13}$$

where σ_{ab} refers to six direction symmetric stress components of each atom, *ab* represents x, y, and z, N_A is the number of atoms in an area A, m_i is the mass of the *i* atom, v_i^a and v_i^b mean the *a* component and *b* component of the *i* atom velocity, V_i is the volume of the *i* atom, F_{ij} is the force between the *i* atom and the *j* atom, x_{ij}^a and x_{ij}^b represent *a* direction vector and *b* direction vector of *i* atom and *j* atom, r_{ij} is the distance between the *i* atom and the *j* atom.

The hydrostatic stress (average of three principal stresses) and von Mises stress of GaAs substrate and diamond tip were further investigated, which could be calculated by equation (3-14) and equation (3-15), respectively [189]–[191]. In this case, the hydrostatic stress and von Mises stress were averaged over a 20Å box for each GaAs substrate atom.

$$\sigma_{hydro}(i) = \frac{1}{3}[\sigma_1 + \sigma_2 + \sigma_3] \tag{3-14}$$

$$\sigma_{von}(i) = \left\{\frac{1}{2}\left[\left(\sigma_{xx}(i) - \sigma_{yy}(i)\right)^2 + \left(\sigma_{yy}(i) - \sigma_{zz}(i)\right)^2 + \left(\sigma_{zz}(i) - \sigma_{xx}(i)\right)^2 + 6\left(\sigma_{xy}^2(i) + \sigma_{zy}^2(i) + \sigma_{xz}^2(i)\right)\right]\right\}^{1/2} \tag{3-15}$$

3.6 Summary

This chapter introduced MD simulation models for nanometric cutting, selection of potential function, selection of visualization tools and post processing of MD simulations results in detail. Both MD simulation models for AFM tip-based nanomachining of single crystal GaAs and SPDT of polycrystalline GaAs were established to investigate the mechanics of single crystal/polycrystalline GaAs. An analytical bond-order potential for GaAs was selected to allow one to model a wide range of properties of GaAs compound structures, as well as the pure phases of gallium and arsenide, including nonequilibrium configurations within the local density functional theory. Additionally, the prediction of the structural changes and binding energy trends through BOP potential function matches experimental observations well. The data obtained by LAMMPS was visualized by OVITO and ParaView tools. Dislocation Extraction Algorithm (DXA) and Crystal Analysis Tool (CAT) were employed to post-process the atomistic data.

Chapter 4 Nanomachining of Single Crystal GaAs

4.1 Introduction

To date, single point diamond turning (SPDT) [192]–[197] becomes a good candidate for manufacturing nanoproducts due to its capability of mass production of 2D and 3D nanostructures with high form accuracy in a single pass. Through establishing machining parameters to meet brittle-to-ductile transition condition, some researchers [29][31] have already successfully obtained nano-smooth machined surfaces on GaAs although it is regarded as a difficult-to-machine brittle material, attributed to its low elastic modulus and fracture toughness. However, so far, the underlying nanometric cutting mechanics of GaAs during SPDT has not been fully revealed yet, including the cutting forces, cutting zone temperature and its anisotropic machinability. This has significantly hampered the development of SPDT process for the manufacturing of 3D nanostructure on GaAs workpiece. This chapter employed MD simulation approach to systematically elucidate an insight of cutting forces of the diamond cutting tool, visualized temperature distribution of the cutting zone, and the anisotropic machinability during SPDT of single crystal GaAs. In addition, SPDT experiment was conducted to verify the MD simulation results qualitatively. Further SPDT of single crystal GaAs trial guided by the findings has verified the effectiveness of this simulated approach.

4.2 Single point diamond turning experimental setup

In order to verify the MD simulation results, SPDT of GaAs was carried out on an ultra-precision diamond turning machine equipped with air bearing slides and spindle. The experiment setup is shown in Figure 4.1. The air bearing spindle has an axial motional error of less than 50 nm. A single crystal GaAs wafer (diameter of 50 mm, thickness of 5 mm) was glued on a copper fixture which was mounted on the vacuum chuck. The cutting direction was along the [1 1 0] direction on the (0 0 1) surface. A cubic lattice structure diamond turning tool with a rake angle of -25 degrees and a clearance angle of 10 degrees which is consistent with the tool geometry used in MD simulation was selected to conduct diamond turning trial. The depth of cut and cutting speed were set as 0.3 μm and 1.84 m/s, respectively. The values of depth of cut and cutting speed are selected based on preliminary experiments. The detailed experimental parameters are shown in Table 4.1. The cutting force was measured by a dynamometer (Kistler 9129). Finally, the machined GaAs workpiece surface was measured by a white light interferometer (Zygo CP300) after ultrasonic cleaning in a 95 % vol medical alcohol bath. The machining trials were performed on the (0 0 1) surface of the GaAs wafer under a dry cutting condition and at a room temperature of 20 degrees in accordance with the MD simulation setup.

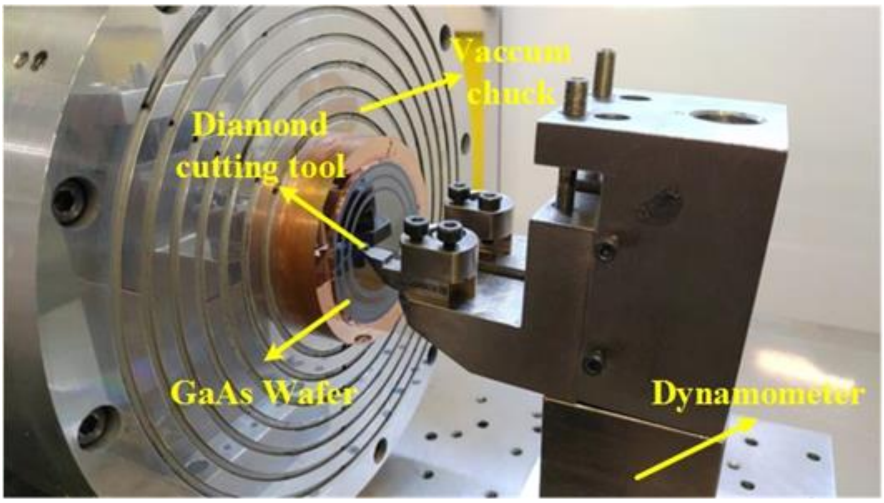

Figure 4.1 Experimental setup of single point diamond turning on GaAs workpiece.

Table 4.1 Diamond turning parameters.

Parameters	**Unit**	**Values**
Depth of cut	µm	0.3
Cutting speed	m/s	1.84
Feed rate	µm/rev	0.5
Tool nose radius	mm	5
Cutting edge radius	nm	61.14
Tool cutting edge radius	nm	73.79
Tool rake angle	degree	-25
Tool clearance angle	degree	10

4.3 MD simulation results during single point diamond turning

4.3.1 Simulation of cutting forces

Figure 4.2 (a) shows the variation of the cutting forces in the X and Y directions during the cutting process. The tangential cutting force F_x rose steeply in the first 2 nm of cutting and then fluctuated around 90 nN at the following 14 nm of cutting with a peak force of 109.373 nN. The normal force F_y increased dramatically in the first 7 nm of cutting and also slightly fluctuated at approximately at 130 nN with a maximum value of 149.33 nN. These data indicate that the cutting chip was generated at the initial 7 nm of cutting and then stabilized in the following 9 nm of cutting. In addition, as shown in Figure 4.2 (a), the growth rate of the normal force along the Y direction is less than the tangential force along the X direction during the chip formation stage but it then became larger than that of the tangential force. This phenomenon is attributed to the use of a diamond cutting tool with a large negative rake angle which provides the normal cutting force larger than the tangential cutting force. Additionally, the average coefficient of friction (Fx/Fy) was calculated to be 0.719 during the stable machining stage from the cutting distances of 10 nm to 16 nm and its variation is shown in Figure 4.2 (b).

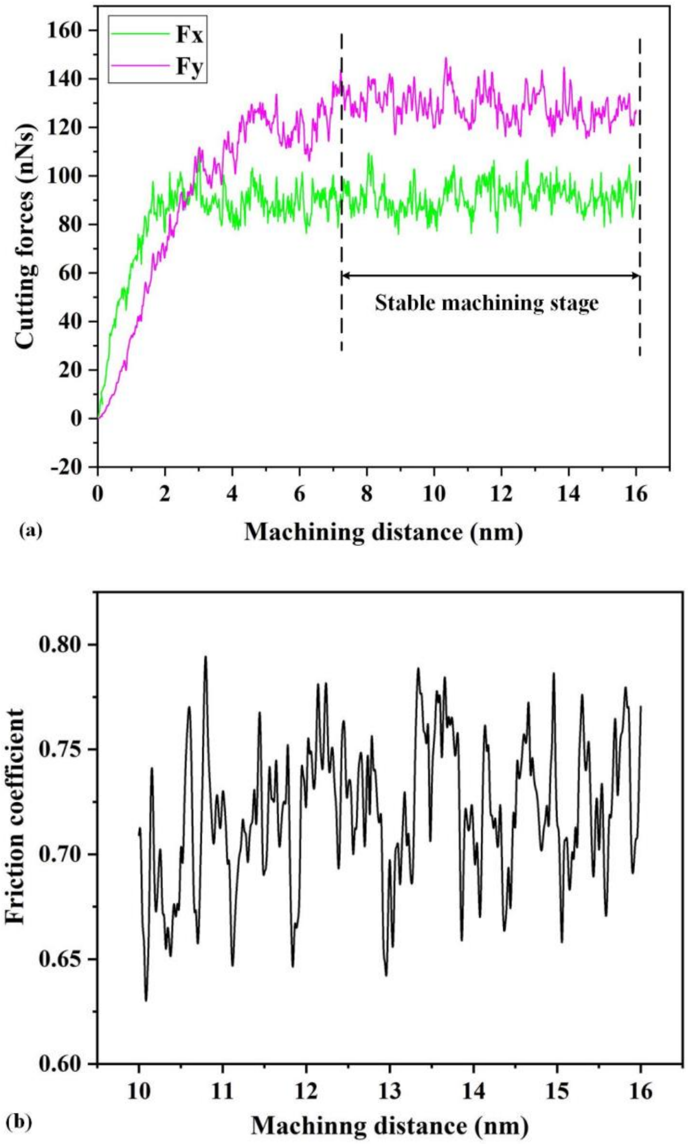

Figure 4.2 (a) variation of the cutting forces in the X and Y directions against cutting distances in MD simulations. (b) the variation of coefficient of friction during stable machining stage in MD simulations.

4.3.2 Simulation of cutting temperature

Rise of cutting temperature can cause thermal deformation or damage of workpiece therefore, cutting temperature is a significant influential factor on the machined surface form accuracy and integrity. In this study, the cutting temperature is calculated by using the following equation.

$$T = \frac{2K.E.}{3NK_b} \tag{4-1}$$

Where the $K.E.$ refers to the kinetic energy of GaAs substrate atoms, N is the atoms quantity, K_b represents the Boltzamn constant. The temperature was averaged over a cubic zone with a length of 10Å. A defined elemental atomic volume (16 × 2 × 3 nm^3) was set to the primary cutting zone. A dramatic rise of cutting temperature with the increase of cutting distance was observed in the diagram of the variation of cutting temperature shown in Figure 4.3 (b). The cutting temperature reached the maximum value of 851.86 K after the cutting distance of 15 nm. Figure 4.3 (a) illustrates the temperature distribution using various color zones. Same phenomenon has been observed on other ductile and brittle materials such as the Cu, Al, and Si materials [40][41]. According to temperature distribution, the highest temperature appeared at the top of chip, which is up to 1100K. This is because that the top of chip experienced the most serious lattice deformation which could possess the maximum transformation lattice energy. Furthermore, the diamond tool rake face and flank face also showed extremely high temperature nearly 900K and 700K, respectively, since the rake face pressed against the GaAs atoms and friction occurred between the flank face and the machined GaAs surface. Additionally, the subsurface of the machined GaAs at 2 nm underneath the flank face showed a high temperature of approximately 700K. Finally, most of the atoms beside to the substrate edge could keep an almost stable temperature 300K, which benefited from the heat dissipation of the thermostat layer atoms.

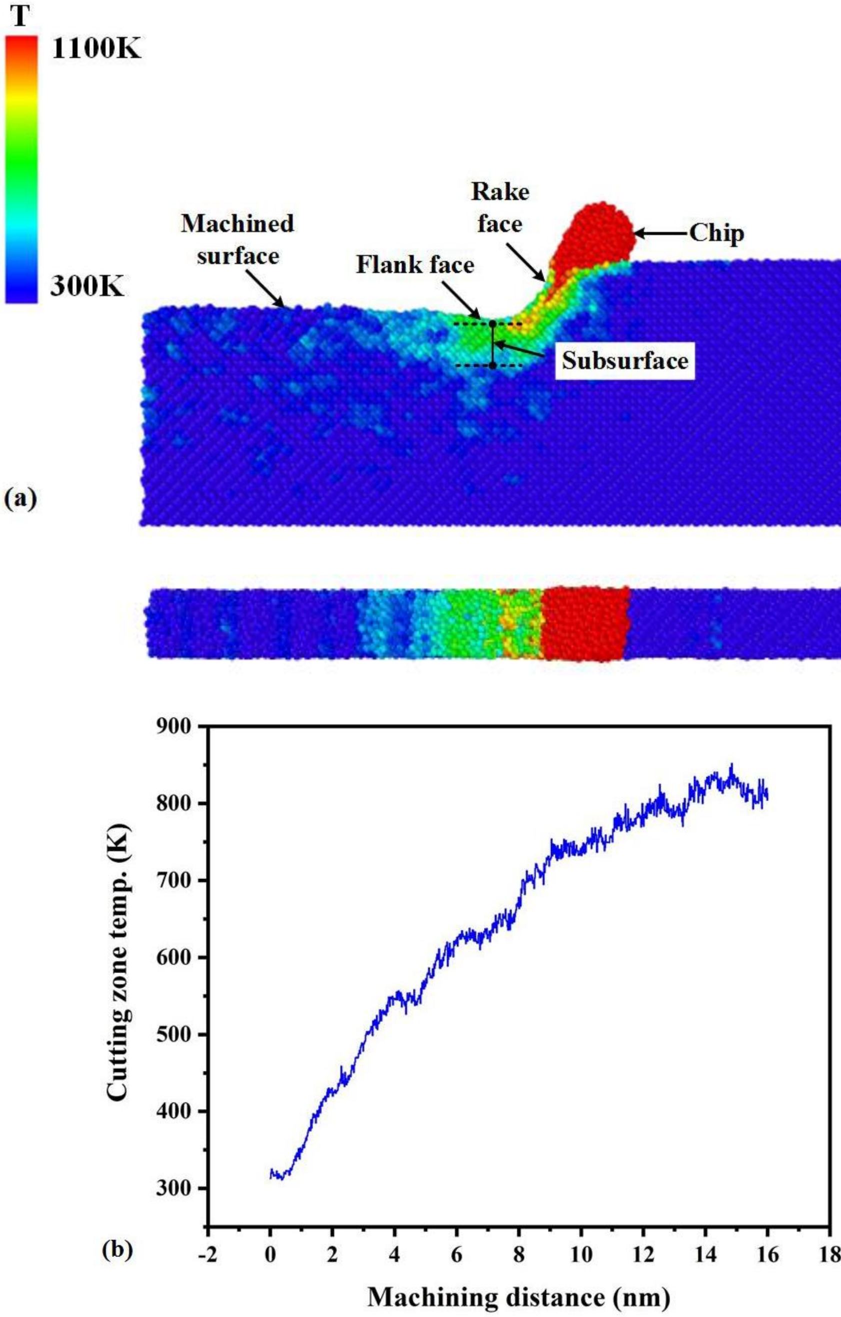

Figure 4.3 (a) temperature distribution on the GaAs workpiece after 16nm of cut. (b) increase of temperature during SPDT machining.

4.3.3 *Simulation of the influence of crystalline orientation*

The chapter also analyzed the effect of crystalline orientation on the cutting chip, sidewall morphology and coefficient of friction among typical crystal orientations, including the (0 0 1) surface along the [1 1 0] cutting direction, (1 1 0) surface along the [0 0 1] cutting direction, and (1 1 1) surface along the [1 $\bar{1}$ 0] cutting direction. According to Figure 4.4 and Figure 4.5, it is clear to see the GaAs atoms piled up on both sides of nanogroove when cutting the (0 0 1) and (1 1 1) surfaces. Furthermore, when cutting the (1 1 1) surface the GaAs atoms were evenly-distributed on both sides, while for cutting the (0 0 1) surface more atoms were piled up on one side, compared to the other. Almost all the removed atoms were piled up on one side for machining (1 1 0) surface. This occurrence might be attributed to different atomic density and inter-atomic distance in different GaAs crystal surfaces.

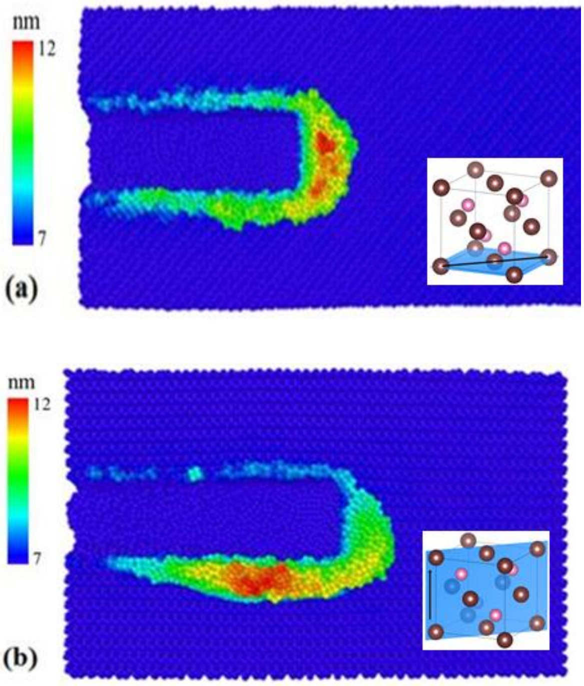

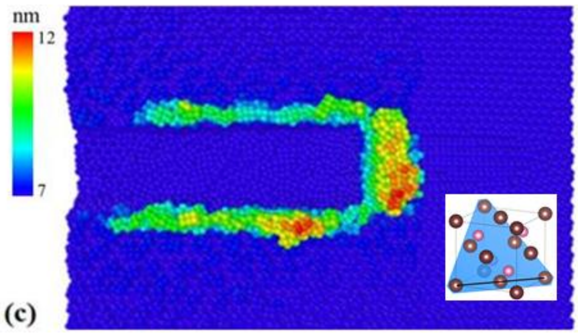

Figure 4.4 The colored morphology of cutting chip and sidewall pile-up during along the Y direction (a) GaAs (0 0 1) (b) GaAs (1 1 0) (c) GaAs (1 1 1).

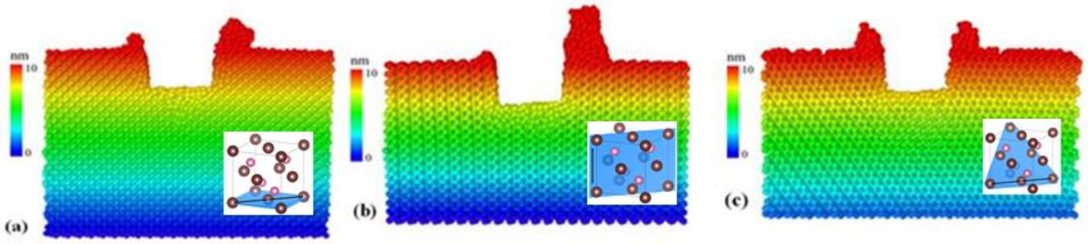

Figure 4.5 The pile-up of the sidewall during SPDT along the Y direction (a) GaAs (0 0 1) (b) GaAs (1 1 0) (c) GaAs (1 1 1).

Additionally, the cutting forces and coefficient of friction were calculated for three different kinds of crystal surfaces. The results were shown in Table 4.2. The minimum coefficient of friction of 0.630 was found when cutting the (1 1 1) face along the $[1\ \bar{1}\ 0]$ direction, which means the SPDT process has the least resistance in this crystalline orientation and cutting direction combination. The maximum coefficient of friction of 0.719 was found when cutting the GaAs (0 0 1) surface along the [1 1 0] direction. Cutting the (1 1 0) surface along the [0 0 1] direction shows the intermediate coefficient of friction of 0.680. The results suggested that the [1 1 0] direction is the hardest machining direction on (0 0 1) surface. This finding is consistent with the conclusion drawn in the experimental study on circumferential distribution of material brittle fracture index of single crystal GaAs by Chen et al [7].

Table 4.2 The average value of tangential force, normal force, and coefficient of friction during SPDT on different crystalline orientations.

	Fx (nN)	**Fy (nN)**	**COF**
(0 0 1)	91.6	127.4	0.719
(1 1 0)	82.3	121.0	0.680
(1 1 1)	66.4	105.3	0.630

4.4 Experimental results and comparison with MD simulations

The cutting force is a pivotal parameter for the study of SPDT process as it is directly related to the formation of cutting chip. The SPDT of GaAs workpiece experiments were carried out under 0.5 μm/rev feed rate. Firstly, the normal force was extracted, as indicated in Figure 4.6 (a). It suggests that the normal force of the machining tool experiences a rapidly increase in the first 20 s and keeps steady fluctuation after 40 s, which suggests the achievement of a stable chip. Consequently, it is obvious to see that the variation trend of experimental normal force in Figure 4.6 (a) is consistent with that of MD normal force simulation in Figure 4.2 (a). Secondly, the coefficient of friction calculated from the SPDT experiment under the feed rate of 0.5 μm/rev fluctuated around 0.70 during the stable machining stage from 40 s to 160 s, as shown in Figure 4.6 (b). In terms of quantitative coefficient of friction, the coefficient of friction obtained from SPDT experiment was 0.720 which is almost same as the MD simulation result of 0.719. Hence, the MD simulation results were verified well. In theory if the GaAs material showed ductile response on the difficult to cut surface and cutting direction, brittle fracture-free machined surfaces could therefore be achieved in other crystal orientations and cutting direction under the same machining parameters. In this study we selected the most difficult to machine (0 0 1) surface to carry out SPDT experiments along the most difficult to machine cutting direction [1 1 0]. The experimental result showed a nano-smooth machined GaAs surface finish with a surface roughness Ra of 8 nm could be obtained when using a feed rate of 0.5 µm/rev and a spindle speed of 800 rpm and a depth of cut 0.3 µm, which is shown in Figure 4.7.

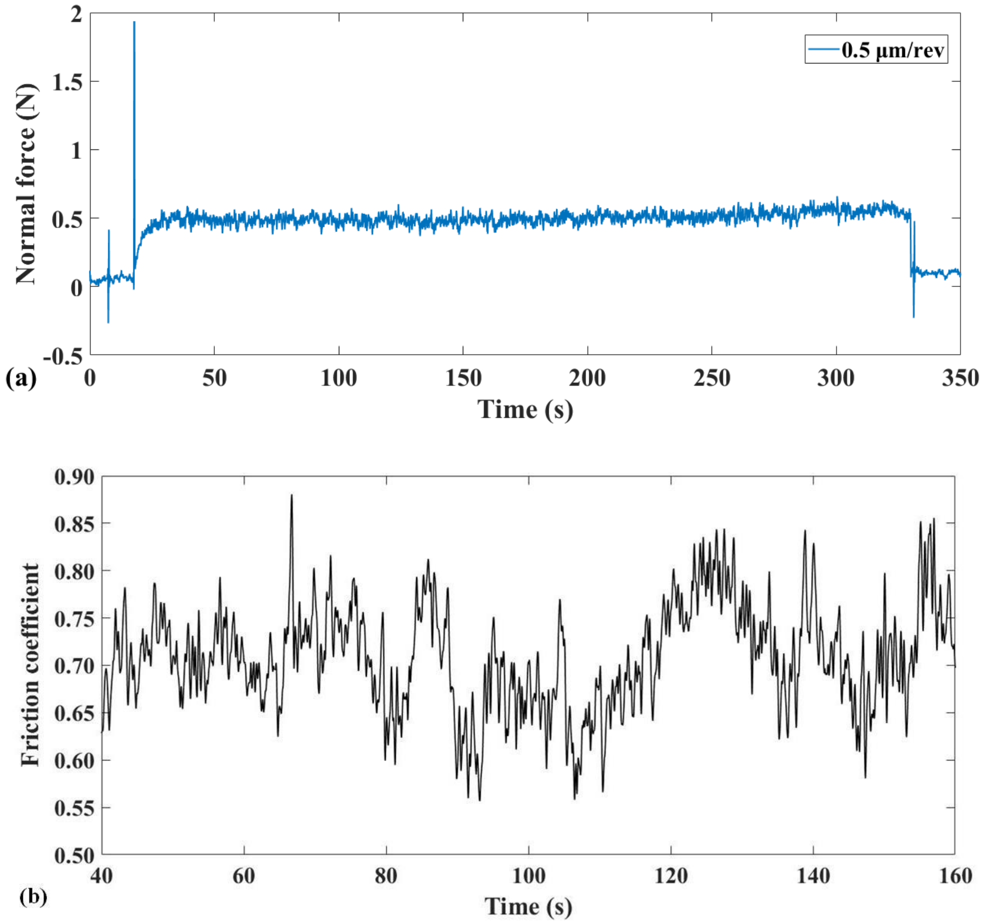

Figure 4.6 (a) variations of normal force F_y at the feed rates of 0.5 µm/rev in experimental test. (b) the variation of coefficient of friction of SPDT experiments results under 0.5 µm/rev in experimental tests.

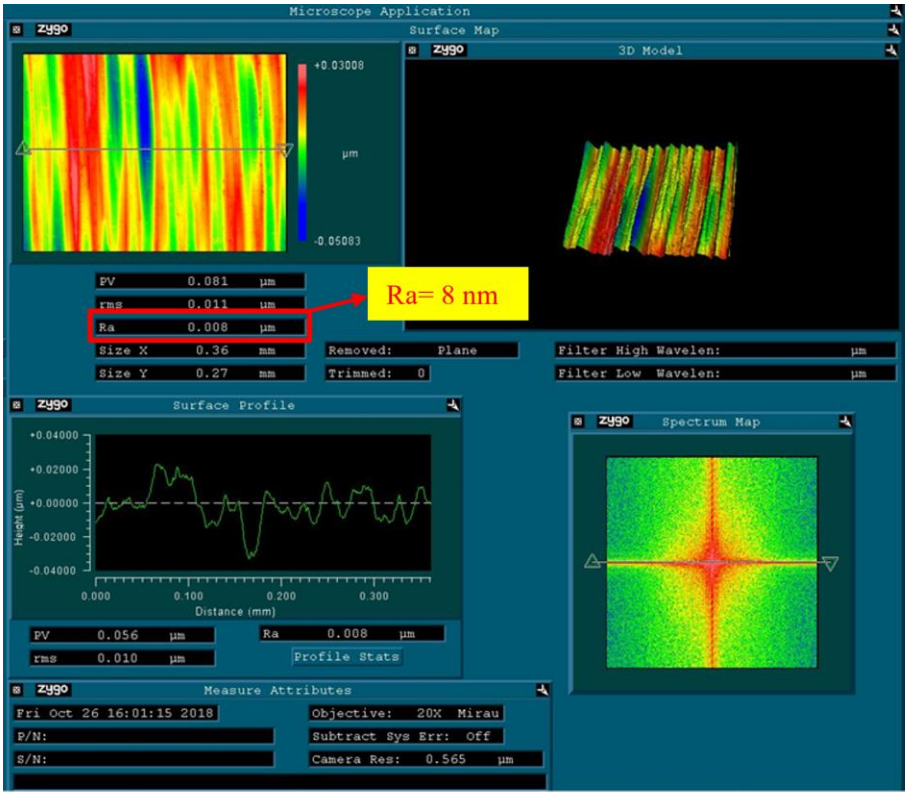

PV 0.081 µm
rms 0.011 µm
Ra 0.008 µm
Size X 0.36 mm
Size Y 0.27 mm
Removed: Plane
Trimmed: 0
Filter High Wavelen: µm
Filter Low Wavelen: µm

PV 0.056 µm
rms 0.010 µm
Ra 0.008 µm

Fri Oct 26 16:01:15 2018
P/N:
S/N:
Objective: 20X Mirau
Subtract Sys Err: Off
Camera Res: 0.565 µm

Figure 4.7 Measured machined surface of GaAs in SPDT experiment.

4.5 Summary

In this chapter, both MD simulation technique and SPDT method have been employed to investigate cutting forces, temperature distribution in the cutting zone and influence of crystalline orientation during nanometric cutting of single crystal GaAs. In terms of qualitative verification, the variation of cutting forces of MD simulation is consistent with that of SPDT experiments result. In terms of quantitative verification, the coefficient of friction of MD simulation is in line with the result of SPDT experiments, around at 0.72. Additionally, the MD simulation results show the SPDT is accompanied by a sharp rise in temperature in the cutting zone. The generated highest temperature is located at the cutting chip, in which the temperature can reach up to 1100K. Furthermore, the rake face and flank face also have extremely high temperatures nearly 900K and 700K, respectively. Finally, single crystal GaAs shows the strong anisotropic machinability during SPDT. When the cutting direction is along the [1 1 0] direction on the (1 0 0) surface, surface topography demonstrates more atomic level pile-up on one side, compared to the other. When the cutting direction is along the [0 0 1] direction on the (1 1 0) surface, most atoms flow to one side. When the cutting direction is along the [-1 -1 0] direction on the (1 1 1) surface, the removal atoms are well-distributed on both sides.

Chapter 5 Nanomachining of Polycrystalline GaAs

5.1 Introduction

GaAs can be grown as a single crystal using methods such as the vertical gradient freeze method, the Bridgman-Stockbarger technique, or the Liquid encapsulated Czochralski growth process [199][200]. Parallel to this, the films of polycrystalline GaAs can be grown by chemical vapour deposition (by annealing an amorphously grown film) [201], or by using molecular beam epitaxy (MBE) [202]. Remarkably, it was found that single crystal GaAs is widely applied in the wireless communication aiming to offer the data communication between base station and users [203]. However, the polycrystalline GaAs is intensively employed in fiber optic communication aiming to complete centralized transmission of a large number of user's data [204]. As opposed to the single crystal GaAs, solar cells of polycrystalline GaAs thin film based can much better reach the demand in the high efficiency (20% AM1.5 with average grain sizes < 1 mm^2) [205], thin [206], light [207] and flexibility [208]. In the field of imaging detectors [209], microwave [210] and optoelectronic devices [211], polycrystalline GaAs gains even wider application due to its low processing cost than that of single crystal GaAs. For the polycrystalline GaAs based nanoscale devices in above applications, multiplex 2D or 3D free-form nanostructures are often required. Subsequently, the investigation of ductile plasticity mechanism become significant for nanomachining polycrystalline GaAs. The deformation mechanisms of polycrystal material which dominated by grain boundaries and dislocations are widely studied and reported in many previous studies [212][213][214]. However, the mechanism was studied by concentrating on the nucleation of dislocations inside of the grains. The origin of incipient dislocations site and fundamental reasons of ductile plasticity in a polycrystalline GaAs during scratching is unknown. Therefore, this chapter reveals the origin of ductile plasticity in a polycrystalline GaAs by establishing extreme scratching conditions spanning from a depth of cut varying from 0 nm to 2 nm via MD simulation technique. Also, this chapter will discuss the scratch forces, sub-surface damage, peak cutting temperature, cutting stresses in a polycrystalline substrate benchmarked against a single crystal GaAs substrate. This chapter only conducted MD simulations for SPDT and not for AFM tip-based nanomachining. Additionally, no experimental result will be reported in this chapter.

5.2 Microstructural changes of polycrystalline GaAs during SPDT

Taking a test case of a depth of cut of 2 nm and a scratch velocity of 200 m/s, Figure 5.1 shows a simulation output wherein blue color atoms, white color atoms, green color atoms and red color atoms represent the perfect zinc blende (ZB) structure, amorphous (Amp) structure, hexagonal diamond (HD) structure and stacking faults (SF) respectively.

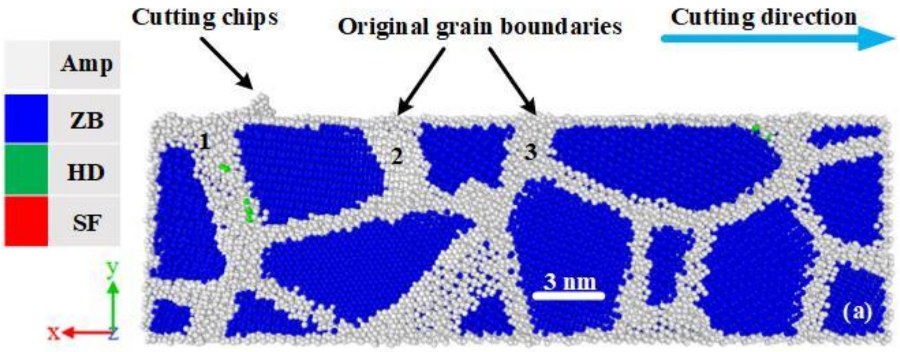

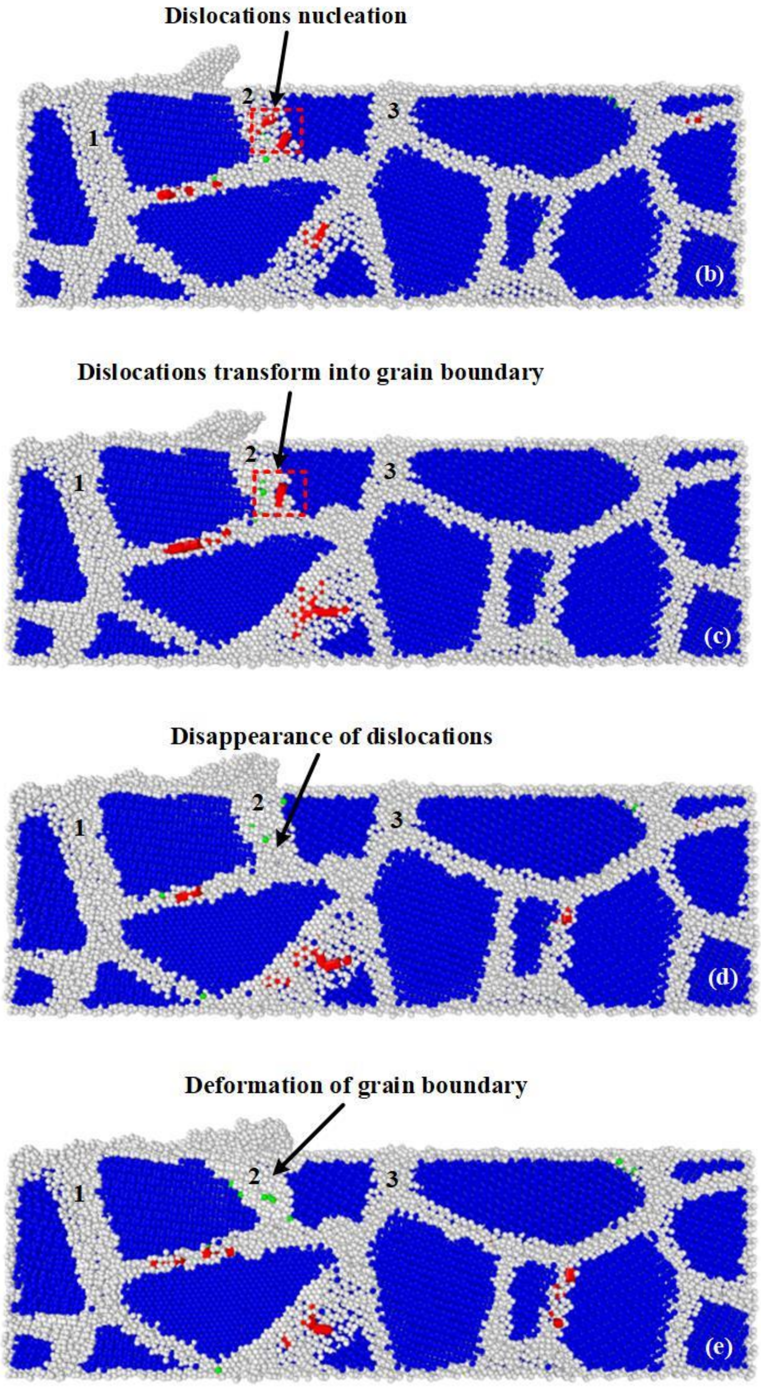
Dislocations nucleation
2
1
3
(b)
Dislocations transform into grain boundary
2
1
3
(c)
Disappearance of dislocations
2
1
3
(d)
Deformation of grain boundary
2
1
3
(e)

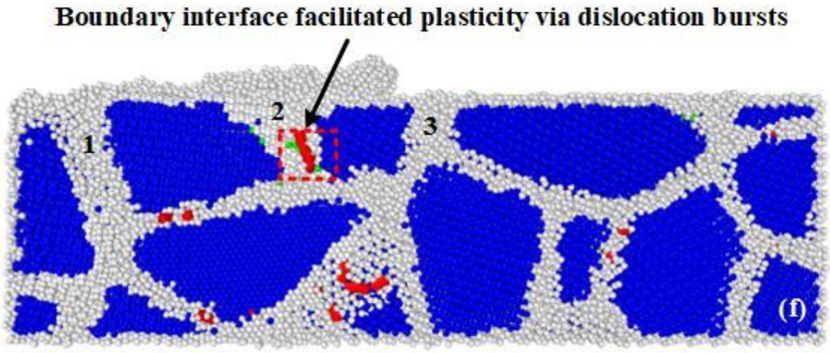

Figure 5.1 Cross-sectional image of the polycrystalline GaAs (diamond tool is kept hidden for visualization and cutting is performed at a depth of 2 nm and scratch velocity of 200 m/s). The snapshots are taken at cutting distances (a) 3 nm, (b) 6 nm, (c) 7 nm, (d) 8 nm, (e) 9 nm and (f) 12 nm. Pictures were processed using OVITO.

As shown in Figure 5.1 (a), the grain boundaries marked by 1, 2 and 3 were chosen as the sites of analysis for post-processing visualization of the dislocation and stacking fault structures using the second nearest neighbor scheme relying on an extended common neighbor analysis implemented in OVITO [215]. Figure 5.1 (b) highlights the initiation of the nucleation of dislocations at several places in the grain boundary 2 (GB 2). With subsequent tool travel, i.e. at the cutting distance of 7 nm, a part of the dislocations created at a cutting distance of 6 nm started to transform to grey color atoms and became a part of GB 2, as illustrated in Figure 5.1 (c). Subsequently, the dislocations within GB 2 disappeared and transformed into a grain boundary marked by grey color atoms at the cutting distance of 8 nm shown in Figure 5.1 (d). Meanwhile, a small number of green atoms were found present in the grain boundaries. At the cutting distance of 8 nm, the GB 2 widens and became thicker as may be seen in Figure 5.1 (e). Finally, as shown in Figure 5.1 (f), a large dislocation burst appeared in the GB 2 at the cutting distance of 12 nm, and a few grey color atoms transformed into red color atoms. The observation reported here remains consistent in all the simulation test cases.

Meanwhile, the evolution of structural changes in polycrystalline GaAs was quantified as a function of cutting velocity at various depths of scratch (see Figure 5.2). It must be noted here that the BOP potential function used in this study does not predict the energy differences between the cubic diamond and hexagonal closed packed diamond and hence the observation of hexagonal diamond in this study is a mere reflection on the faulted diamond cubic structure [216]. Overall, results in Figure 5.2 show that a higher cutting velocity leads to a reduced degree of structural transformation in the material. Additionally, it was observed that all such microstructural transformations initiate preferentially in the grain boundaries. It implies that grain boundaries are preferred sites of nucleation of dislocations during the scratching of a polycrystalline substrate.

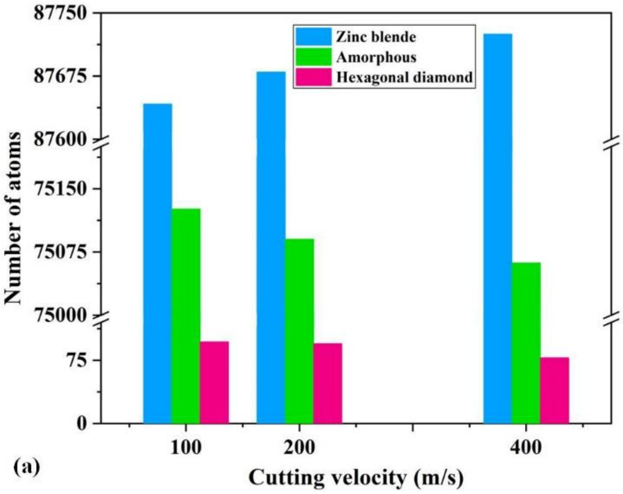

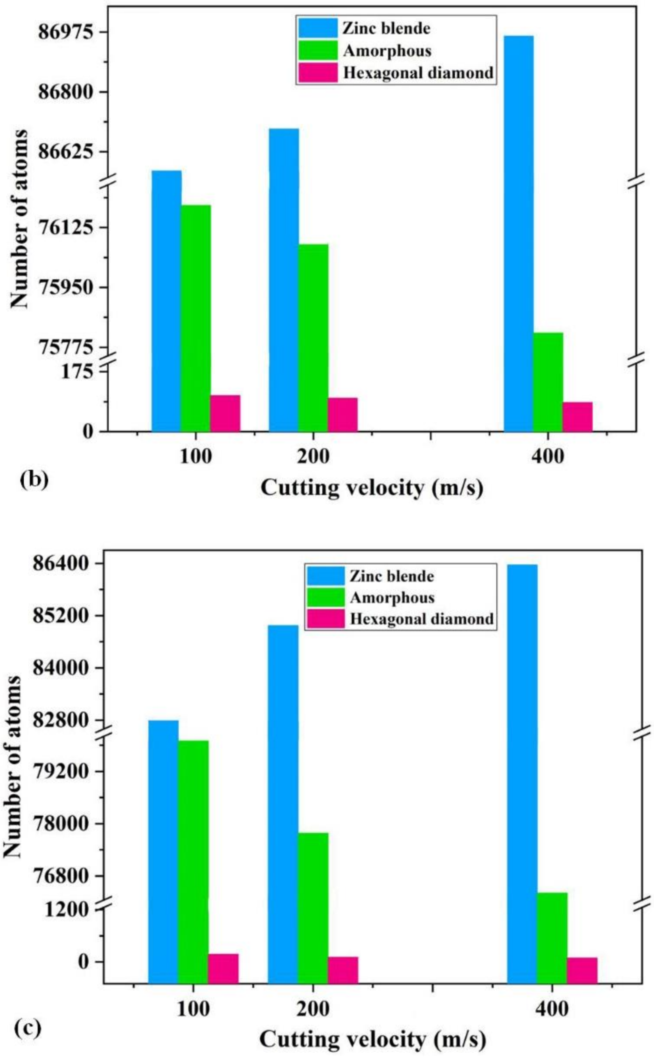

Figure 5.2 The evolution of microstructure changes in polycrystalline GaAs during nanoscratching process with various cutting velocities under depth of cut of 0.5 nm (a), 1 nm (b) and 2 nm (c). Note here that the occurrence of the formation of hexagonal diamond is a mere artefact since the potential function used in this study does not distinguish energy differences between cubic and hexagonal phases.

5.3 Analysis of nucleation of dislocation

Figure 5.3 shows the details of nucleation of dislocation. It can be seen that the nucleation of dislocations (marked by red color atoms) occurred in the grain boundaries, which is consistent with the two-dimensional (2D) images shown earlier in Figure 5.1. As no dislocations were found inside of the individual grains of polycrystalline GaAs, it indicated that the grain boundaries are softer than the grains and deform swiftly. This phenomenon is in accordance with the recently reported work on polycrystalline silicon carbide material [195]. Additionally, when the diamond tool penetrated the polycrystalline GaAs at 3 nm (see Figure 5.3 (a)), the two clusters of the dislocations were found in G1-G2 and G5-G6, respectively. Subsequently, the dislocation nucleation diffused through G4-G5 and the right corner of the polycrystalline GaAs workpiece, as illustrated in Figure 5.3 (b). In accordance with Figure 5.3 (c) and Figure 5.3 (d), the dislocation nucleation kept reappearing when the diamond tool passed through the edge of the grain boundary between G4 and G5. When the diamond tool started to penetrate the grain boundary between G4 and G5, there was no dislocation nucleation in G4-G5 (see Figure 5.3 (e)). The dislocation nucleation was distributed across the G5-G6 and G7-G8-G9-G10-G11-G13. Finally, the dislocation nucleation reoccurred in the G4-G5, as showed in Figure 5.3 (f), while the diamond tool cuts the grain boundary between G4 and G5.

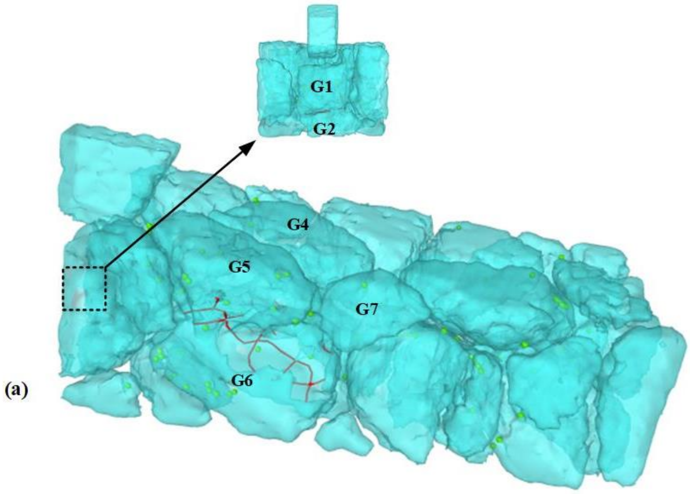

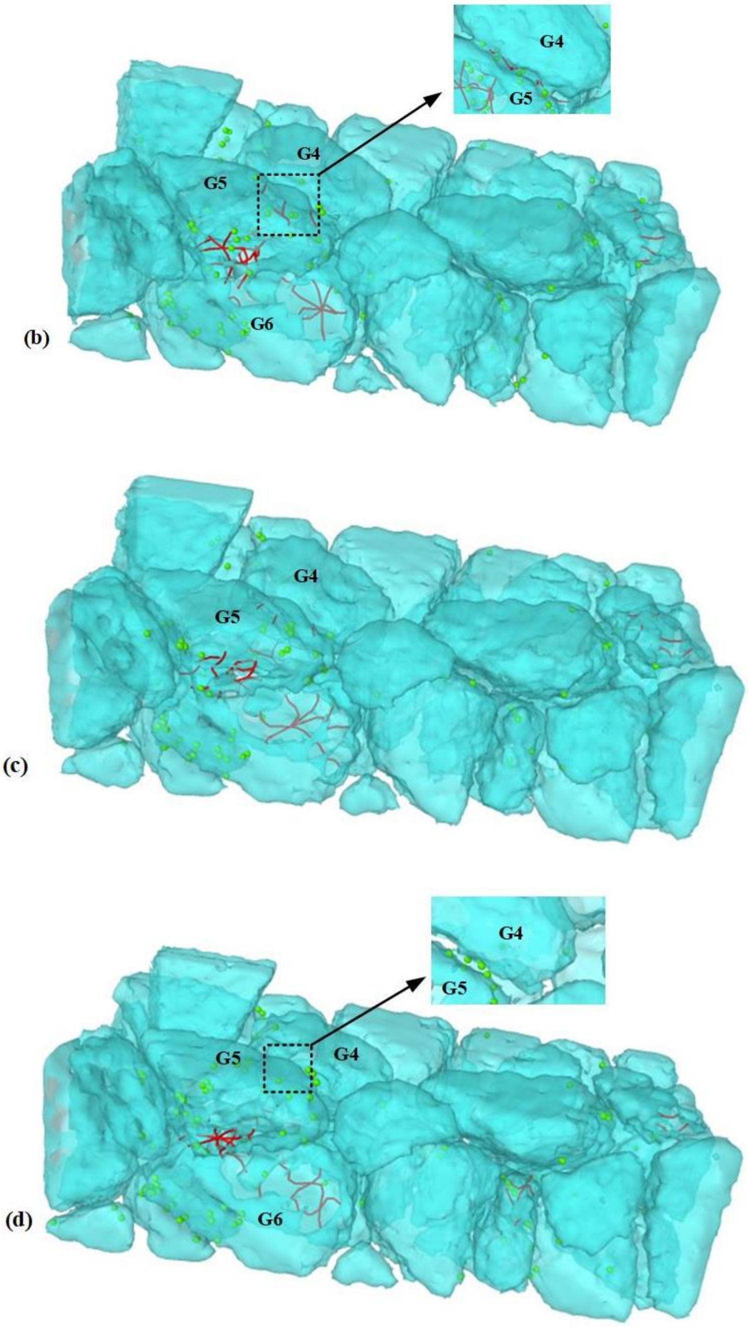
G4
G5
G4
G5
G6
(b)
G4
G5
(c)
G4
G5
G5
G4
G6
(d)

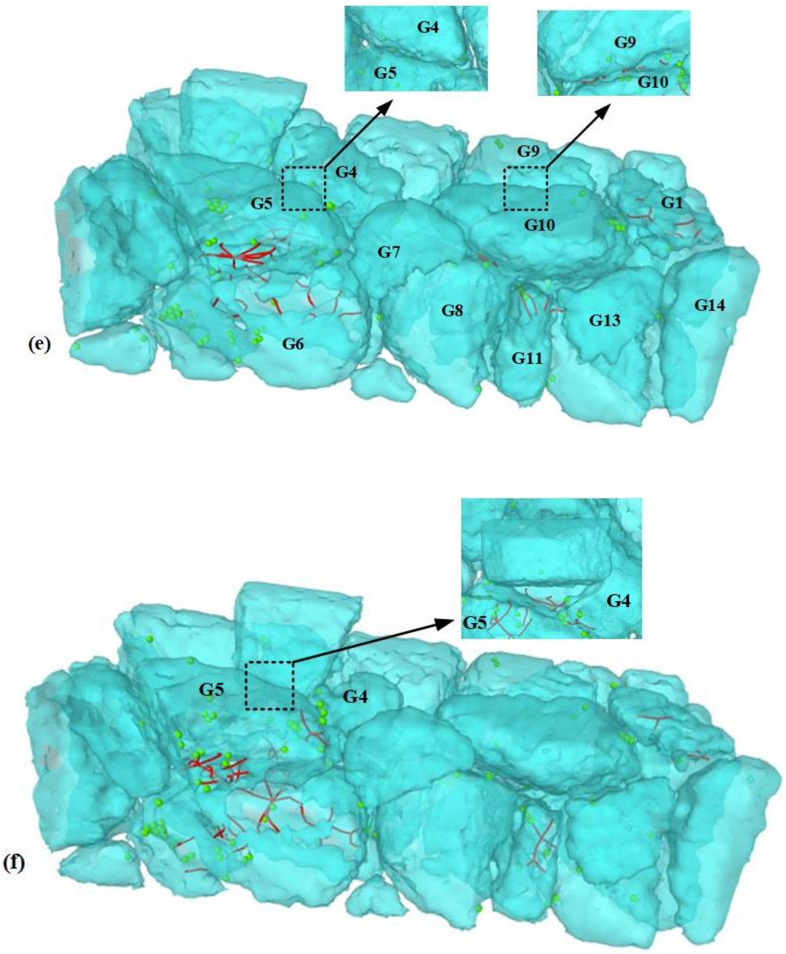

Figure 5.3 The movement of dislocations in the polycrystalline GaAs at (a) 3 nm (b), 6 nm (c), 7 nm (d), 8 nm (e), 9 nm and (f) 12 nm.

In terms of the quantitative analysis, the number of dislocation segments extracted from the MD data is shown in Figure 5.4. It can be seen that the presence of 1/2<110> type dislocations dominated others which was responsible for the incipient plasticity observed in the polycrystalline GaAs. The two other dislocations of type $1/6\langle 112\rangle$ and $1/3\langle 111\rangle$ were also present and were of the same length for the duration of cutting studied here. During the simulation, the dislocation with 1/2[110] Burgers vector was observed to split into two Shockley partials with one having

$1/6\,[121]$ Burgers vector and the other having $1/6\,[211]$ Burgers vector. The dissociation reaction can be represented as $1/2\,[110] = 1/6\,[121] + 1/6\,[211]$.

Also, the $1/3\langle 111\rangle$ dislocation with [-110] Burgers vector at 7 nm cutting distance appears to dissociate to a $1/3\langle 111\rangle$ dislocation with [11-2] Burgers vector. This phenomenon suggests the shuffle set dislocations could transit to glide set dislocations under large shear stress caused by the scratching tool [217]. The occurrence of the dual slip mechanisms was seen an important factor driving plasticity in poly GaAs in sharp contrast to a single GaAs.

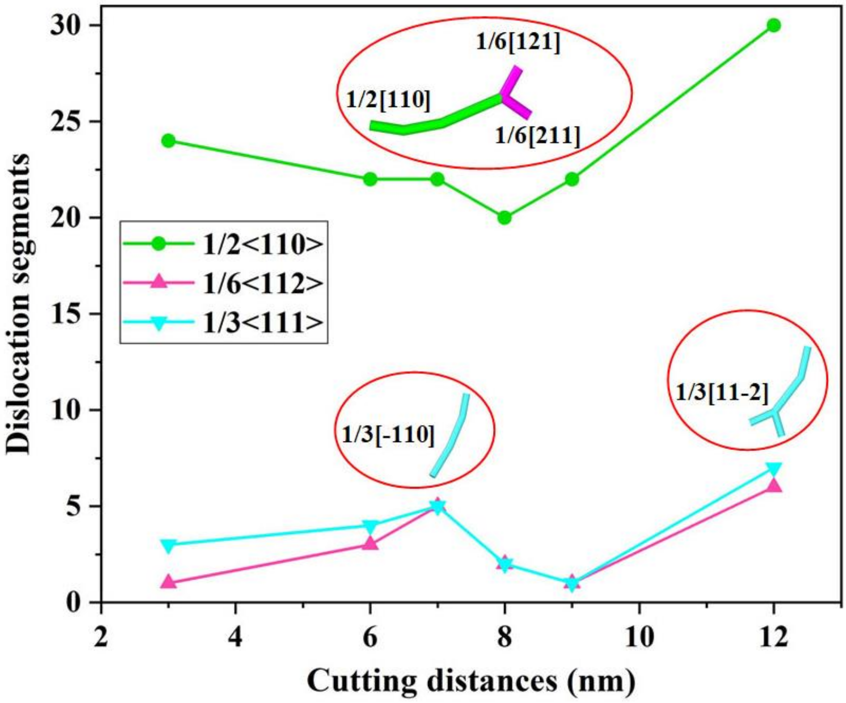

Figure 5.4 Variation in the extent of dislocation segments and dislocations images with cutting distance.

An important physical quantity, dislocation density, was employed to describe the total length of dislocation lines contained in a unit volume of polycrystalline GaAs. The dislocation density was calculated by follow equation [218].

$$\rho = \frac{L}{V} \tag{4-2}$$

Where the L and V represent the total length of dislocation lines (Å) and volume of workpiece ($Å^3$), respectively. Consequently, the evolution of dislocation density as a functional of scratching distance is illustrated in Figure 5.5.

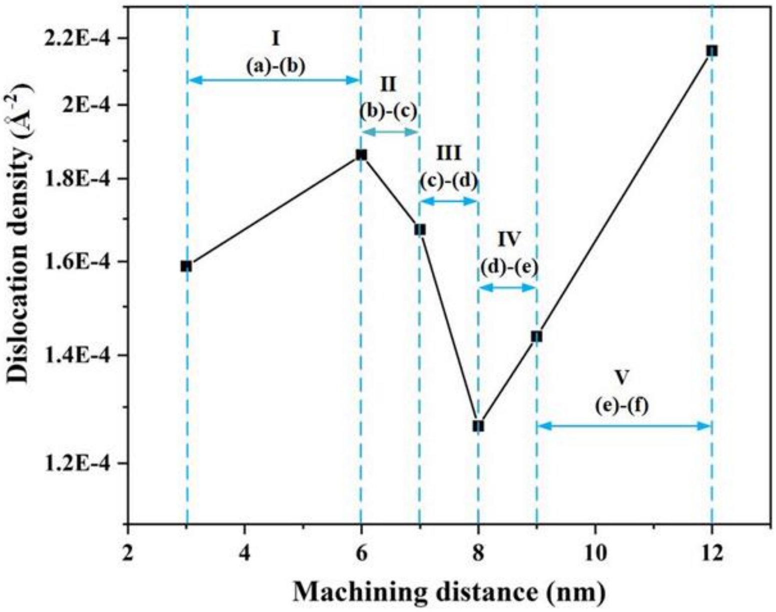

Figure 5.5 Evolution of the dislocation density as a function of machining distance.

The dislocation density curve was seen to consist of five stage (I, II, III, IV and V). The dislocation density in the Ist stage was seen to increase which indicated the initiation of dislocation nucleation within the grain boundary. The dislocation density in the IInd and IIIrd stage decreases implied that certain dislocations transform to grain boundaries vis-a-vis disappearing of certain dislocations in a certain grain boundary as shown in Figure 5.1 and Figure 5.3. The dislocation density of the IV and V stage experienced a significant increase indicating that the diamond tool propagated through the grain boundaries to cause more dislocations and the cycle keeps repeating.

5.4 Influence of depth of cut and cutting speed

In this section, the influence of depth of cut and cutting speed on the cutting forces, sub-surface damage depth and the cutting temperature are reported. As shown in Figure 5.6, both lateral (F_x) and normal forces (F_y) during cutting of the polycrystalline GaAs decreased with the increase of cutting speed or decreasing depth of cut. It was further observed that the normal force (F_y) continues to be higher than the lateral force (F_x) in all cases of scratching.

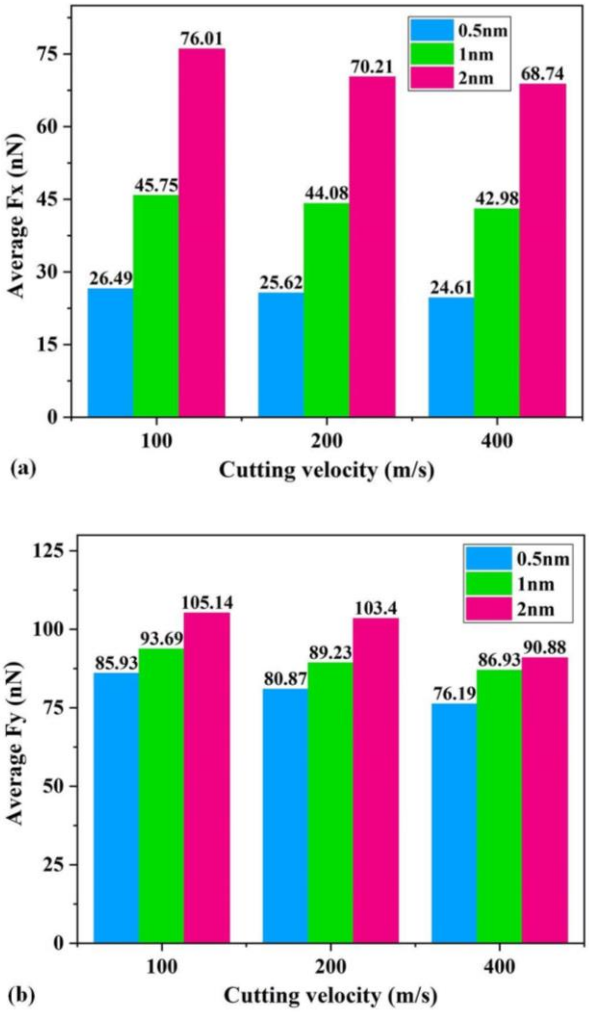

Figure 5.6 The average value of the lateral (F_x) and normal forces (F_y) under different cutting velocities and depth of cut in cutting of polycrystalline GaAs.

Next, the sub-surface damage depth during cutting of polycrystalline GaAs was estimated as a function of different speeds and depth of cut which is shown in Figure 5.7. It can be seen that the damage depth reduces with the increase of cutting speed which indicates that high strain rate applied during cutting decreases the sub-surface damage. A maximum sub-surface damage reduction of 16.32% could be achieved while cutting at 400 m/s at a depth of cut of 2 nm in comparison to cutting at 100 m/s at the same depth of cut.

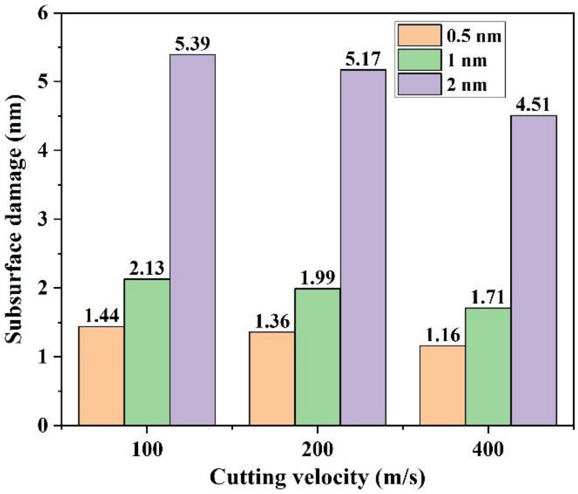

Figure 5.7 Sub-surface damage depth at different cutting velocities and depth of cut.

Finally, the variation of temperature as a function of depth of cut and cutting speed was estimated and shown in Figure 5.8. Higher speed of cutting and higher depths of cutting were both seen to accompany an increase in the cutting temperature in the plastic zone. The combined information of the temperature and stresses acting in the cutting zone could be used as a vital information to predict the microstructural changes in the cutting zone and we shall expand on this aspect in our future work.

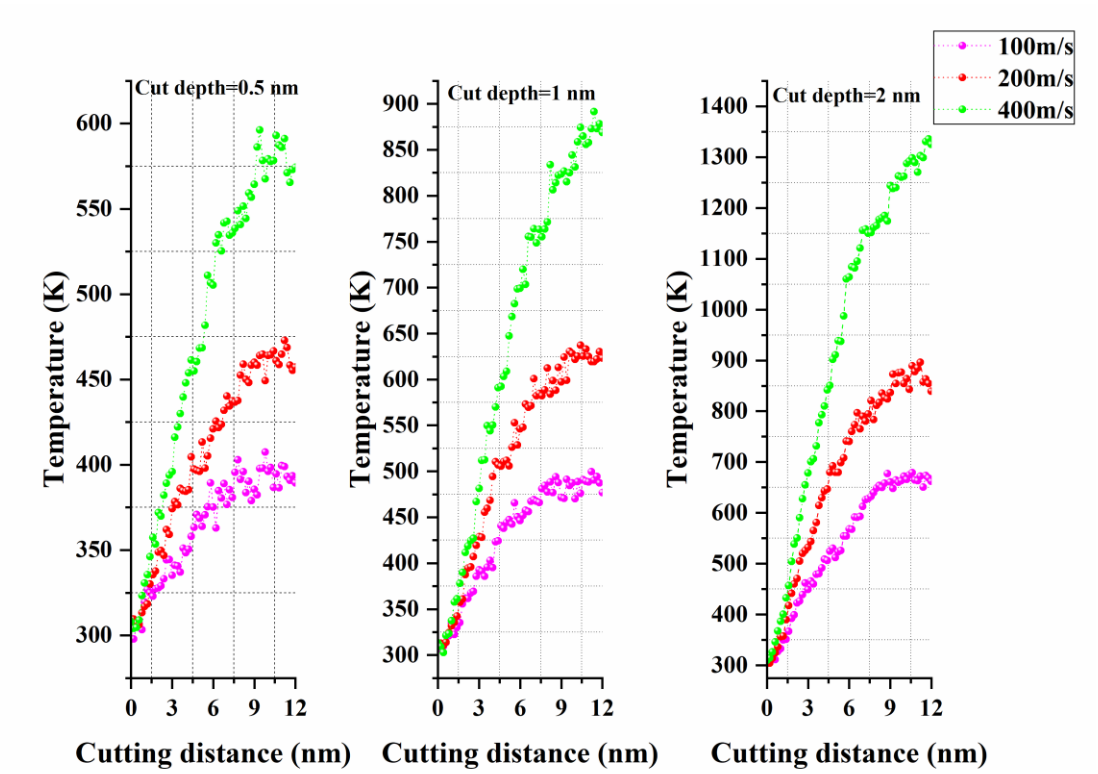

Figure 5.8 Peak temperature variation at various scratch speeds and depth of cuts.

5.5 Differences in the cutting of single crystal and polycrystalline GaAs

During this investigation, additional MD simulations were performed to benchmark the scratch forces namely, the lateral force (F_x) and normal force (F_y) during cutting of polycrystalline GaAs and single crystal GaAs. Figure 5.9 shows the evolution of the scratch forces obtained from the MD simulations while cutting polycrystalline GaAs and single crystal GaAs substrates. Initially, until the onset of chip formation (unsteady cutting condition), the lateral force (F_x) was seen to be larger than the normal force (F_y) and once the machining achieved a steady-state, then the normal force (F_y) becomes larger than the lateral force. In this study, under the same scratching condition (depth of cut of 2 nm and cutting velocity of 200 m/s), the lateral

(F_x) and normal force (F_y) while cutting polycrystalline GaAs were about 70 nN and 110 nN respectively while the forces during cutting of the single crystal GaAs were of the order of 90 nN and 130 nN, respectively. The variation trend of MD normal force simulation can be validated qualitatively to some extent by our recent experimental results reported in [7].

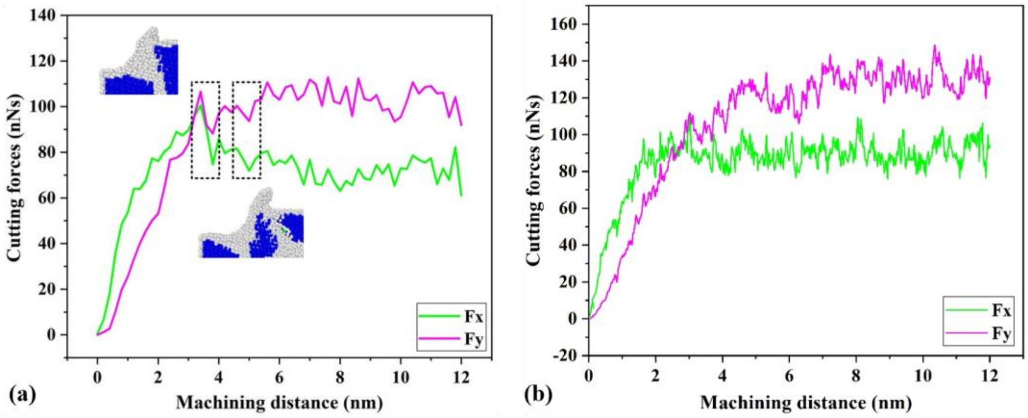

Figure 5.9 Evolution of cutting forces i.e. lateral (F_x) and normal force (F_y) at a cutting velocity of 200 m/s and at depth of cut of 2 nm (a) Scratch forces during cutting of a polycrystalline GaAs (b) Scratch forces during cutting of a single crystal GaAs.

Furthermore, by comparing Figure 5.9 (a) and Figure 5.9 (b), it can be seen that the lateral (F_x) and normal force (F_y) smoothly undulated from crests to troughs during cutting of polycrystalline GaAs. The reason for this is that the cutting force drops as the grains started to slide along an easy slip direction and when the grain boundary paved the way for the plastic deformation causing the cutting energy to be mainly concentrated in the grain boundaries. Beyond a certain threshold, the grain boundary collapses releasing a burst of deformation energy which leads to wave troughs of the cutting force. Additional calculations of the specific cutting energy (e_c) and coefficient of friction (F_x/F_y) were also made. The specific cutting energy is defined as the work done by the tool in removing the unit volume of material and it can be calculated as [219].

$$e_c = \frac{R}{b \times t} \tag{4-3}$$

Where R refers to the resultant force $sqrt(F_x^2 + F_y^2)$ while b and t represents the width of cut and depth of cut, respectively.

As shown in Table 5.1, the resultant cutting force, specific cutting energy and kinetic coefficient of friction values for cutting polycrystalline substrate were seen to be lower in magnitude compared to cutting single crystal GaAs.

Table 5.1 Comparison of cutting results for single crystal GaAs and polycrystalline GaAs.

Workpiece	F_x **(nN)**	F_y **(nN)**	F_r **(nN)**	**Specific cutting energy (GPa)**	**Coefficient of friction**
Single crystal GaAs	91.56	127.35	156.85	27.46	0.719
Polycrystalline GaAs	70.21	103.40	124.98	21.88	0.679

The machining force results indicated that the polycrystalline GaAs was more machinable than the single crystal GaAs. This is due to the presence of grain boundaries which eases the ductile deformation of a polycrystalline substrate.

5.6 Summary

In this chapter, the deformation mechanism of polycrystalline GaAs during nanoscratching was investigated by the MD simulations and benchmarked to single crystal GaAs. During the simulations, the scratch depth, speed of scratching (thus the applied strain rate) and microstructure of the workpiece (polycrystalline vs single crystal GaAs) were varied and output parameters such as the scratch forces (and specific cutting energy), kinetic coefficient of friction, cutting temperature, sub-surface damage and dislocation structures were extracted and analysed. The MD simulations results show that the grain boundaries of polycrystalline GaAs are the incipient sites of nucleation of 1/2<110> dislocation. The 1/2<110> type dislocation can dissociate into 1/6<121> and 1/6<211> type dislocations within the grain boundaries. The sub-surface damage decreases with the increase of cutting velocities and depth of cut. The cutting zone temperature increases with the increase of cutting velocities and depth of cut. It is discovered that the polycrystalline GaAs has smaller friction coefficient and specific cutting energy than their counterparts in scratching single crystal GaAs. The cutting forces demonstrates a unique cyclic wave crest to wave troughs transition comparing with the cutting of the single crystal GaAs. This is another interesting finding of this chapter.

Chapter 6 Atomic Scale Friction during Nanomachining of GaAs

6.1 Introduction

Obtaining the kinetic coefficient of friction is an important element in nanotribology as many analytical equations to obtain insights into the wear processes require the value of the coefficient of friction as a *priori*. However, the previously reported values of coefficient of friction except for the work of Komanduri et al. [220] have reported a wide range of values varying from extremely low ~0.005 to intermediate values of 0.13 to high values of 1.2 and 5. Moreover, they investigated nanoscale friction on aluminium which is a face centred cubic ductile metal and hence there is an element of doubt about whether the same conclusions will still apply to a zinc-blende lattice structure material like GaAs. From the literature, a survey of materials shows that a wide range of values for the coefficient of friction (COF) depending on the material's crystal structure – a list of these is shown in Table 6.1.

Table 6.1 Coefficient of friction (COF) in various materials.

Material	Lattice structure and lattice plane	Method and counter material	COF
Silicon Carbide [221]	Zinc blende (001)	Nanoscratching with diamond	0.70
	Zinc blende (110)		0.64
	Zinc blende (111)		0.66
Titanium [222]	Body centred cubic (001)	Nanoscratching with silicon nitride	0.76
Tantalum [223]	Body centred cubic (001)	Nanoscratching with diamond	0.68
Nickel [224]	Face centred cubic (100)	Nanoscratching with nickel	0.60
Copper [225]	Face centred cubic (110)	Nanoscratching with copper	0.27
	Face centred cubic (100)		0.46
PMMA [226]	—	Nanoscratching with steel ball	0.50
Glass [227]	Amorphous solid	Nanoscratching with diamond	0.12
Graphene [153]	Hexagonal	Nanoscratching with diamond	0.22

A similar investigation on a brittle-hard semiconductor material like GaAs is necessary to ensure whether the nature of atomic-scale friction in this material is similar or different to that of the materials listed in Table 5.1. Particularly, an open-ended question is whether GaAs behaves similarly to aluminum in terms of nanoscale scratching size effect and whether the force ratio and specific scratching energy in GaAs scale with the scratching depth or remain unchanged? These questions were the primary motivation behind undertaking this chapter. According to the literature review, many MD studies have emerged during the last decade and further studies are emerging about the nanomachining of GaAs. These studies have shed light on aspects of crack formation [228] during single point diamond turning (SPDT), plastic deformation of the GaAs [229] and material removal mechanism during its chemo-mechanical polishing [230]. These studies however have not addressed aspects of size-effect observed in GaAs much like the other brittle materials and have also not clarified whether the kinetic coefficient of friction is a robust enough indicator to compare simulations and experiments especially in this era of the digital twin. Consequently, a well-planned experimental and molecular dynamics simulation methodology was developed by undertaking a thorough investigation to obtain various insights relevant to the cost-effective nanomanufacturing of GaAs in this chapter.

6.2 AFM tip-based nanoscratching experimental setup

The nanoscratching experiments were performed on the (110)-oriented GaAs surface using a triangular pyramid diamond tip (Micro Star Technologies Ltd. (US)) on a commercial AFM platform with a Nanoman module (Dimension Icon, Bruker Corporation, Germany). The nanoscratching feed direction was kept perpendicular to the cantilever of the diamond tip to avoid its bending due to the scratching load [231]. A schematic illustration of the nanoscratching methodology followed during the experiments is shown in Figure 6.1. The diamond tip was maneuvered into the workpiece at a velocity of 5 μm/s for each scratch under 0.05 V ~ 0.4 V applied voltage. The preset normal load (F_N) from this information can be estimated as F_N=Voltage×$\mathrm{K_N}$×sensitivity where the K_N refers to the spring constant of the cantilever of the diamond tip, which was 200 N/m specified by the manufacturer. The sensitivity was measured to be 627.5 nm/V by pressing the diamond tip on a sapphire specimen surface. Therefore, the normal load (F_N) was estimated to be in the range of 6.28 μN to 50.20 μN for the applied voltage of 0.05 V to 0.4 V, respectively. The normal load was set small enough to ensure that the material removal during the nanoscratching occurs in the ductile regime and cracking in the wafer can be avoided. After nanoscratching, a sharp silicon tip was employed to measure the topography of all the nanoscratch surfaces.

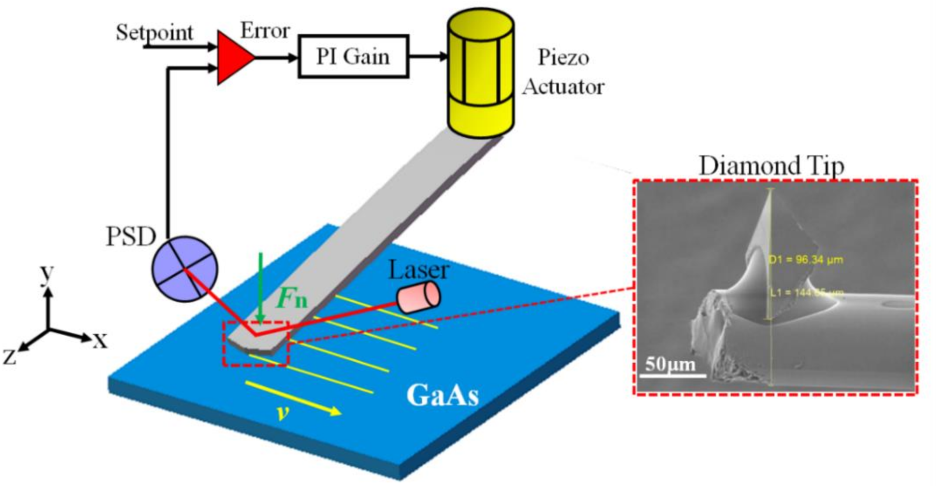

Figure 6.1 The schematic of AFM tip-based nanoscratching on single crystal GaAs.

6.3 Surface topography of the nanoscratches

The surface topography of various surfaces obtained at scratch depths of 0.5 nm, 1 nm, 1.5 nm, 2 nm, 2.5 nm and 3 nm are shown in Figure 6.2. The atoms in Figure 6.2 are coloured by height map by keeping the bottom of the scratch depth as the 0 nm datum and measuring the top pileup height in the increasing order. Thus, for instance, for a scratch depth of 0.5 nm, the bottom of the scratch surface is at the 0 nm datum, the theoretical surface reference surface would be 0.5 nm above the datum, which means if the height label reads at 0.8 nm, indicating a pile up height of 0.3 nm above the surface. From Figure 6.2, it may be seen that at shallower depths of scratch, the pile up scales linearly with an increase of the scratch depth. Also, the pile up occurred only at one prismatic side of the tool tip, which is due to the oblique cutting angle presented by the AFM tool tip.

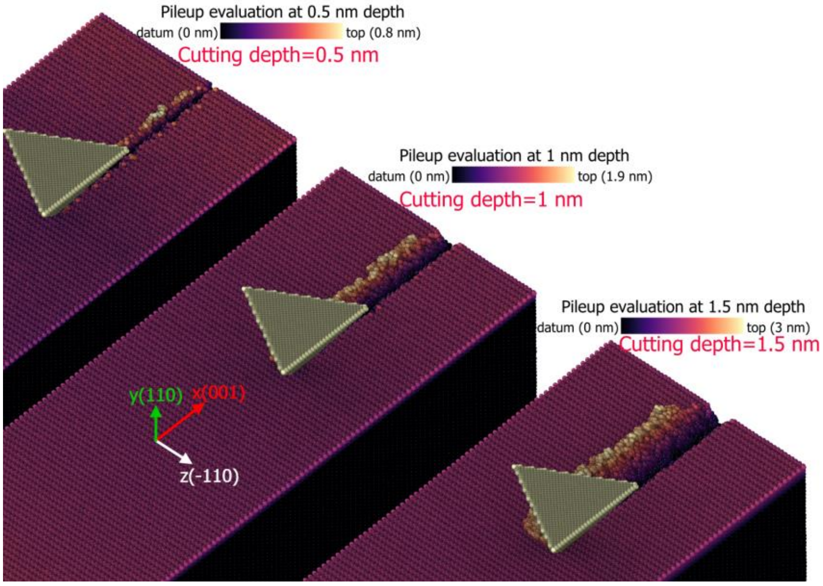

(i) Post-processed scratch topography measurement of GaAs at scratch depths of 0.5, 1 and 1.5 nm.

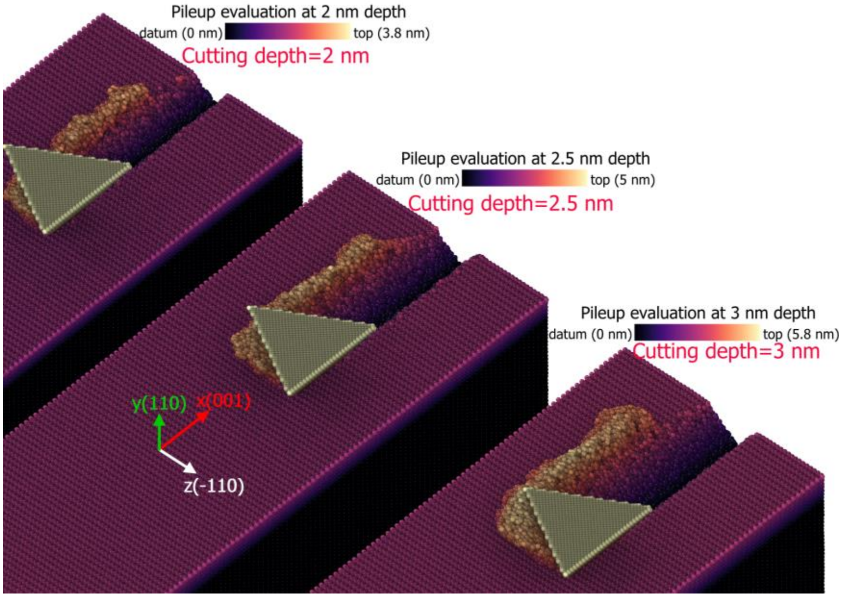

(ii) Post-processed scratch topography measurement of GaAs at scratch depths of 2 nm, 2.5 nm and 3 nm.

Figure 6.2 Assessment of the pile up, flow of cutting chips and nature of the chip flow during the material removal observed from the MD simulations. Colours represent height map of the atoms in the vertical Y direction.

The experimental AFM topography of the measured scratches is shown in Figure 6.3 (a). A total of 8 scratches were made in the AFM at various loads and their indicative scratch depths are plotted in the cross-section in Figure 6.3 (b). It shows that at shallow depths, the pile up occurred on one side. This is very similar to that observed during the MD simulation. The pile up at shallow depths can also be seen to scaling linearly with increasing depth.

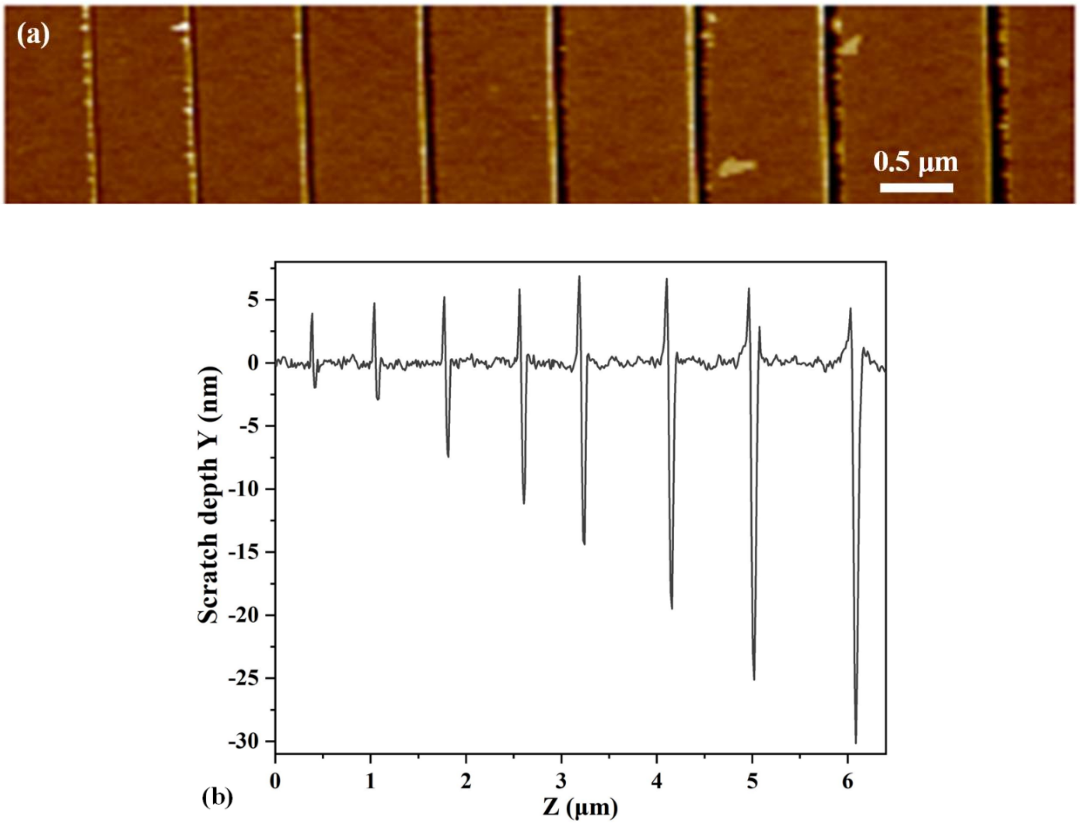

Figure 6.3 Measurement results by AFM (a) Surface morphology of various nanogrooves and (b) Height map of various scratches.

6.4 Forces, coefficient of friction and specific scratching energy

The evolution of the (i) friction force (*Fx*) – force acting in the direction of scratching and (ii) the normal force (*Fy*) – force acting in the direction perpendicular to the tool movement is shown in Figure 6.4. In addition to these, the resultant force described as the square sum of these forces was also estimated using the formulae ($Fr = \sqrt[2]{F_x^2 + F_y^2}$).

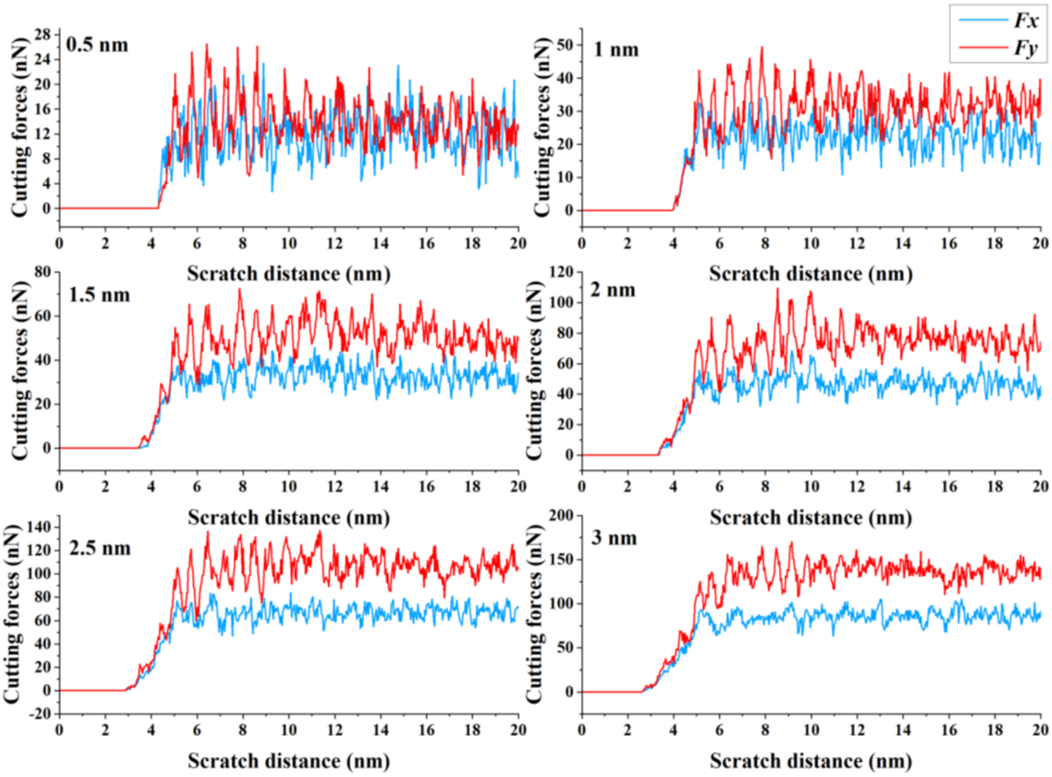

Figure 6.4 Evolution of the *Fx* and *Fy* at scratch depths 0.5 nm, 1 nm, 1.5 nm, 2 nm, 2.5 nm and 3 nm plotted with respect to the simulation time steps corresponding to a total scratch distance of 20 nm.

In the early stages of contact, the force increases from 0 to a certain value (in this regime, compression of the workpiece material is dominating), this regime is also referred to as an unsteady cutting state. Thereafter once the material starts to flow, the shear stress dominates and the force value becomes saturated. This regime is referred to as steady state cutting. With increasing depth of the scratch, the normal force can be seen to become higher than the friction force which speaks for the reduced coefficient of kinetic friction. Also, the magnitude of the *Fy* was larger than that of *Fx,* especially at higher scratch depth, which results from the active negative rake angle presented by the triangular pyramid tip similar to a cutting tool used in the machining of brittle materials like silicon during the single point diamond turning (SPDT) [232][194][219] or the grinding process [233]. The nature of forces can be seen to increase linearly with an increase of the depth of cut, as shown in Figure 6.5. The resultant force multiplied by the scratching distance and divided by the volume of the material removed gives a scalar quantity called specific scratching energy, which is considered independent of the size of the tool and is representative of the material's resistance to cutting at various depths. The estimated specific scratching energy obtained at various depths of scratches obtained from MD is shown in Figure 6.6. The nature of this variation was seen to follow an identical trend to that of the force ratio of the kinetic coefficient of friction (defined by *Fx/Fy*) shown in Figure 6.7. It was seen that the specific scratching energy was as high as 75 GPa with a kinetic coefficient of friction approaching a value of 0.87 at a shallow scratch depth of 0.5 nm. This value becomes more saturated at about 17 GPa and 0.62 at higher scratch depths of 3 nm. The steepness of this variation was mild for scratch depths between 1.5 to 3 nm but had a bigger slope of 70 GPa/nm within the scratch depth of 0.5 to 1 nm. The nature and trend of the force ratio and specific scratching energy was reminiscent of the previously reported work on aluminium discussed earlier in the introduction and hence clearly indicated a strong size effect in GaAs much like aluminium.

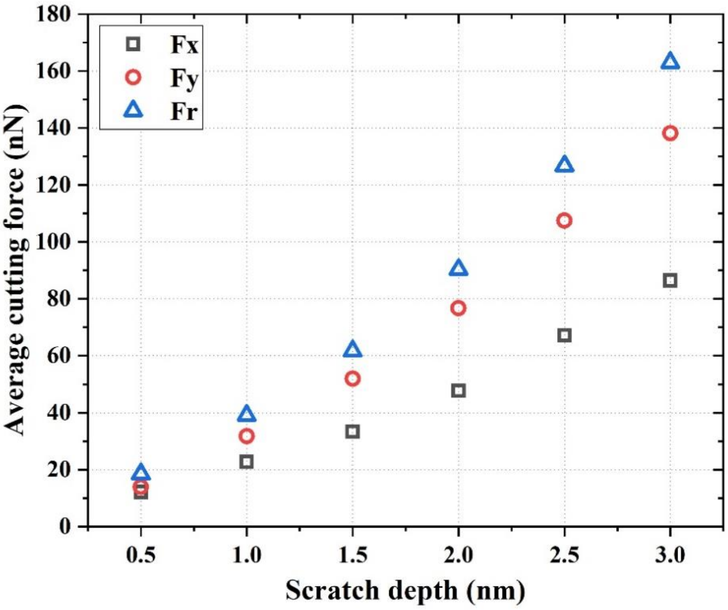

Figure 6.5 Variations in the cutting forces obtained from the MD simulations with Fr as the resultant force.

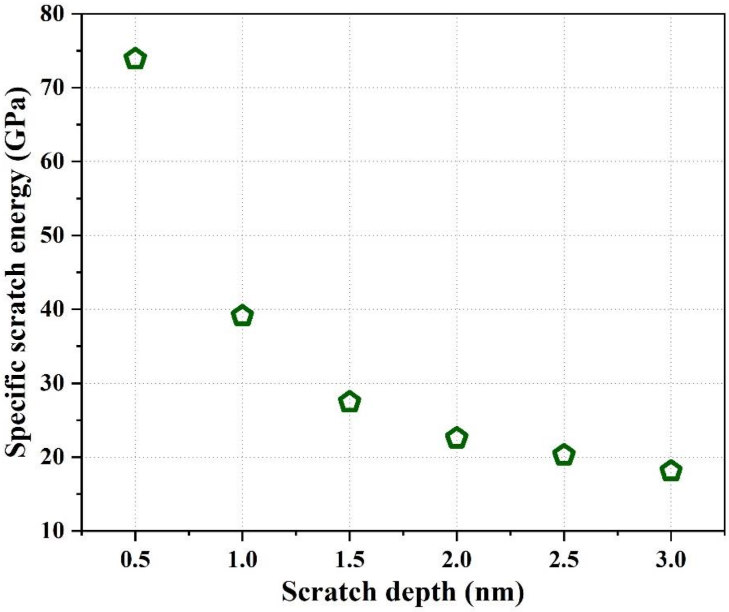

Figure 6.6 Variation in the specific scratch energy for different scratch depth cases obtained from the MD simulations.

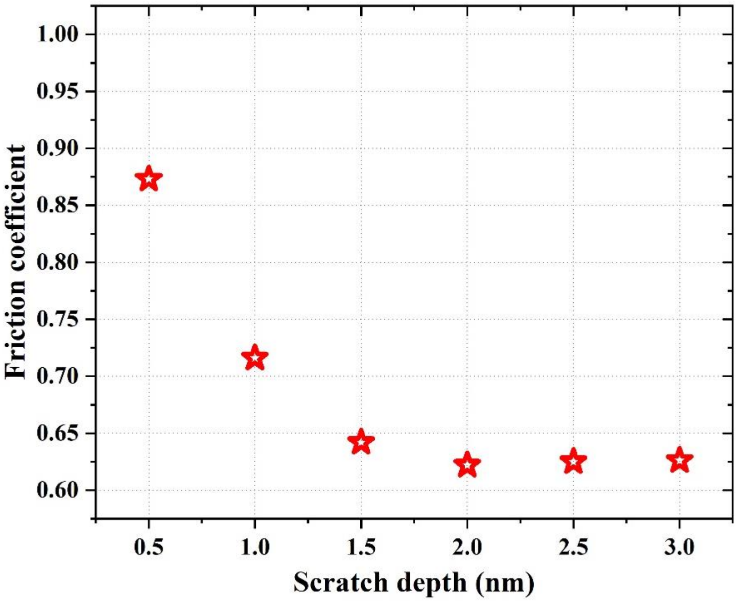

Figure 6.7 Variation in the friction coefficient for different scratch depth cases obtained from the MD simulations.

Figure 6.8 shows the corresponding AFM experimental results obtained for various scratches performed from 2 to 30 nm scratching depths. Not only the AFM experiments in common with the MD simulations showed an increasing magnitude of the cutting forces with the scratch depth, but the kinetic coefficient of friction also indicated a strong size effect. While the ratio of friction coefficient at a shallow depth of 2 nm scratch was close to unity, it reduced to almost a value of 0.55 at a higher scratch depth of >15 nm. This also indicated an influence of the included angle and the depth of the scratch. A sharper AFM tip can be expected to achieve a lesser coefficient of friction at depths below 15 nm which was the case seen in the MD simulation where the threshold of the size effect occurred at about 2 nm.

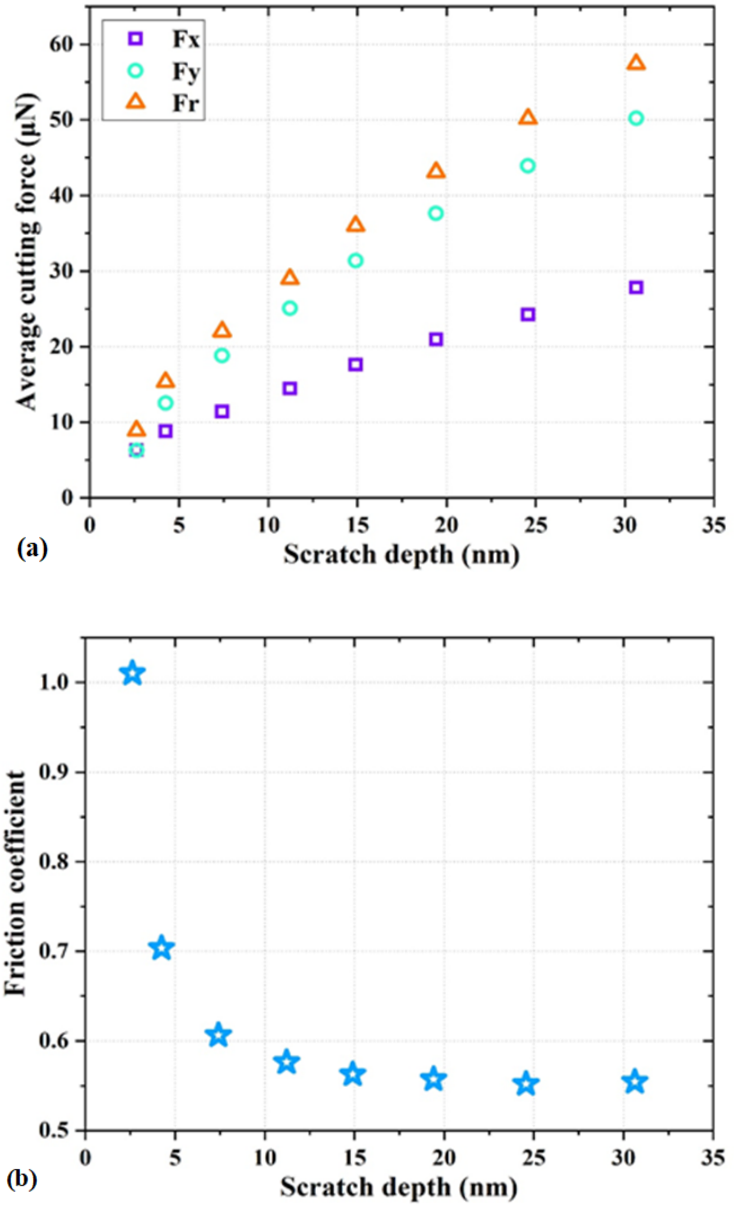

Figure 6.8 Variation in the (a) scratch forces and (b) kinetic coefficient of friction obtained from the AFM experiments.

s

6.5 Flow stress and plasticity

It is well known that the Tresca stress and von Mises stress can be used to predict yielding in ductile materials while a Principal stress criterion is more suitable to predict yielding in brittle materials [234]. Single crystal GaAs is hard and brittle at room temperature, but its chips are removed via the ductile-mode so this research looked into the stress tensors and yield criterion that can be applied to describe ductility in GaAs. To achieve this aim, the scalar stress values were obtained in the cutting zone. Here the atomic stress tensor was averaged temporally and then processed using established 3D stress mechanics theory [191], as shown in Figure 6.9. The detailed equations of 3D stress mechanics theory are demonstrated in appendix A. It became evident that the magnitude of von Mises stress in the cutting zone was ~6.89 GPa, which appeared close to the experimental nanoindentation hardness [235][236][237] of GaAs. The variation of von Mises stress in the cutting zone is shown in Figure 6.10. The result shows that both the von Mises and the minor Principal stress criterion can be used to predict yielding during ductile-mode cutting of GaAs.

A previous experimental work performed on studying doped GaAs material has indicated the possibility of phase transition from zincblende structure (GaAs-I) to rocksalt structure (GaAs-II) as responsible for the incipient plasticity [238]. Without offering any direct evidence of the phase transition and at pressures as high as < 12 GPa, the work suggested that the GaAs-I to GaAs-II transition causes the plasticity in the material. The fact that indentation hardness is representative of the plastic property of the material and coincides with the value of flow stress obtained in this work from the MD simulation seems to suggest that GaAs can flow plastically at a lower stress value than what's reported before [238]. Moreover, the stress required to cause a phase transformation from GaAs-I to GaAs-II phase is calculated to be of the order of 17.3 GPa which is very unlikely to occur during nanoscratching [239][240][241]. Hence, phase transformation can be ruled out as the reason of incipient plasticity.

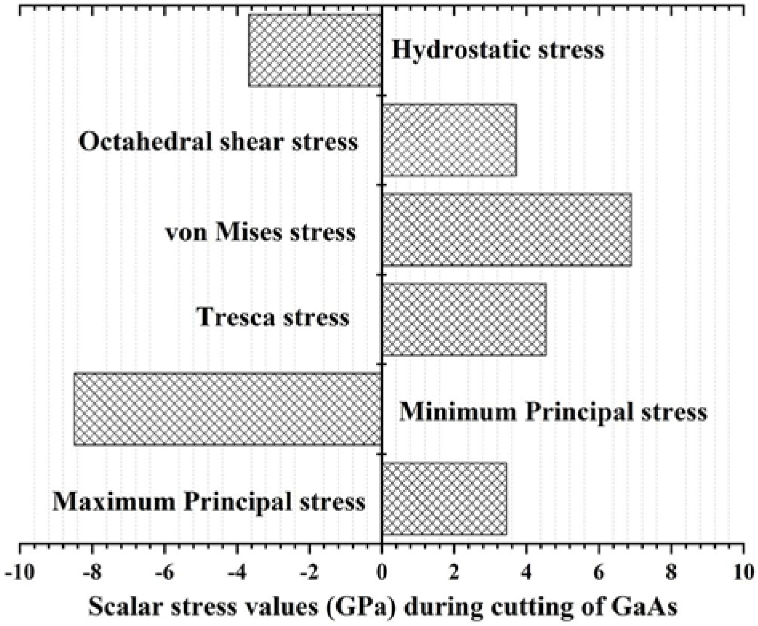

Figure 6.9 Scalar stress values (GPa) during cutting of GaAs.

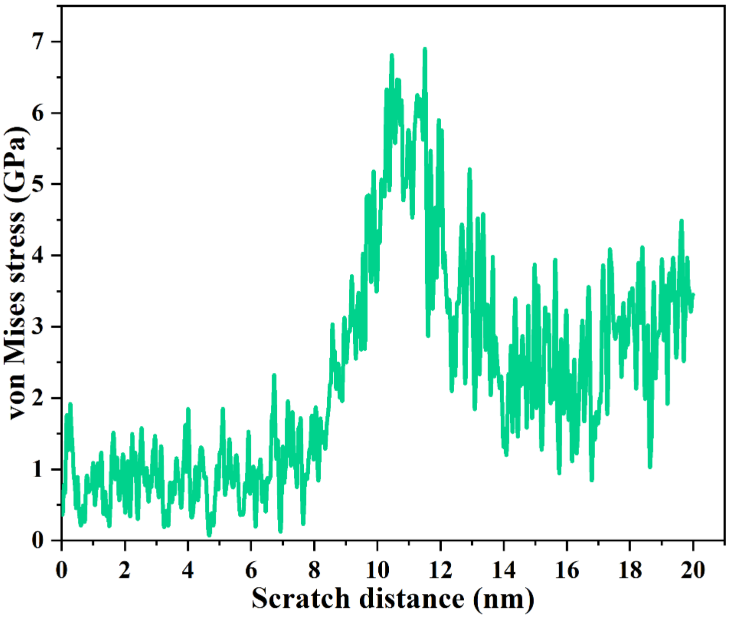

Figure 6.10 Variation in von Mises stress at scratch depth of 3 nm.

Furthermore, a Dislocation Extraction Algorithm (DXA) [180] was used to capture an instance of the emission of two dislocations in the sub-surface belonging to the Burgers vector family of 1/2<110> as shown in Figure 6.11. This explains that the nucleation of dislocation can occur much earlier than the phase transformation and hence, is energetically more favourable.

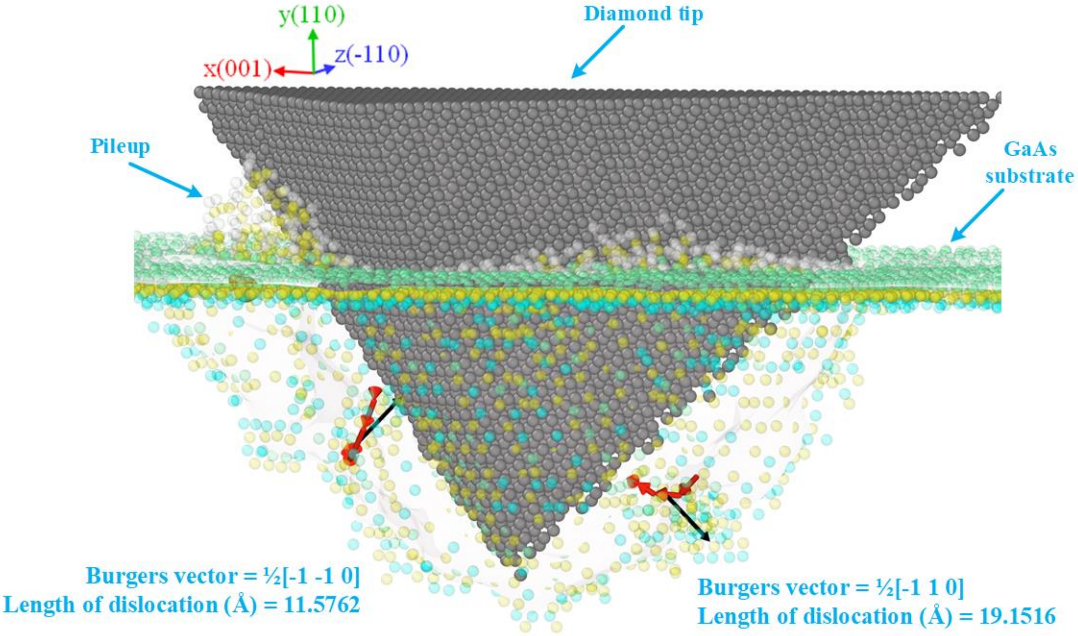

Figure 6.11 Observation of sub-surface at scratch depth of 3 nm.

Overall, if the potential function used in this investigation (Albe type) is to be trusted, then the dislocation nucleation occurring at a lower stress value of 7 GPa which coincides with the value of nanoindentation hardness (which is also a plastic property), seems to suggest that the primary reason for plasticity to occur in GaAs is dislocation nucleation which challenges the existing publication reporting phase transition to be responsible for the ductile plasticity in GaAs.

6.6 Remarks on comparing MD simulations with experiments

It is important to recognize that while a very good qualitative comparison is obtained in this investigation between the MD simulations and experiments, there are differences in the situations which cannot be neglected and needs further discussions. The experimental techniques involving the scanning probe microscopes such as the AFM and STM have large dependencies on the stiffness of the system (cantilever/tip) whereas the MD simulation assumes an infinitely rigid diamond tip. Moreover, the experimental results can easily be influenced by extrinsic factors such as the surface contaminants, surface state, the geometry of the slider, tilting of the substrate or the tip, impurities in the substrate and the contact conditions at the interface. Also, the cutting velocity employed during the AFM scratches was of the order of few micrometres per second (5 µm/s) as opposed to the velocity of 10 m/s used during the simulations. In view of this, the contact conditions during experiments were somewhat close to being quasistatic but more dynamic during the simulations which point us to strong strain rate effects in the MD. This should however not affect the hardness, or the flow stress and the elastic modulus usually obtained from the MD simulation studies.

It was necessary to employ higher cutting and/or sliding velocity to keep the computational requirements of the study within acceptable limits. Because of this, appropriate caution needs to be exercised in data interpretation. As such, the surface of the GaAs modelled in MD is atomically smooth and completely free of any contaminant and the entire process of scratching took place in a vacuum. Considering all these differences in the background, Figure 6.12 shows a comparison of the kinetic coefficient of the friction and the specific scratching energy for the range of depth investigated commonly between MD and the AFM experiments.

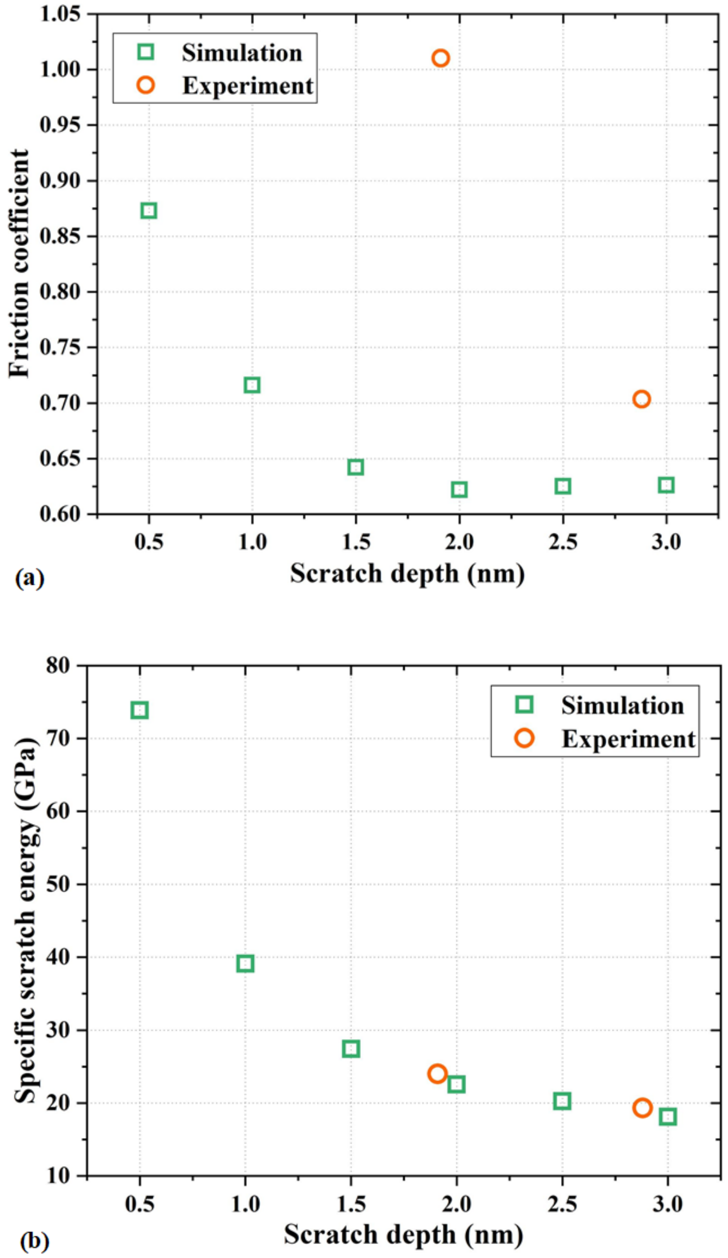

Figure 6.12 Comparison of the MD simulation and experimental results (a) Kinetic coefficient of friction and (b) specific scratching energy.

Figure 6.12 revealed that the comparison of the specific scratching energy showed good proximity between the MD simulation and experiments whereas the value of the kinetic coefficient of friction revealed differences. It points to the fact that the specific scratching energy could be insensitive to the velocity, geometry of the indenter but the kinetic coefficient of friction is perhaps governed by certain other factors which need to be further investigated. Especially, the force ratio was found to be substantially different at a very narrow depth of scratch of <2nm, which leads us to think and plan a follow-on work to investigate if this is due to previous surface amorphisation, or the roughness or due to the presence of an oxide layer as opposed to pure GaAs scratched in MD.

6.7 Summary

This chapter employed MD simulations and AFM scratch experiments to investigate the nanoscale friction and behaviour of material removal on single crystal (110)-oriented GaAs material surface. The results show a strong size effect was observed for scratch depths below 2 nanometres from the MD simulations and about 15 nm from the AFM experiments. The specific scratch energy is found to be a more dependable indicator than the kinetic coefficient of friction which maintains a constant value (0.55 in the MD simulation and 0.62 in the AFM experiments). Significantly, contrary to the published experimental results suggesting a phase transformation from GaAs-I to GaAs-II (zinc-blende to rocksalt phase) which can only occur at stress values <13 GPa, the simulations performed here using bond-order potential function (BOP) suggested that the von Mises stress values or the nanoindentation hardness can only reach up to 7 GPa. At this lower value of stress, the phase transformation cannot take place and instead, the incipient plasticity in single crystal GaAs during nanoscratching was observed to occur due to the 1/2<110> type dislocation nucleated in the sub-surface of the GaAs.

Chapter 7 Orthogonal and Oblique Nanomachining of GaAs

7.1 Introduction

During SPL, a prismatic shape tip acted as a cutting tool to perform the subtractive nanomachining. Correspondingly, the alignment of the prism can significantly influence the accuracy and quality of the machined surfaces. Hyon et al. [22] employed diamond tip to generate 10 nm narrow nanogrooves on GaAs surface. However, they did not consider the tip alignment effects in their investigation. Yan et al. [130][242] reported the effects of tip alignment while machining a ductile copper metal. However, in contrast to hard and brittle, copper is malleable and ductile which can easily be machined without any issues. The most important question remains unanswered: how GaAs will respond to the differently oriented diamond tips during nanoscratching? Therefore, this chapter will investigate the influence of differently oriented diamond tip on the chip flow behavior. Moreover, this chapter will also reveal the formation mechanism of sub-surface damage of single crystal GaAs in nanomachining via MD simulation and high resolution transmission electron microscopy (HRTEM) characterization of machined surfaces.

In addition, gradual diamond wear during nanomachining process can undermine the brittle-to-ductile transition condition and result in transition of ductile regime machining to brittle fractures [243]. On the other hand, catastrophic wear of diamond tip can lead to stress concentration in the cutting zone which results in microcracks and fractures. Single crystal diamond and polycrystalline diamond tools have been experimentally observed to undergo different wear mechanisms, such as diffusion wear [244], thermo-chemical wear [245], abrasive wear [246], graphitization [247] and chemical diffusion [248]. Correspondingly, this chapter will reveal the wear mechanism of diamond tip in order to find a solution to mitigate the wear of diamond tip during high-volume production of GaAs-enabled devices in the future.

7.2 Orthogonal and oblique nanomachining experimental setups

The prismatic shape diamond tip has three scratching faces. Figure 7.1 (a) shows the tip scratching face is tilted with an inclination angle (θ) with the scratch direction, which is equivalent to oblique cutting in conventional machining as illustrated in Figure 7.1 (b). Consequently, the protuberances tilt at an angle and are squeezed onto one side. Here, the inclination angle, θ, is defined as the angle between the directions of scratching and cutting face. Figure 7.2 (a) shows that two inclination acute angles were involved in AFM scratching, which suggests this scratching manner is oblique cutting with double cutting sides. Figure 7.2 (c) indicates an oblique cutting process with one obtuse angle and one cutting side. Figure 7.2 (b) is equivalent to the conventional orthogonal cutting. For brevity, we named them as OBCDS, ORC and OBCSS, respectively.

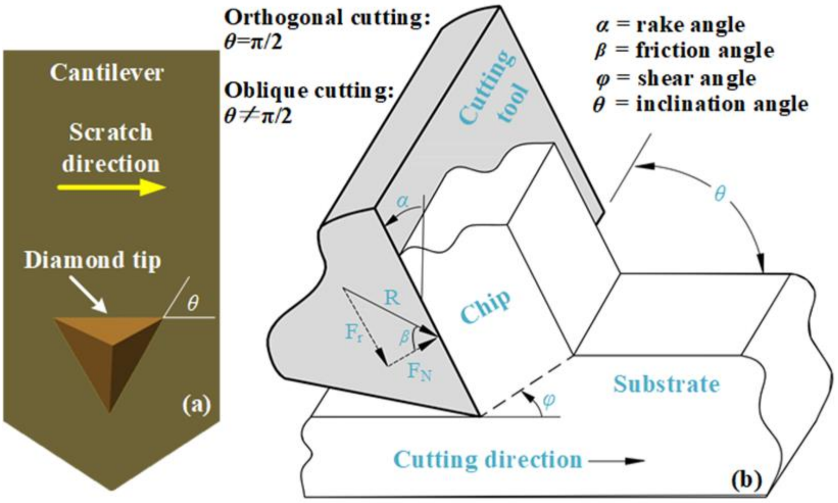

Figure 7.1 (a) Oblique cutting in AFM scratching with prismatic shape tip. (b) Conventional oblique machining.

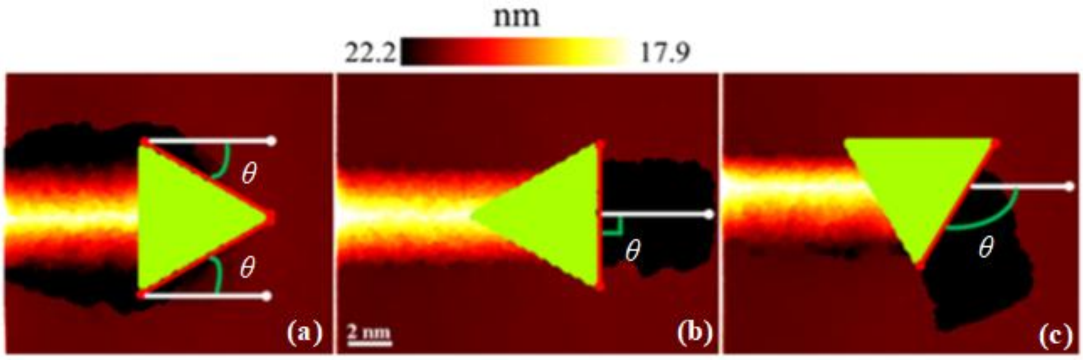

Figure 7.2 (a)(c) Oblique cutting in AFM scratching. (b) Orthogonal cutting in AFM scratching.

As mentioned in chapter 6, the generic prismatic sharp diamond tip (Micro Star Technologies Ltd. (US)) was employed to carry out the nanoscratching experiments on the 0 0 1) substrate surface of a single crystal GaAs wafer (diameter of 10 mm, thickness of 0.5 mm, PI-KEM Ltd. (UK)) with OBCSS, OBCDS and ORC along the <1 1 0> direction, which has been reported as the hardest cutting direction [7], on a commercial AFM platform with Nanoman module (Dimension Icon, Bruker Corporation, Germany). The schematics of the nanoscratching experiments is shown in Figure 7.3. The normal load (F_N) varies from 31 μN to 63 μN under an applied voltage from 0.25 V to 0.5 V. The normal load was set small to ensure that the nanoscratching was implementing in the ductile regime without causing cracks and fractures. After nanoscratching with each method, a sharp silicon tip was employed to measure the morphology of the nanogroove. Meanwhile, the scratched surface was imaged by a SEM (Quanta 200FEG, FEI, USA). TEM specimens (a thickness of <100 nm) was prepared by a focused ion beam (FIB) system (FEI Helios Nanolab G3 UC DualBeam microscope) and was then observed by a TEM (FEI Tecnai F20, USA).

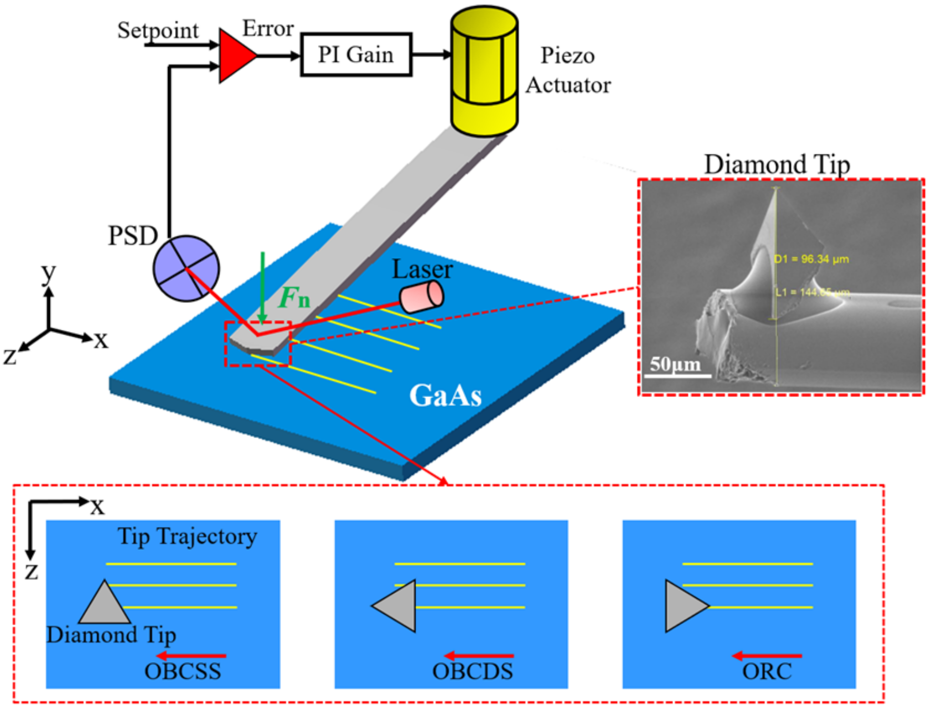

Figure 7.3 The schematics of the nanoscratching experiments with prismatic shape diamond tip by atom force microscope (AFM).

7.3 Chip flow behavior

In this section, three different nanoscratching manners i.e., OBCDS, ORC and OBCSS, were carried out during MD simulations and nanoscratching experiments. Additionally, the depth of cut remained under serval nanometers to enable ductile regime scratching to take place. The results of MD simulations were demonstrated from three perspectives i.e., three-dimensional (3D) morphology image, two-dimensional (2D) surface morphology image colored along the Y direction and the cross-sectional scatter plot in Y and Z direction. The result of nanoscratching experiments were shown in the aspects of SEM image, AFM image and cross-sectional profile of created nanogroove. In terms of OBCDS, an obvious pileup on both sides of the nanogroove was observed from the result of MD simulation, as shown in Figure 7.4 (a-c). In particular, no chip formation in the front of the diamond tip was found, implying the ploughing was the primary material removal state during OBCDS process instead of cutting. No chip formation has been approved in experiments as shown in Figure 7.5. It is plausible that ploughing took place. The cross-sectional profile (see Figure 7.5 (c)) from AFM image (see Figure 7.5 (b)) demonstrates the material piled evenly up on both sides of the nanogroove, which is same as the MD simulation result (see Figure 7.4(c)).

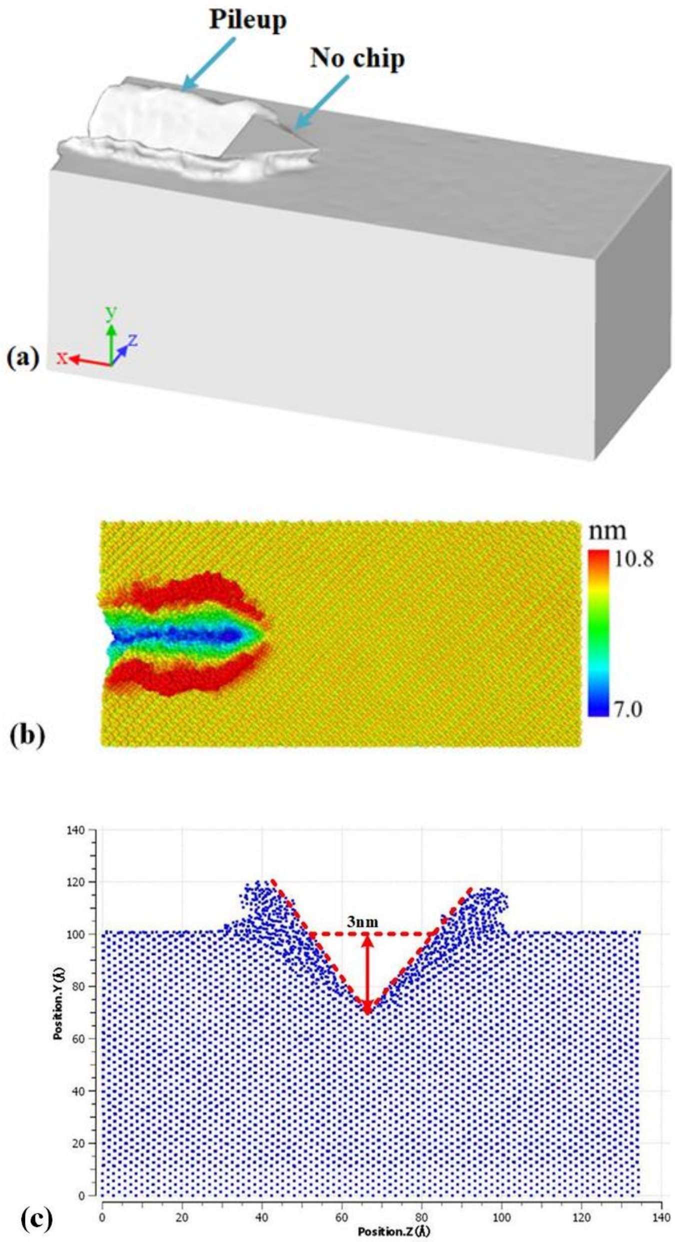

Figure 7.4 The results of MD simulation of OBCDS. (a) 3D morphology, (b) 2D surface morphology colored along the Y direction, and (c) Depth of nanogroove.

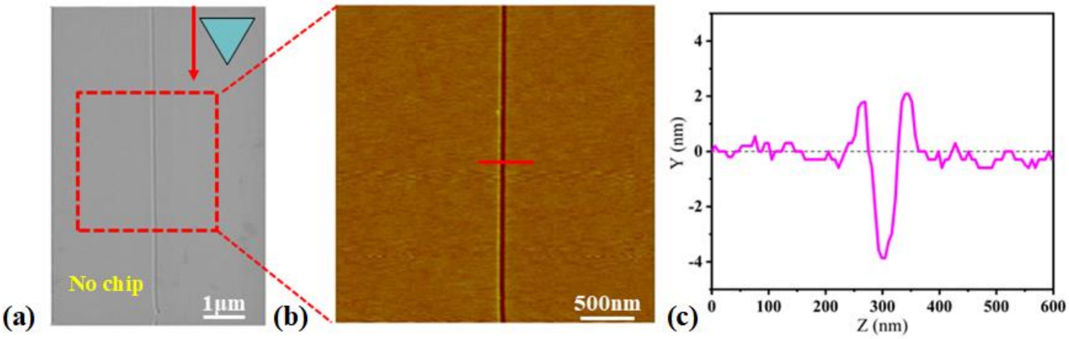

Figure 7.5 OBCDS experimental test on the GaAs surface (a) SEM image of nanogroove, (b) AFM image of nanogroove, and (c) Cross-sectional profile of nanogroove.

In ORC, high-volume continuous chip was formed in the front of the diamond tip, as shown in Figure 7.6 (a)(b), which induced by compression via a larger contact interface area between workpiece and tip. Conversely, few materials piled up on the surface of the nanogroove (see Figure 7.6 (b)(c)). In experiment, chip and burrs (see Figure 7.7 (a)) were found beside the nanogroove and material piled barely up on both sides of the nanogroove (see Figure 7.7 (b)(c)), which validates the result of MD simulation (see Figure 7.6 (a-c)) of ORC.

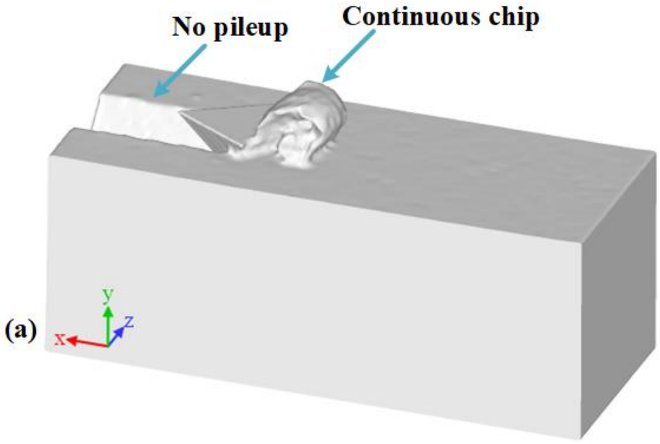

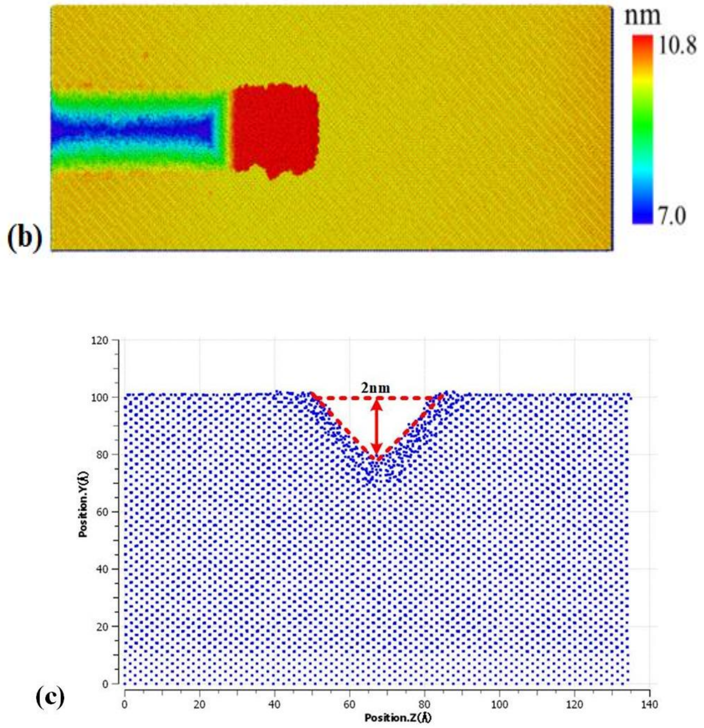

Figure 7.6 The results of MD simulation of ORC. (a) 3D morphology, (b) 2D surface morphology colored along the Y direction, and (c) Depth of nanogroove.

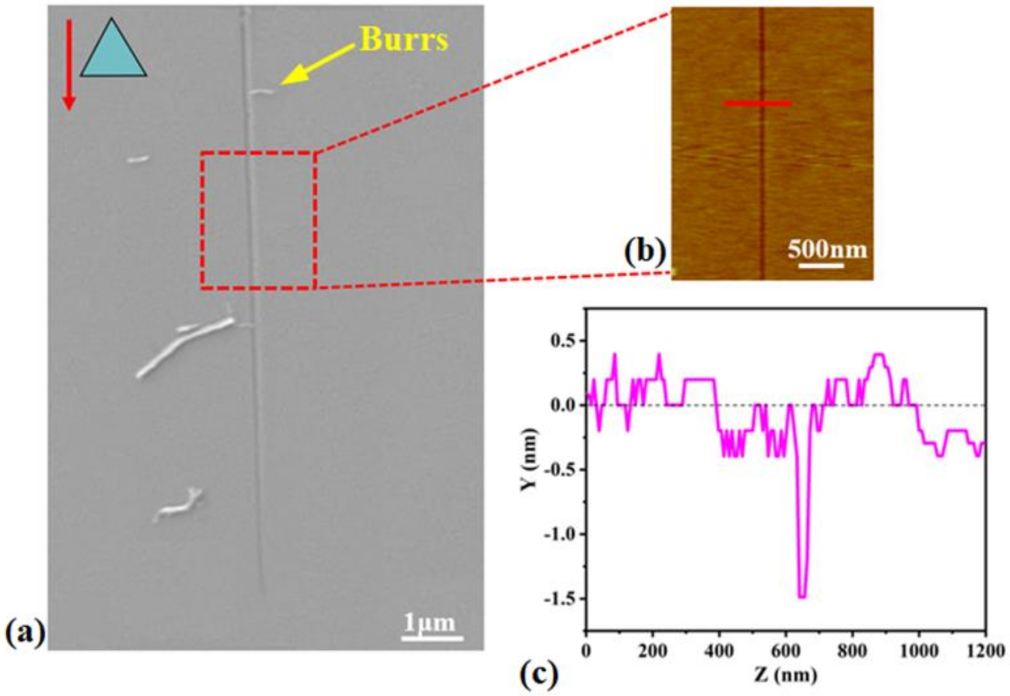

Figure 7.7 ORC experimental test on the GaAs surface (a) SEM image of nanogroove, (b) AFM image of nanogroove, and (c) Cross-sectional profile of nanogroove.

In OBCSS, it is evident to see the sidewall pileup and formed chip on the surface of the nanogroove, as illustrated in Figure 7.8 (a)(b), which is consistent with the experiment result (see Figure 7.9 (a)). Additionally, several smooth and continuous belt-type chips were formed at the end of the nanogroove. Unlike in ORC, no burrs were found on both sides of the nanogroove. The same format of sidewall pileup was found in MD simulation (see Figure 7.8 (c)) and Figure 7.9 (c) of nanoscratching experiment (see Figure 7.9(c)). Most material piled up on one side of the nanogroove and a little bit material piled up on the other side. This is attributed to the geometry of the diamond tip, where β is obvious bigger than α, as shown in Figure 7.8 (c). Therefore, the presence of different angles changes the direction of chip flow. Additionally, through comparing the scratched depth of the nanogroove between Figure 7.4 (c) and Figure 7.5 (c), between Figure 7.6 (c) and Figure 7.7 (c), and between Figure 7.8 (c) and Figure 7.9 (c), it can be seen that OBCDS could reach the same scratched depth with the preset 3 nm depth of cut in MD simulation. The ORC had the smallest scratched depth about 2 nm, while the scratched depth of OBCSS was intermediate at 2.5 nm. This result is ascribed to the nanoscratching manner under different tip alignments which could lead to different material structural plastic recovery. Additionally, a comparison of the depth of cut under different normal loads (see Figure 7.10) also validates the results of MD simulation: the OBCDS could create the biggest depth of cut followed by OBCSS and then ORC, respectively.

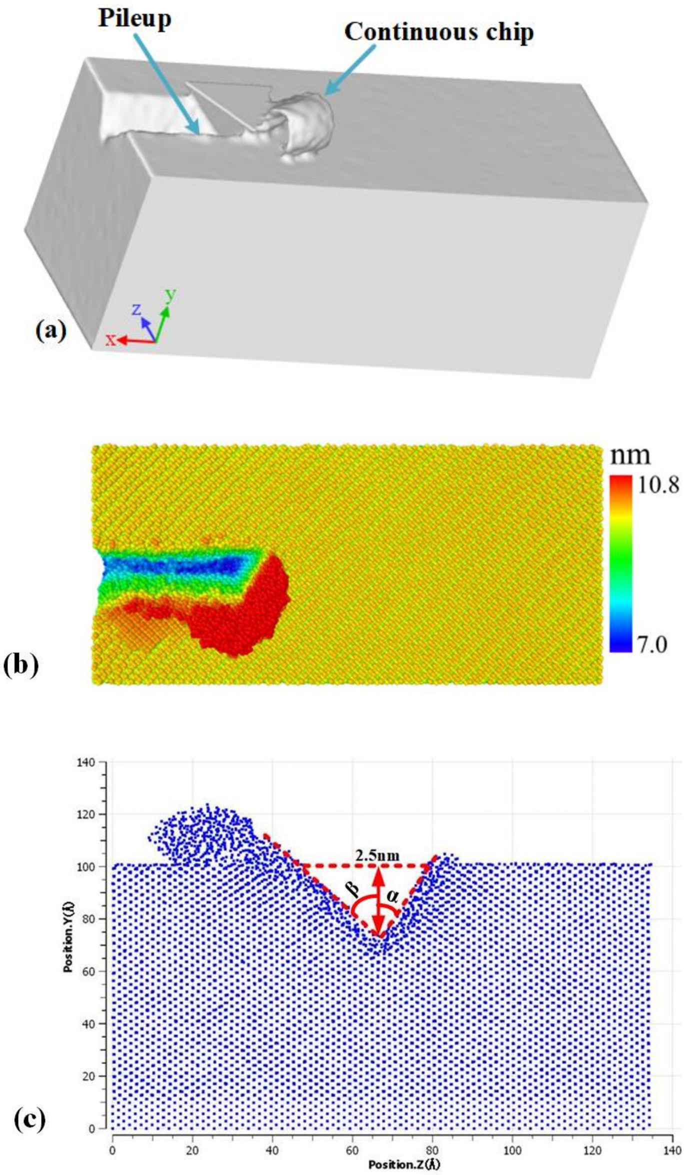

Figure 7.8 The results of MD simulation of OBCSS. (a) 3D morphology, (b) 2D surface morphology colored along the Y direction, and (c) Depth of nanogroove.

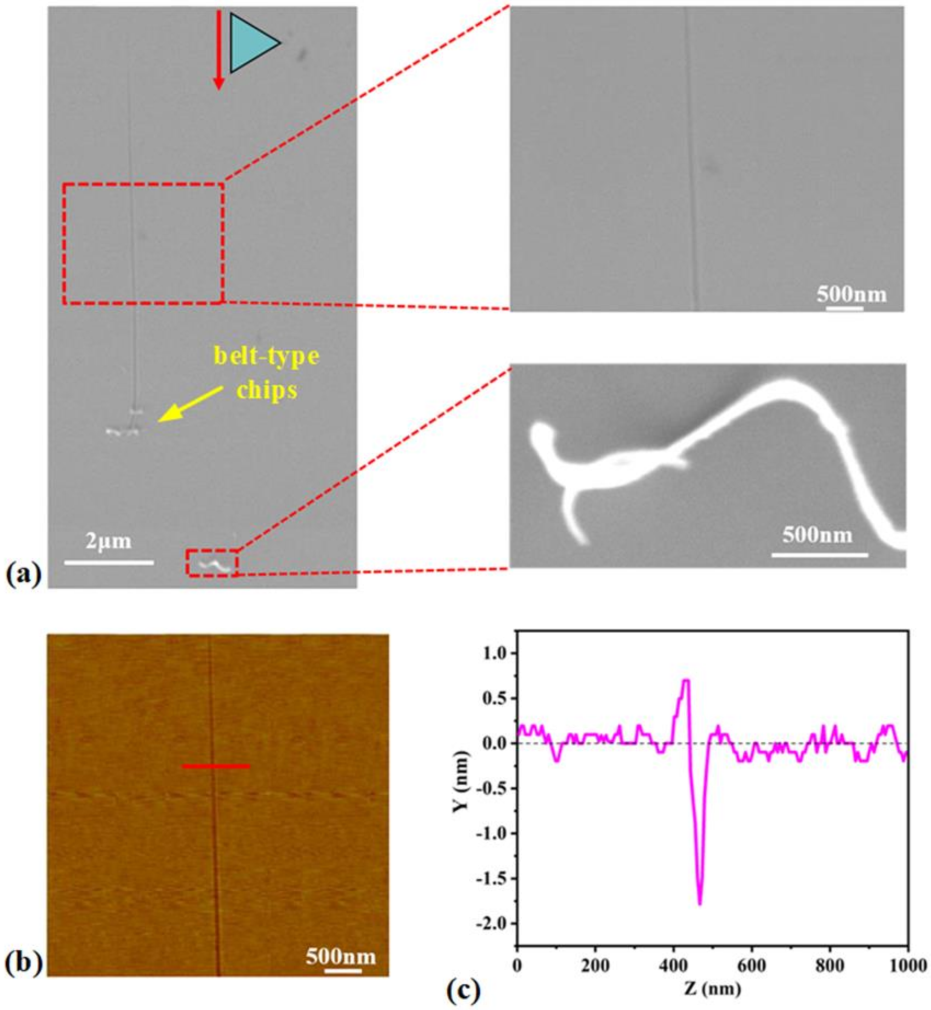

Figure 7.9 OBCSS experimental test on the GaAs surface (a) SEM image of nanogroove, (b) AFM image of nanogroove, and (c) Cross-sectional profile of nanogroove.

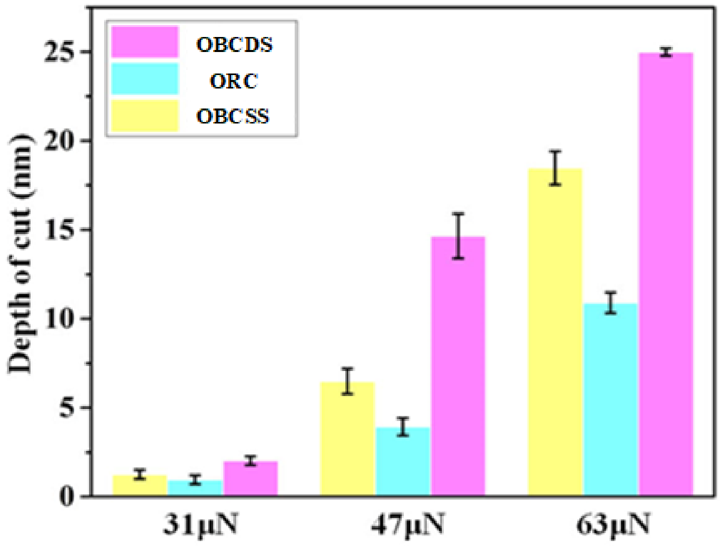

Figure 7.10 The scratched depth of the nanogroove under different normal loads from the experimental tests.

7.4 Cutting forces and temperatures under different tip alignments

Figure 7.11 demonstrates the variation of scratch forces *Fx, Fy* and *Fr* against scratch distance under three cases. Much importantly, it shows that the resultant scratch force *Fr* raised rapidly when the diamond tip gradually penetrated into the single crystal GaAs (Stage I) and fluctuated steady after the diamond tip entered into the workpiece thoroughly (Stage II). Furthermore, the Stage I demonstrates an interesting growth trend for these three cases. ORC shows the fastest increasing trend which is attributed to the large compression contact area. Subsequently, OBCDS shows relatively slow increase trend due to the initial pure shear induce mechanism. The increase trend of OBCSS is intermediate, which results from the combined action of shear and compression. Additionally, OBCDS had the biggest average scratch force (see Figure 7.12) with biggest coefficient of friction (COF=*Fx/Fy*) (see Figure 7.13). OBCSS had the smallest COF (see Figure 7.13) with smallest average scratch force (see Figure 7.12). Specific cutting energy (e in GPa) is defined as a ratio of the work performed (cutting force × distance travelled) by the cutting tool to the volume of material removed, as shown in Figure 7.14. A reduced specific cutting energy signifies the weaker cutting resistance. Alignment of diamond tip, therefore, has significant influence on the cutting force (up to 29.98% reduction), COF (up to 11.27% reduction) and specific cutting energy (up to 20.55% reduction). A comparison of Figure 7.12, 7.13 and 7.14 shows OBCSS can achieve a relative deep depth of nanogroove with the smallest cutting resistance, which will facilitate prolonging the life of diamond tip.

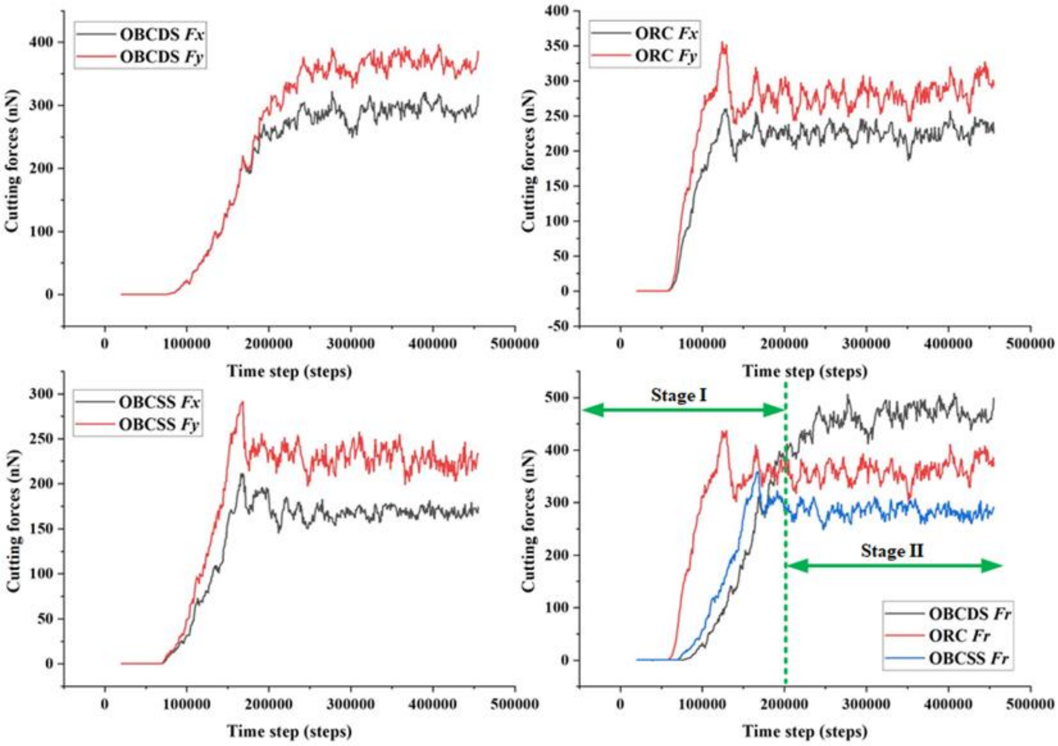

Figure 7.11 Variation in scratch force Fx, Fy and Fr with scratch distance under three cases in MD simulations.

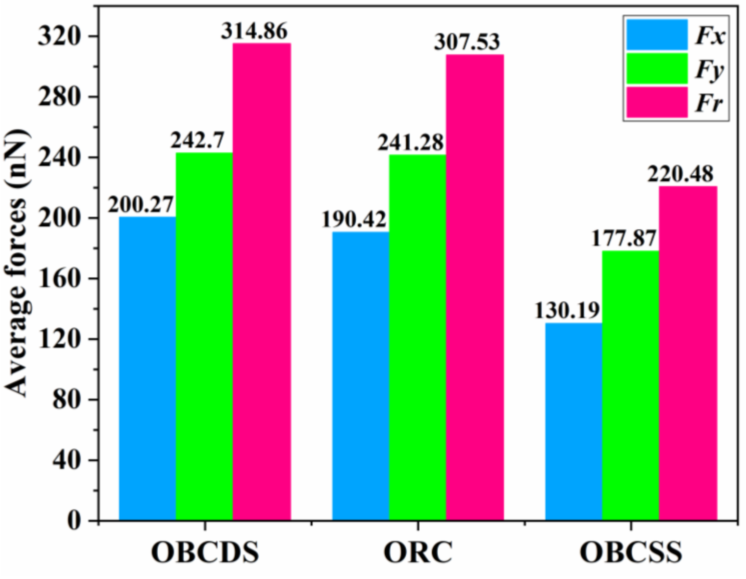

Figure 7.12 The average value of lateral force *Fx*, normal force *Fy* and resultant force *Fr* for three cases in MD simulations.

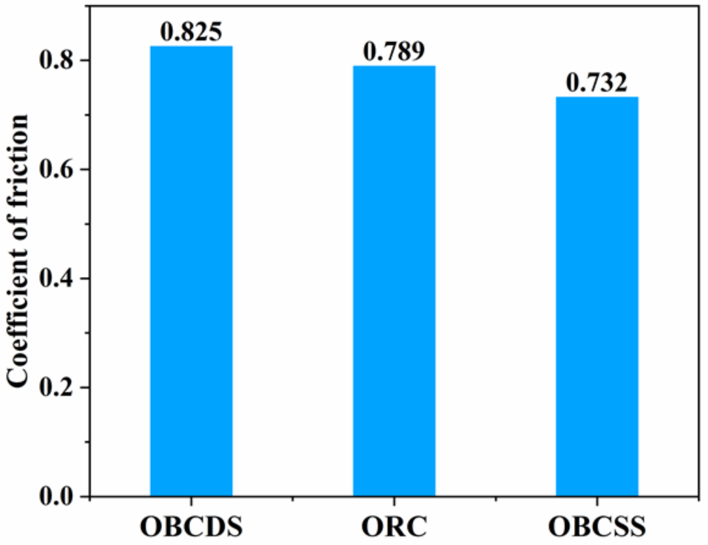

Figure 7.13 The average value of coefficient of friction (COF) for three cases in MD simulations.

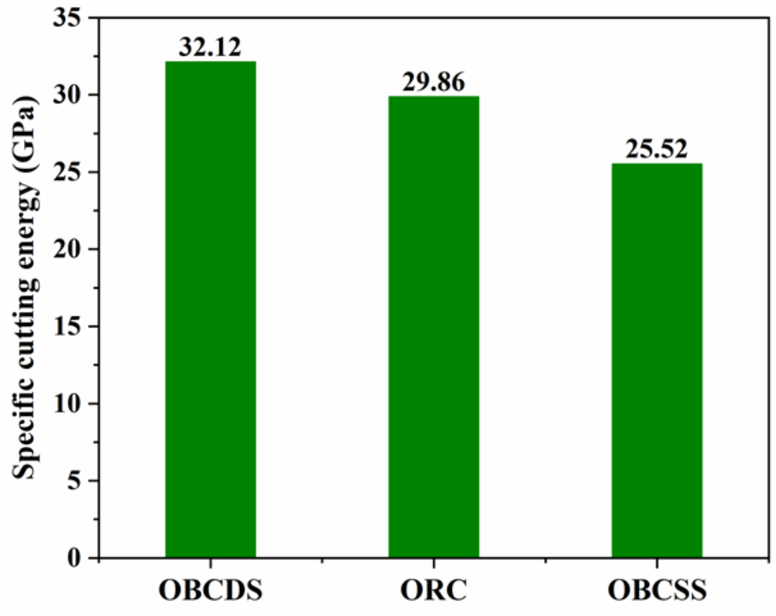

Figure 7.14 The specific cutting energy for three cases in MD simulations.

Figure 7.15 shows that the average temperature of the cutting zone went up with the scratch distance. The ORC had the fastest growth trend which is attributed to more bond breaking and energy release in single crystal GaAs, while OBCDS shows the slowest growth trend of temperature and the OBCSS was intermediate among three cases.

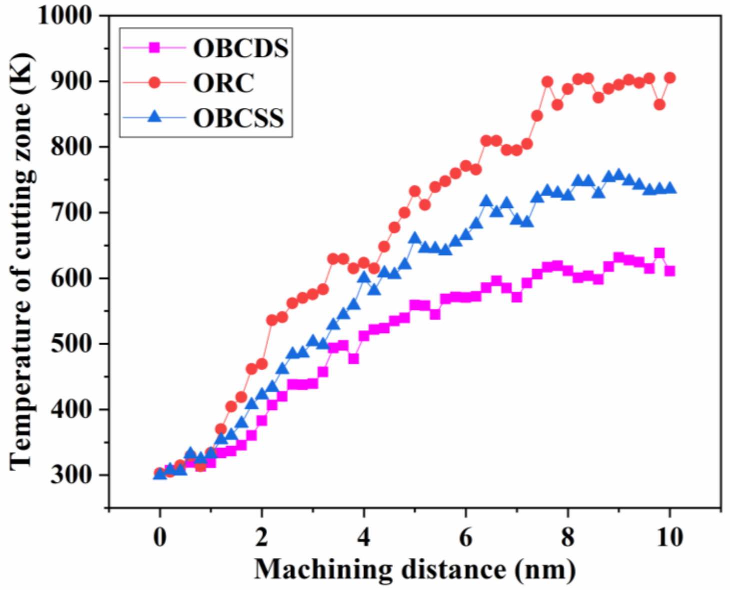

Figure 7.15 Evolution of the average temperature in the cutting zone against scratch distance under three cases in MD simulations.

7.5 Formation mechanism of sub-surface damage

The automated dislocation extraction algorithm (DXA) and crystal analysis tool (CAT) was used to detect and identify sub-surface activity in single crystal GaAs. Figure 7.16 shows the sub-surface damage depth for oblique cutting and orthogonal cutting. The MD simulation results indicate OBCDS has the minimum sub-surface damage, followed by OBCSS and ORC. From what has been discussed in section 7.2, we safely draw the conclusion that the OBCDS can achieve the deepest depth of cut with least sub-surface damage layer. According to section 7.3, OBCSS was identified to experience the smallest cutting resistance on single crystal GaAs. Therefore, considering reducing the wear of diamond tip, OBCSS was selected to fabricate a set of nanogrooves to achieve a direct observation of sub-surface damage by TEM. Additionally, the formation mechanism of sub-surface damage does not depend on either oblique or orthogonal cutting manners. Therefore, this section only chooses to analyze the MD simulation result of OBCSS case for brevity.

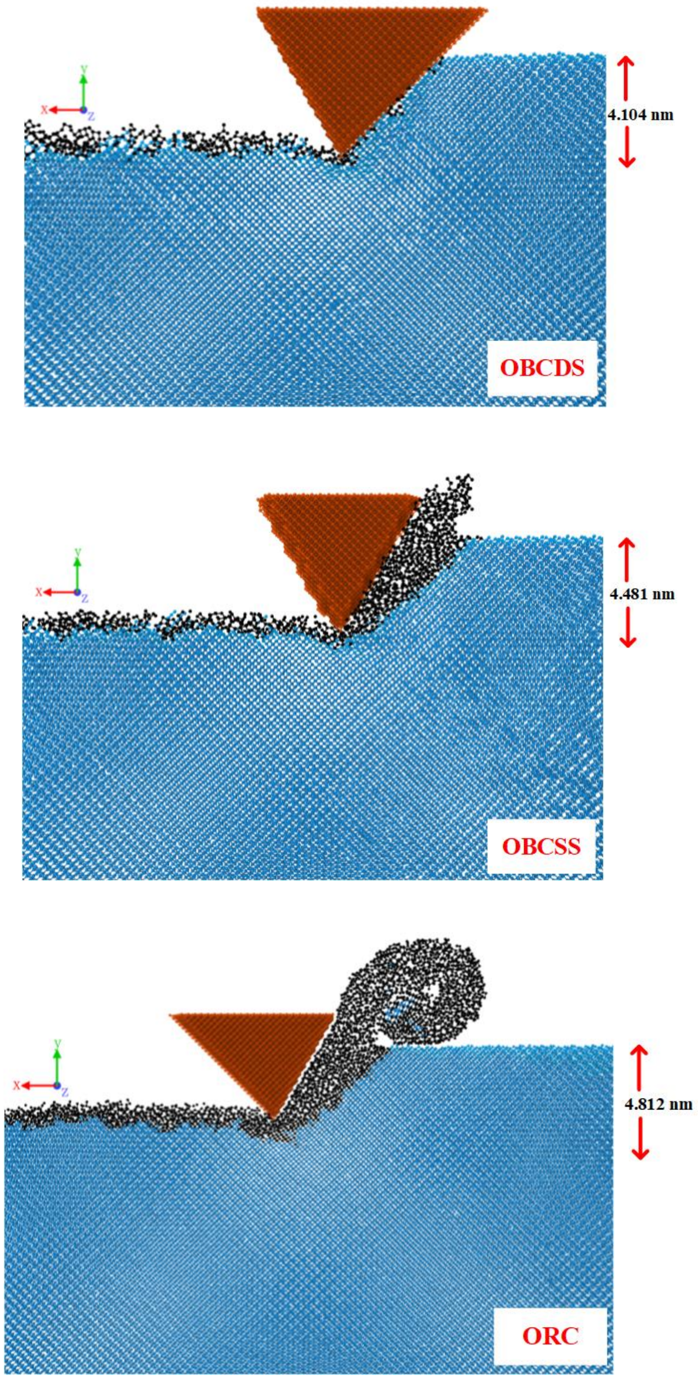

Figure 7.16 The sub-surface depth in the MD simulations.

Figure 7.17 shows various types of dislocation clouds underneath the machined surface in OBCSS. The dislocation extraction algorithm indicated four types of dislocation nucleation with their Burgers vector as 1/2<110>, 1/6<112>, <0-11> and 1/2<1-12>. It can be seen that the predominant dislocation nucleation with the 1/2<110> type dislocation emanates from the primary shear zone of the GaAs substrate. It was also observed that the 1/2<110> type dislocation dissociated into Shockley partials, 1/6<121> (30°) and 1/6<211> types (60°) dislocations interconnected by an intrinsic stacking fault (ISF). This phenomenon of dislocation dissociation has commonly been observed in silicon under moderately applied stress and temperature conditions [249]. This phenomenon shows level of similarities in the way zinc-blende structure yields akin to a diamond lattice structure. Additionally, the dislocation loops, multi dislocation nodes and dislocation junctions were observed in the sub-surface defect cluster, as show in Figure 7.18.

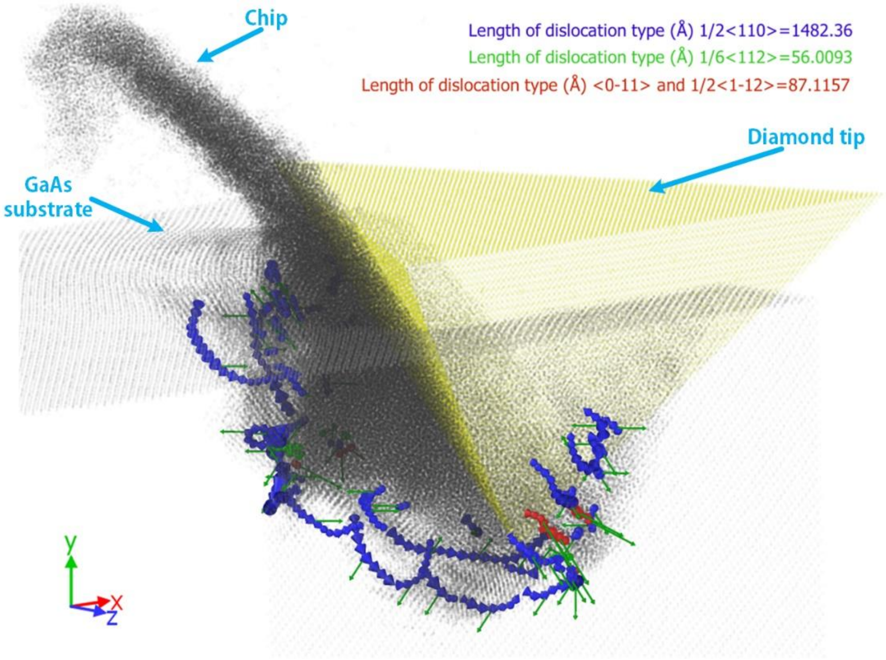

Figure 7.17 Dislocation nucleation during scratching of GaAs at a cutting distance of 10 nm.

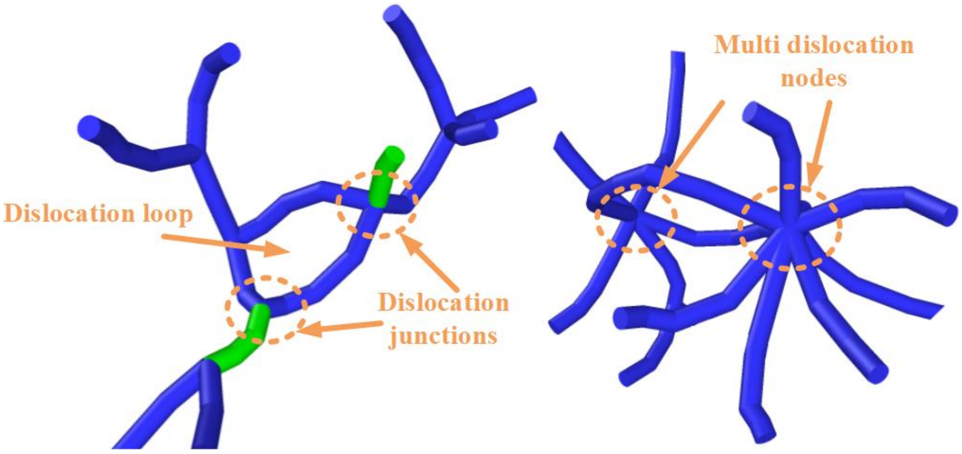

Figure 7.18 Dislocations evolution in the sub-surface of single crystal GaAs.

The cross-sectional of a machined sample was cut off by using a focused ion beam (FIB) perpendicularly to the scratching direction and was lifted out using an in situ micromanipulator attached to a specimen holder, as shown in Figure 7.19 (b)(c). As illustrated in Figure 7.20 (a), a common deformation zone is clearly observed in the subsurface of the five nanogrooves by TEM. Moreover, the deformation zone consisted of high-density dislocations and stacking faults due to high shear stress and high pressure induced by the diamond tip, as shown in Figure 7.20 (b)(c)(d)(e). Significantly, a deeper dislocation extended zone was observed underneath the deformation zone. It can be found that almost all the dislocation extended along the $(\bar{1}\ \bar{1}\ \bar{1})$ and $(\bar{1}\ 1\ 1)$ planes according to the diffraction pattern in Figure 7.20 (a). This suggests that the {1 1 1} is the slip system in nanomachining of single crystal GaAs. Furthermore, as the existing of the dislocation types (1/2<110> and 1/6<112>), we can conclude a dual slip mechanisms i.e. shuffle-set slip mechanism and glide-set slip mechanism occurred in the sub-surface damage during AFM-based nanoscratching process on single crystal GaAs [249].

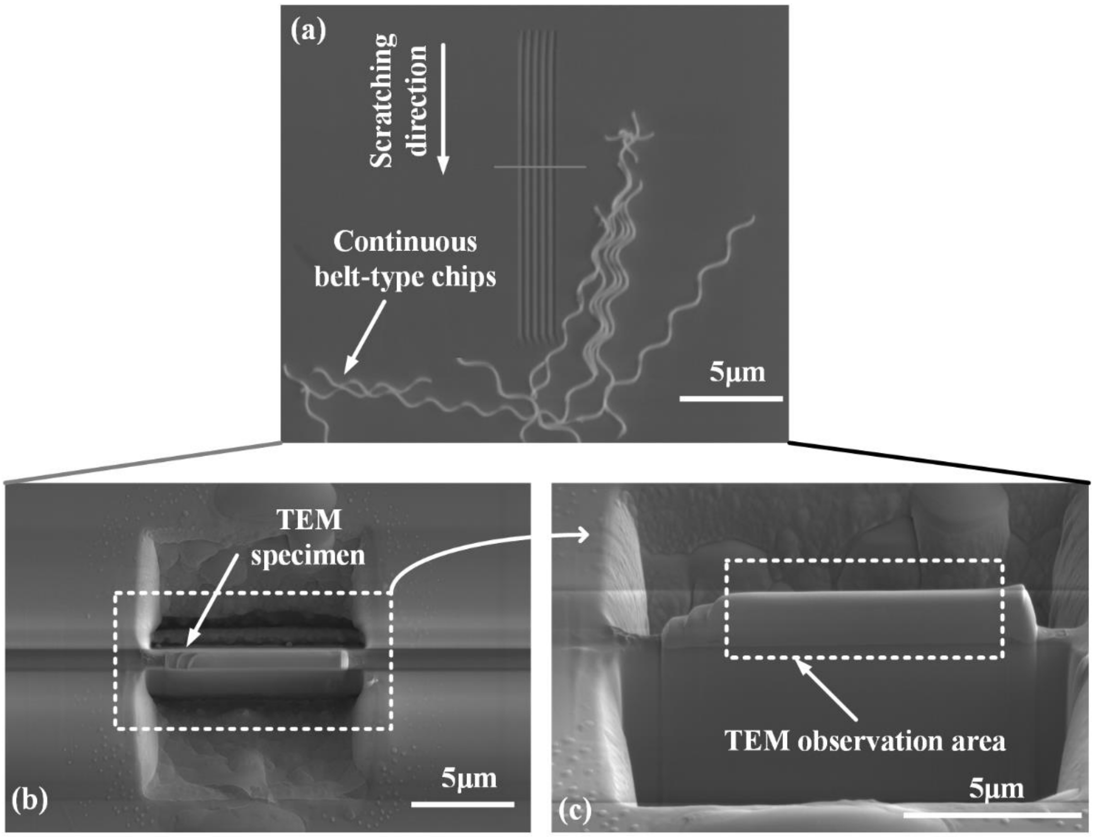

Figure 7.19 (a) The morphology of the nanogrooves. (b) The location of the specimen preparation by FIB in situ. (c) The location of TEM observation.

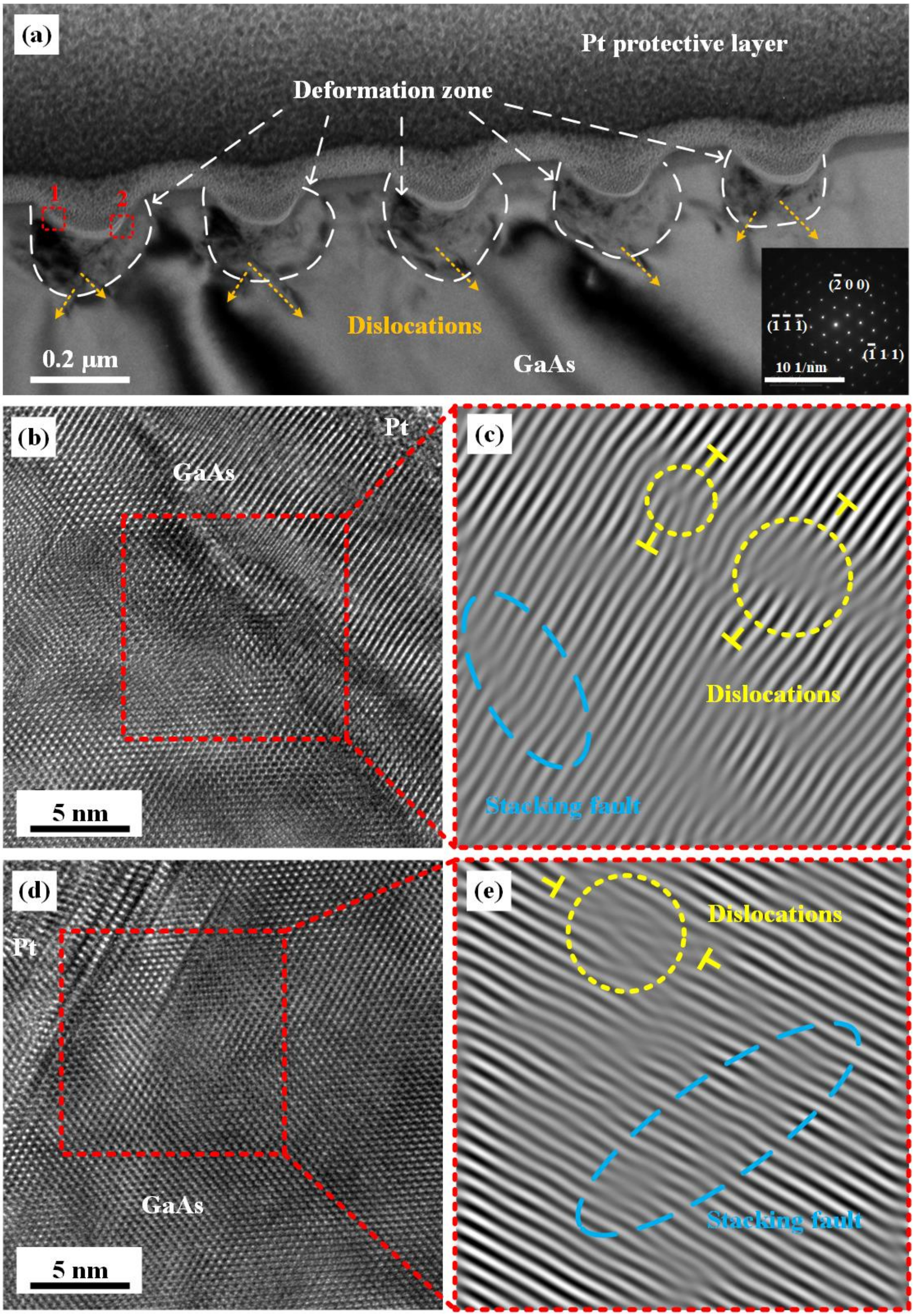

Figure 7.20 (a) The bright field TEM image of the subsurface with diffraction pattern. (b)(d) HRTEM images of marked regions 1 and 2. (c)(e) Fast Fourier transformation (FFT) patterns.

7.6 Wear mechanism of diamond tipss

7.6.1 Deformation of diamond tip

As shown in Figure 7.21, the diamond tip experienced elastic-plastic deformation during the nanomachining process caused by a sp^3-sp^2 hybridization transition. The deformation hotspot appeared at the apex of the diamond tip, meanwhile, the cutting edge of the diamond tip showed incipient deformation. Furthermore, from Figure 7.22, it can be observed that the maximum atomic displacement of the apex of the diamond tip could reach 0.12 nm. The occurrence of diamond tip elastic-plastic deformation behavior is attributed to high pressure acting on the diamond tip structure [250][251].

Moreover, from the enlarged diagrams of the apex of the diamond tip shown in Figure 7.21, it is apparent that a hexagonal structure with two C-C bond gaps (as shown in Figure 7.21 (b)) forms at the cutting distance of 2 nm. With the nanomachining advancement, an irregular hexagonal structure, as illustrated in Figure 7.21 (c), was observed at the cutting distance of 6 nm. Then, a complete hexagonal carbon-cycle structure occurred at the distance of 10 nm, as demonstrated in Figure 7.21 (d). Subsequently, the measured bond angle and bond length of C-C were 121° and 1.41 Å, respectively. This is very close to the graphite hexagonal lattice structure with 121° C-C bond angle and 1.42 Å C-C bond length [252][253]. Finally, at the cutting distance of 20 nm, the presence of a clear sp^2 graphite layer structure was observed, as seen in Figure 7.21 (e). This phenomenon suggests that the apex of the diamond tip transformed from an initial sp^3 hybridization diamond lattice structure to sp^2 graphite lattice structure due to the C-C bond transformation and reorganization of bonds. From this, we can infer that the graphitization governs the wear mechanism of diamond tip during AFM tip-based nanomachining of GaAs. Correspondingly, thermal and shear stresses were analyzed in the subsequent sections to investigate the underlying mechanism of graphitization of the diamond tip thoroughly. Further advancement of the machine leads to the graphite layer of diamond to fall off and separated from the diamond tip and create a small concave structure, previously reported by Cheng et al. [254].

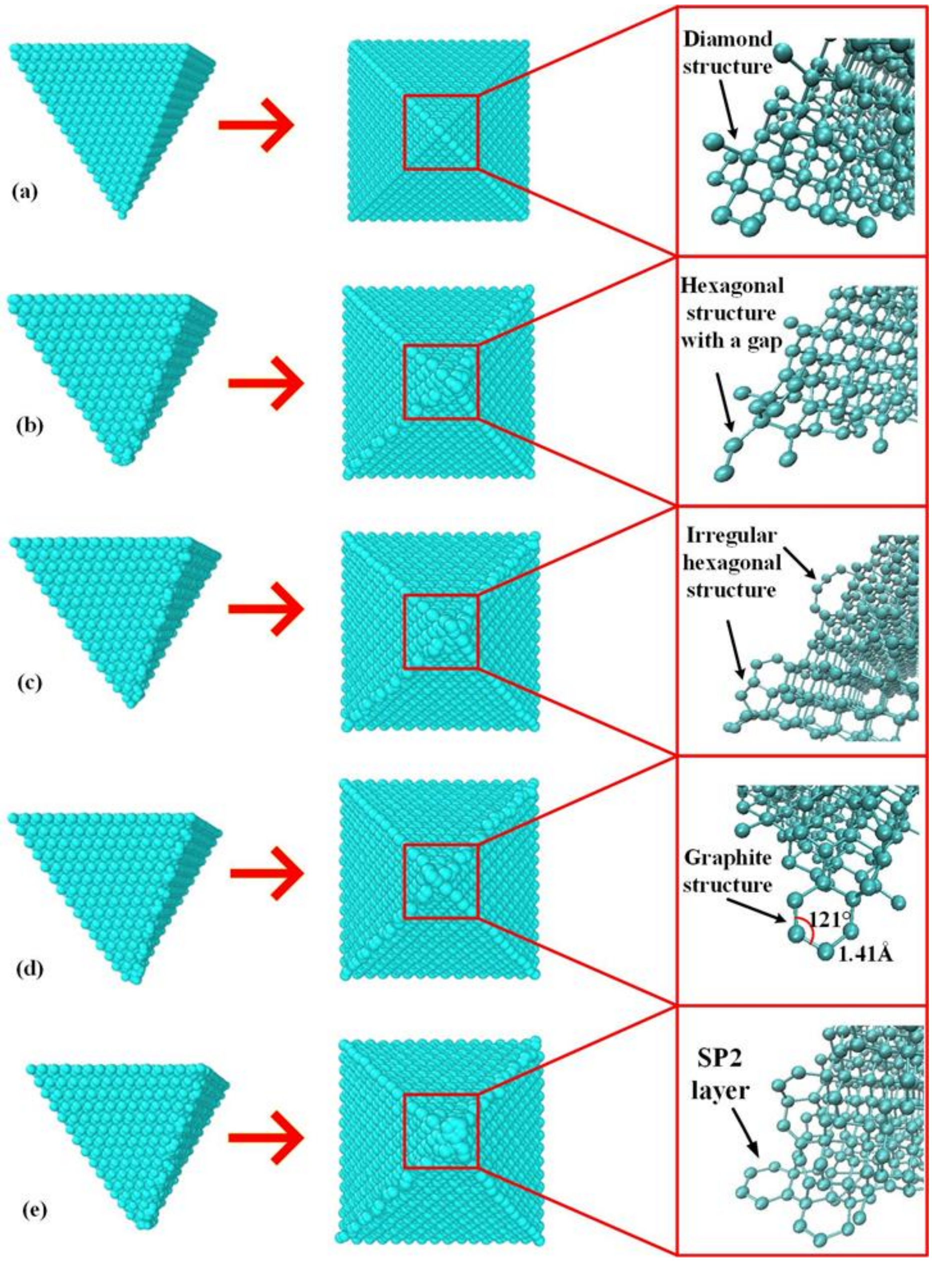

Figure 7.21 The observation of structural change of the diamond tip during nanometric cutting of GaAs. (a) initial diamond tip structure. (b-e) the diamond tip structures at the cutting distances of 2 nm, 6 nm, 10 nm, and 20 nm, respectively.

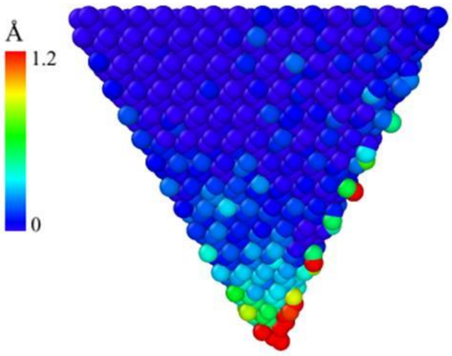

Figure 7.22 The atomic displacement of the carbon atoms in the diamond tip after a nanomachining distance of 10 nm.

7.6.2 Shear stress state of diamond tip

It has been reported by some researchers that the cubic diamond lattice structure can transform to hcp graphite lattice structure under high shear stress state [255][256]. Therefore, the high shear stress is a considerable factor to investigate the underlying mechanism for the graphitization of the diamond tip. The evolution of stresses on the diamond tip estimated from the simulations is shown in Figure 7.23. It was found that the average shear stress fluctuated at a magnitude of 7 GPa. In addition, as shown in Figure 7.24, after the cutting distance of 10 nm, the peak shear stress was mainly located at the apex of the diamond tip. The magnitude of stress was much lower than the shear stress of 95 GPa that was required to induce the cubic diamond lattice instability to the hcp graphite lattice structure [257]. This indicates that besides shear some other factor also contributes to causing the graphitization of diamond tip during nanometric cutting of single crystal GaAs.

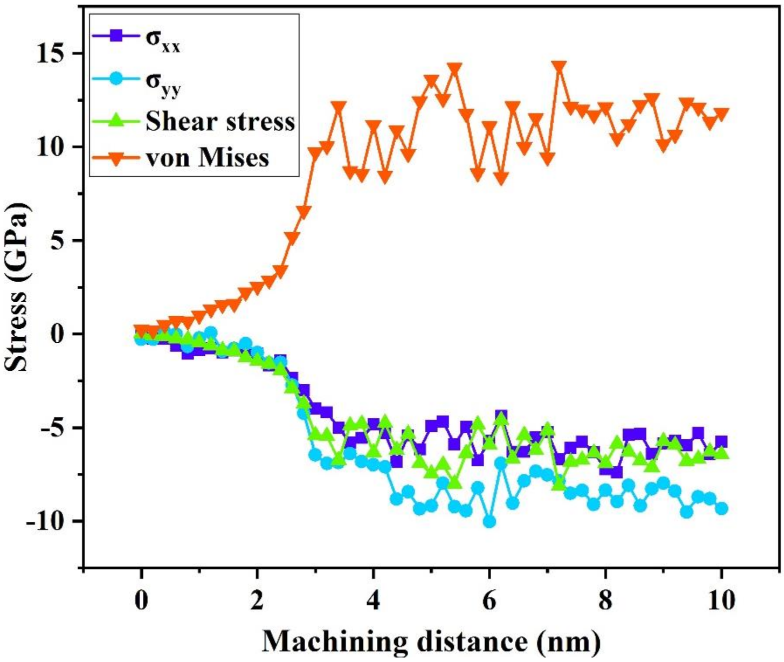

Figure 7.23 The stresses variation on the diamond tip.

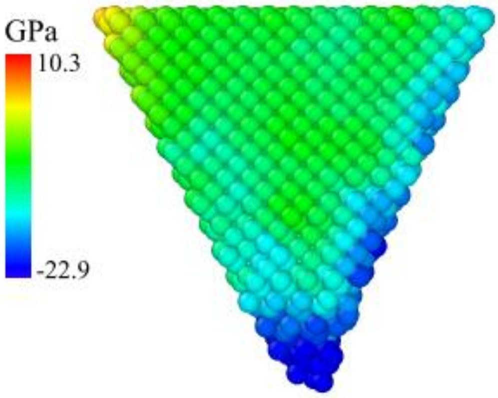

Figure 7.24 The distribution of shear stress at the diamond tip after the cutting distance of 10 nm.

As earlier shown in Figure 7.23, the stress components σ_{xx} and σ_{yy} variation kept fluctuating between -6 GPa and -10 GPa indicating the compression state of the diamond tip. The von Mises stress was computed over the simulation period, which is employed to predict the yielding and shape distortion of the GaAs material [258][259].

The average von Mises stress of the diamond tip experienced a relatively stable stage at around 12.5 GPa between the cutting distances 4 nm and 10 nm.

7.6.3 Thermal state of diamond tip

Another significant potential factor that may cause graphitization of the diamond tip is the cutting heat. The average temperature of the diamond tip dramatically increased at the start of the nanometric cutting, as illustrated in Figure 7.25 (b), and then kept steady at approximately 600 K. The stable average temperature rise of the diamond tip with the increase of cutting distance might be attributed to the quick heat dissipation thanks to the high thermal conductivity of diamond [260]. Another observation from Figure 7.25 (a) was that the locally highest temperature around 950 K was concentrated at the apex of the diamond tip, which was also the place of initiation of graphitization. It is known that the minimum temperature required to cause the graphitization of diamond is about 940 K under anaerobic conditions [261], which is basically the same as the high temperature of the apex of the diamond tip based on the simulation results with the same simulation environment. Therefore, it implies that the high temperature at the apex of the diamond tip might weaken the cohesion energy of the C-C bond and further lead to the reorganization of the C-C bond with the advancement in the nanometric cutting [254][262]. Correspondingly, cutting heat appears to have triggered the sp^3-sp^2 hybridization transition of the diamond tip. Additionally, the relation between higher cutting speed and the temperature at the tip of the diamond tool could be uncovered by conducting more MD simulations in the future.

more MD simulations by higher cutting speeds will be conducted in the future to discuss the

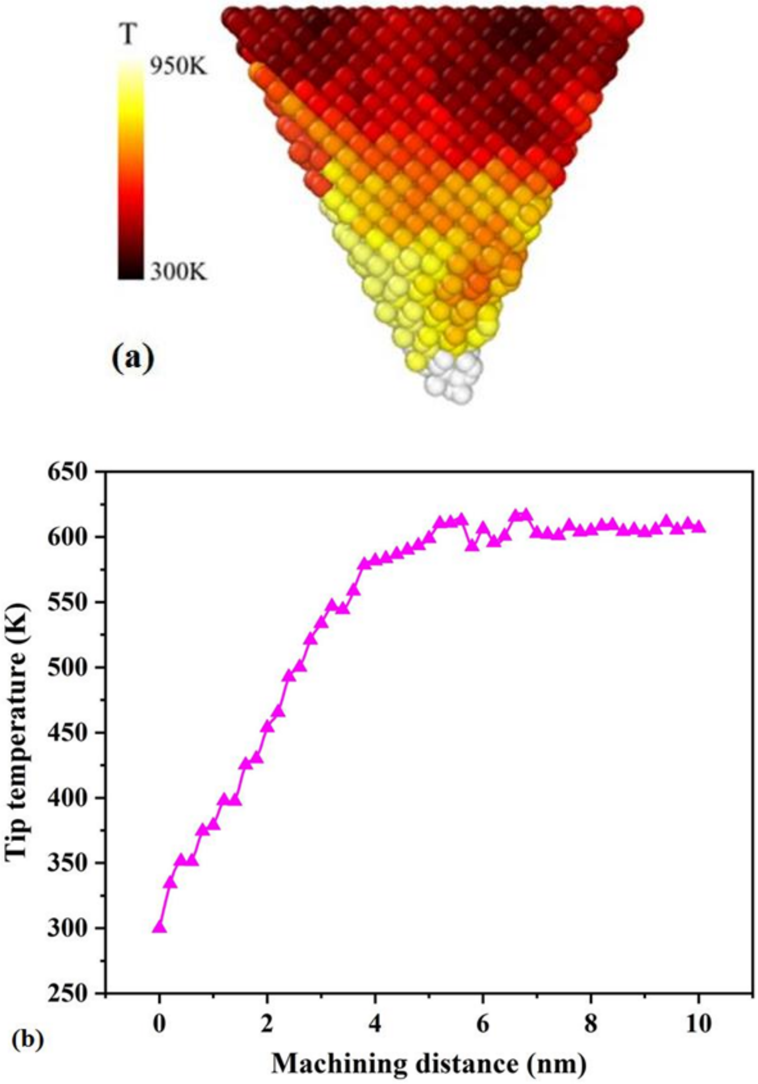

Figure 7.25 (a)The temperature distribution of diamond tip at nanomachining distance of 10 nm. (b)The average temperature evolution of diamond tip.

7.6.4 Graphitization conversion rate of diamond tip

It is well known that diamond has a coordination number of 4 while graphite has a coordination number of 3. In this chapter, the graphitization conversion rate of the diamond tip was quantified by the division of the number of graphitized atoms to the total atom number (13107 atoms) of the diamond tip. To eliminate the influence of dangling bonds (292 atoms) of the diamond tip surface, the total number of s graphitization atoms was calculated via the recorded number of CN 3 atoms deducting the initial number of dangling bonds atoms. This is akin to the research methodology that has previously been followed by Saurav Goel [252].

The graphitization conversion rate of the diamond tip is illustrated in Figure 7.26. The trend of the graphitization conversion rate of the diamond tip could be split into two regions during the course of nanomachining. The initially growing graphitization region implied that the initial rapid wear up to a cutting distance of 14 nm was more severe. Later stages of wear were somewhat steady. A similar trend of wear of diamond tool was found during the diamond turning of silicon [263] and silicon carbide [252] although the final rapid tool failure stage and final rapid wear stage did not reach in the MD simulation due to the short cutting distance. Therefore, this curve suggests that the continuous graphitization of diamond tip might lead to tool failure during nanometric cutting of GaAs.

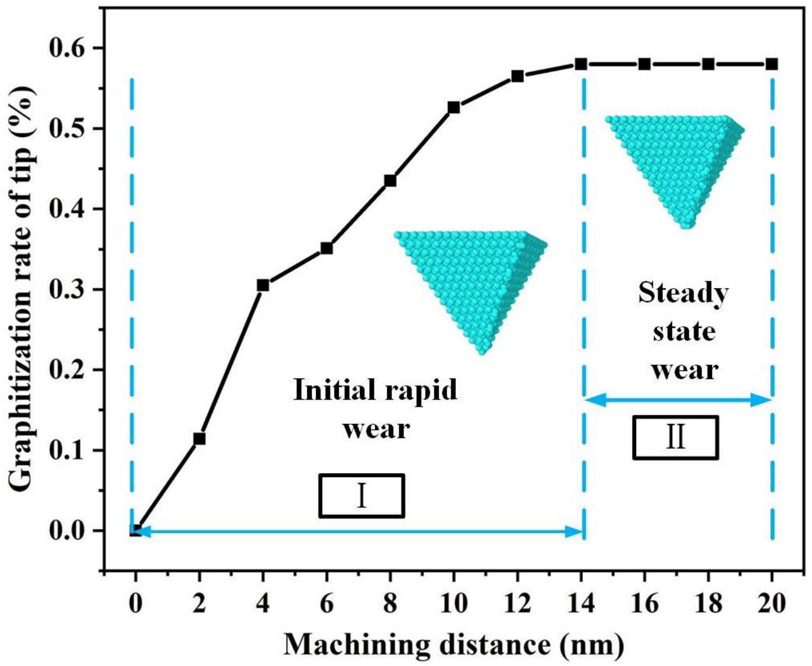

Figure 7.26 The graphitization conversion rate of diamond tip.s

7.7 Summary

In this chapter, the influence of the diamond tip alignment on the nanoscratching of single crystal GaAs was investigated by MD simulation, AFM nanoscratching experiments and was characterized by HRTEM. The results show the diamond tip alignment has a critical influence on the chip flow behavior, sidewall pileup morphology, and material removal state on the single crystal GaAs material surface. Additionally, a particular condition of oblique cutting with two cutting sides (OBCDS) taking part in cutting was observed to provide stronger stability to the AFM tip resulting in lesser sub-surface damage than oblique cutting with single side (OBCSS) and orthogonal cutting (ORC). OBCSS can create continuous belt-type chip without burrs. ORC has the fastest growing rate of cutting zone temperature. The TEM and DXA results show the sub-surface damage of single crystal GaAs during nanomachining process is attributed to the dual slip mechanisms i.e. shuffle-set slip mechanism (refer to the 1/2<110> dislocation in the {1 1 1} slip system) and glide-set slip mechanism (refer to the 1/6<112> dislocation in the {1 1 1} slip system), and the creation of dislocation loops, multi dislocation nodes, and dislocation junctions. Additionally, various stress states, such as hydrostatic stress, shear stress, and von Mises stress within the diamond tip and the temperature distribution of the diamond tip were also calculated in order to find out the underlying mechanism of graphitization. The results showed that the cutting heat during nanomachining of GaAs would mainly lead to the graphitization of the diamond tip instead of the high shear stress-induced transformation of the diamond to graphite. Finally, the graphitization conversion rate of diamond tip can be quantified in MD simulations.

Chapter 8 Hot Nanomachining of GaAs

8.1 Introduction

As we all know, the relative high nanoindentation hardness of 6.9 GPa, the elastic modulus of 103 GPa and low fracture toughness (K_{IC}=0.43 MPa $m^{1/2}$) results in poor room-temperature machinability of GaAs and makes it an even more challenging hard-to-machine material than Si [264][265] i.e. plasticity index (E/H) of silicon on the (100) orientation is 13.72 while that of GaAs is 14.92 and the brittleness index (H/K_{IC}) of silicon on the (100) orientation is 12.08 and that of GaAs is 16.27. It is well known that the hardness and yield strength of a hard, brittle material decreases at higher temperatures due to the reduced elastic recovery [266] whereas the fracture toughness increases with the increase of temperature [267]. This thesis, therefore, believes that the hot machining conditions can improve the machinability of GaAs. A major motivation behind this work is therefore to understand the salient aspects of the AFM tip-based hot machining of GaAs using MD simulations.

8.2 Cutting forces and temperatures during hot machining

The resultant cutting force was calculated by summing up the component forces between the diamond tip and GaAs substrate in LAMMPS. A comparison of the resultant force variation under the four conditions of cutting is shown in Figure 8.1 (a). It can be seen that the resultant forces experienced a sharp increase at the beginning of the cut until the onset of chip formation (where compression dominates) and thereafter the force become steady (where flow of chips becomes steady). The resultant force (which is square sum of the lateral and vertical forces) fluctuated between 100 and 150 nN. Furthermore, the magnitude of the resultant cutting force during the hot machining at 1200 K was 24% lower than that of room temperature nanomachining at 300 K. This noticeable reduction may be attributed to the thermal softening of the workpiece which increases its plasticity index (E/H) and this is consistent with other brittle materials like the single crystal 3C–SiC and silicon [158][159][160][162]. Contrary to a reduction observed in the resultant force, the friction coefficient (F_x/F_y) during hot machining went up in comparison to room temperature machining (see Figure 8.1 (b)). It is very interesting to see that the higher temperature of 1200 K led to a 7.83% increase in the friction coefficient compared to the room temperature machining at 300K. An increase in the value of friction coefficient for deep ploughing and until the critical temperature (ploughing friction) and a gradual drop in the grazing friction [268] has been ascribed to 'skating' through a local liquid cloud [269], and the linear response properties of the free substrate surface respectively.

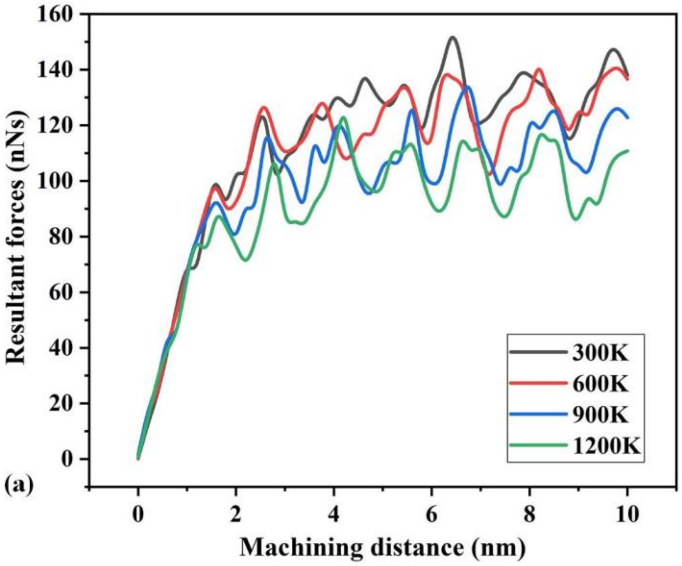

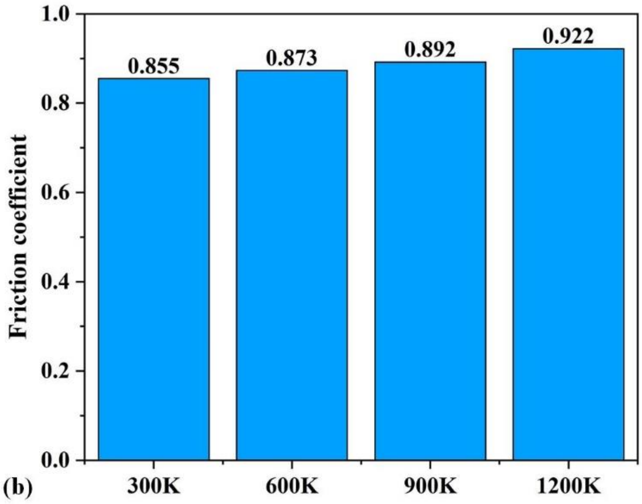

Figure 8.1 (a) Variations in the resultant cutting forces with the cutting distance. (b) Variation in the friction coefficient with the cutting temperature.

A comparison of the atomic temperature distribution during various cutting scenarios is illustrated in Figure 8.2. A relatively high temperature was observed near the apex of the diamond tip. One can see that the local temperature at the apex of the diamond tip reached a value of above 1000 K during hot machining of GaAs at 1200 K. Experimentally such a condition was observed to cause graphitization of diamond [261]. Therefore, the useful life of the diamond tip comes in a serious jeopardy during hot machining at extremely high temperatures. Moreover, the average temperature of cutting zone in the workpiece rises steadily with increasing cutting distance (see Figure 8.3).

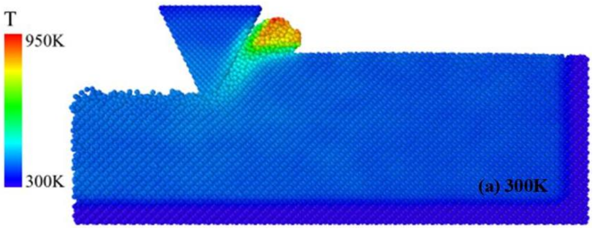

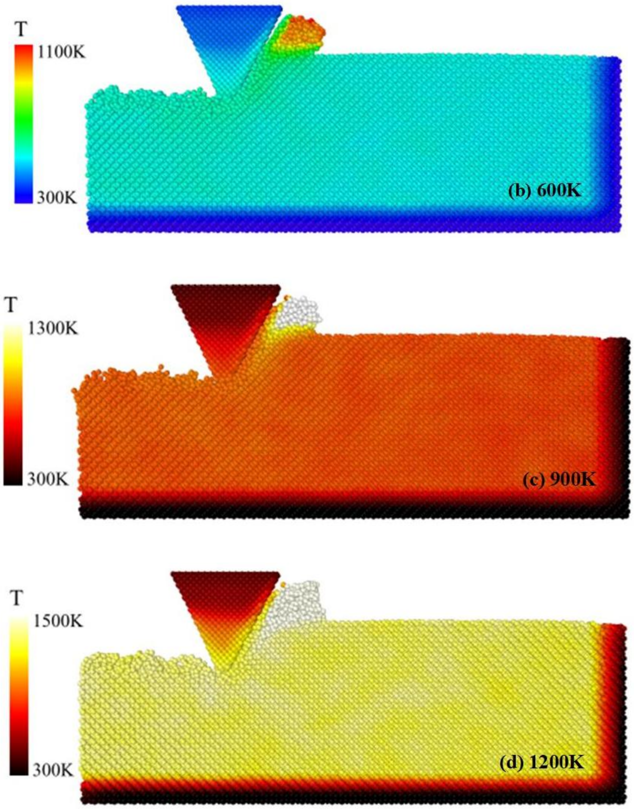

Figure 8.2 The temperature distribution at cutting distance of 10 nm under 300 K, 600 K, 900 K and 1200 K, respectively.

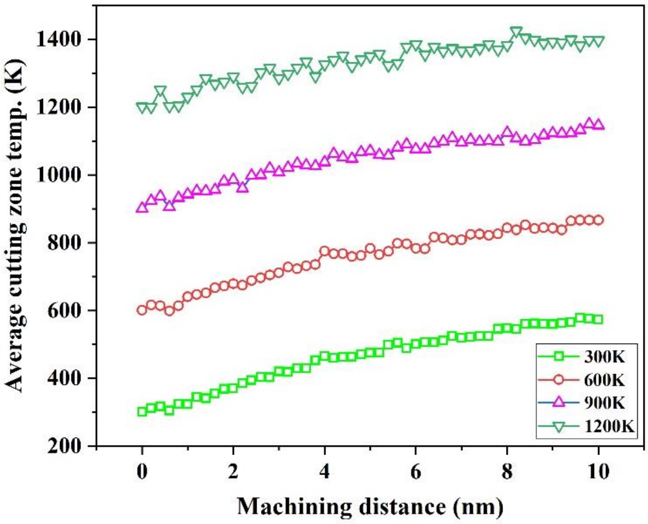

Figure 8.3 Variation in the cutting temperature in the cutting zone of the workpiece at different machining temperatures.

8.3 von Mises stress of diamond tip and atomic shear strain of cutting zone

As can be seen from Figure 8.4 (a), the magnitudes of the stress components, σ_{xx}, σ_{yy} and σ_{xy} acting on the diamond tip at 1200 K fluctuated between -3 GPa and -10 GPa, which suggests that the diamond tip undergoes compression. A similar evolution trend in the hydrostatic stress and von Mises stress was observed in Figure 8.4 (b). The magnitude of the hydrostatic stress and von Mises stress vary around -6 GPa and 9 GPa, respectively, which was approximately one fifth and one twentieth of that of acting on the diamond cutting tool for cutting silicon [141] and silicon carbide [267], respectively. The extremely low magnitude of stresses acted on the diamond tip is attributed to the lower cutting resistance of GaAs compared to silicon and silicon carbide. The von Mises stress distribution (see Figure 8.5) in the diamond tip shows that the higher the pre-heating temperature the smaller the portion of high von Mises stress in hot machining of GaAs.

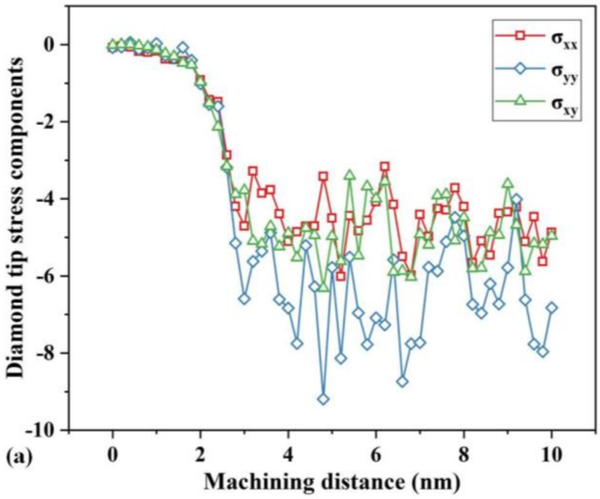

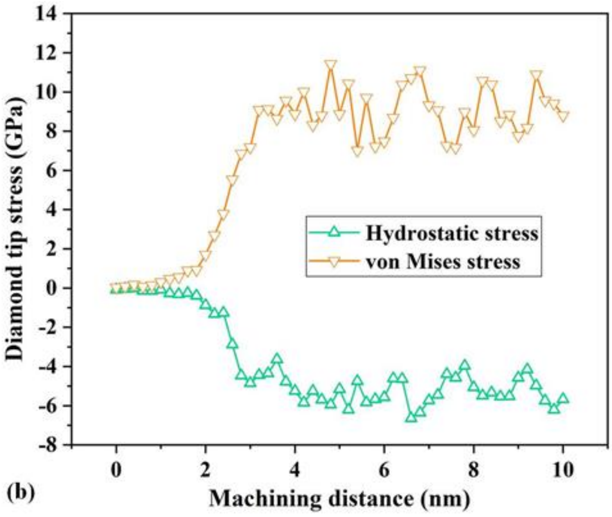

Figure 8.4 (a) Variations of stress components of the diamond tip at 1200 K. (b) Variations of hydrostatic stress and von Mises stress of the diamond tip at 1200 K.

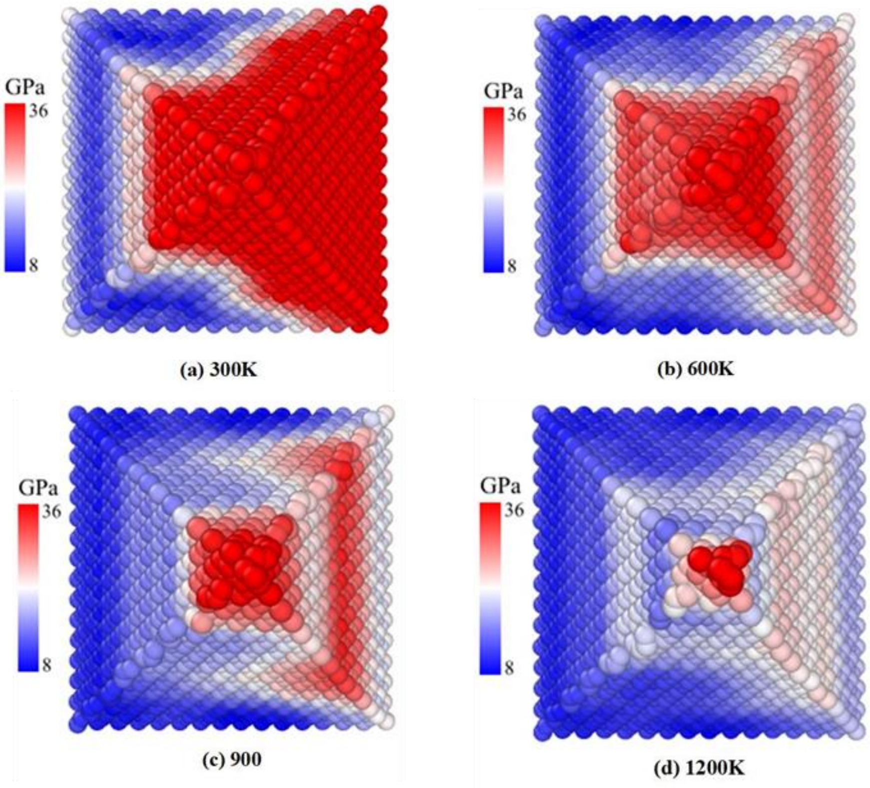

Figure 8.5 The von Mises stress distribution of the diamond tip at 300 K, 600 K, 900 K and 1200 K, respectively.

Next the research used atomic-level strain tensors before cutting (initial configuration) to compare the strain after cutting 10 nm (deformed configuration) GaAs [270][271]. The local atomic shear strain i.e. von Mises strain has been reported to describe well the local inelastic deformation [162][272]. The Green-Lagrangian strain tensor matrix η_i was derived from the local deformation gradient tensor matrix J_i and the initial gradient tensor matrix I. The local atomic shear strain was computed by below equations, in which η_{ij} represents the six gradient tensor components, and its distributions in two representative cases during cutting at 300K and at 1200K are shown in Figure 8.6.

$$\eta_i = \frac{1}{2}(J_i J_i^T - I) \tag{8-1}$$

$$\eta_i^{Mises} = \sqrt{\eta_{yz}^2 + \eta_{xz}^2 + \eta_{xy}^2 + \frac{(\eta_{yy}^2 - \eta_{zz}^2) + (\eta_{xx}^2 - \eta_{zz}^2) + (\eta_{xx}^2 - \eta_{yy}^2)}{6}} \tag{8-2}$$

It was observed that shear strain accumulates in the primary shear zone where the workpiece atoms experienced inelastic deformation and the magnitude of this strain decreases with the cutting temperature due to fact that the deformation is partially assisted by the thermal energy.

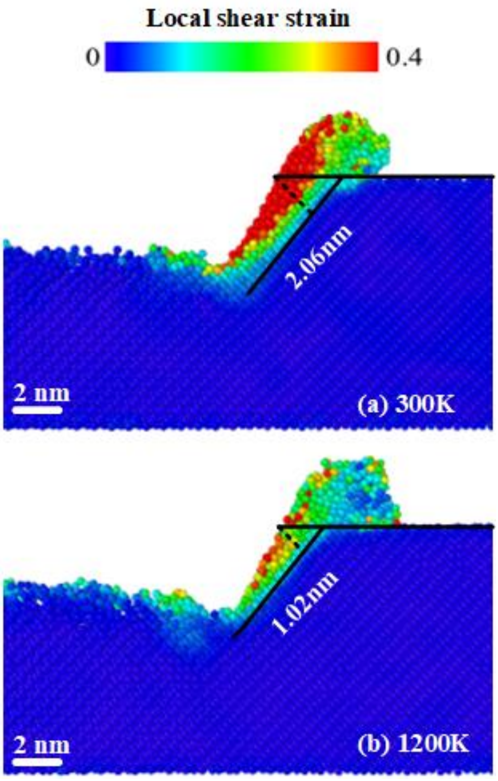

Figure 8.6 The local shear strain distribution of the cutting zone at 300 K and 1200 K, respectively.

8.4 Shear plane angle and sub-surface damage

The shear plane angle (as shown in Figure 8.7) represents the position of the primary shear zone relative to the horizontal plane and it was used to describe the machinability of the GaAs workpiece [184]. The shear plane angle was calculated by below equation.

$$\tan\theta = \frac{r\cos\alpha}{1-r\sin\alpha} \qquad (8\text{-}3)$$

where θ and α refers to the shear plane angle and rake angle of the diamond tip, respectively. The r is the chip ratio between uncut chip thickness and cut chip thickness. It was found that the shear plane angle reduced by approximately 4.33 degrees when cutting at 1200 K compared to 300 K. Further details may be seen from Table 8.1. The reduction of shear plane angle during hot machining suggests that the tangential cutting forces (F_x) become dominant over normal forces (F_y), which explains an improved cutting action and improved machinability of GaAs at high temperature.

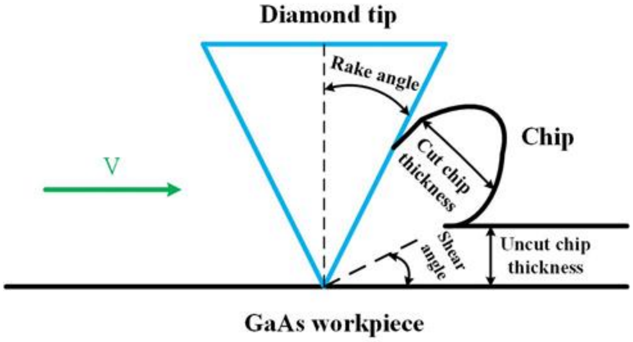

Figure 8.7 Schematic diagram of chip formation during AFM tip-based nanomachining of GaAs process.

Table 8.1 The comparison of shear plane angle for four different temperature cases.

Cases	**Nanoscratching temperature**	**Ratio of uncut chip thickness to cut chip thickness (r)**	**Shear plane angle (θ)**
1	300K	0.456	27.16 deg
2	600K	0.441	26.15 deg
3	900K	0.418	24.70 deg
4	1200K	0.389	22.83 deg

The research finally examines the extent of sub-surface damage at various cutting temperatures and these results are shown in Figure 8.8. It can be seen from Figure 8.8 (a)(b) that the depth of sub-surface damage in the machined surfaces increases with the increase of machining temperature, this is one of the drawbacks of hot machining. One of the reasons for seeing larger sub-surface damage is that hot cutting can weaken the interatomic bonding strength resulting in easier damage penetration and more widespread influence of even a low stress value [159]. This behavior was also observed during the cutting of silicon [161] and silicon carbide [159]. Furthermore, as shown in Figure 8.8 (c), the number of atoms in the cutting chip grew with the hotness of the workpiece and it suggests that the hot cutting chips are denser than the chips cut at lower temperature.

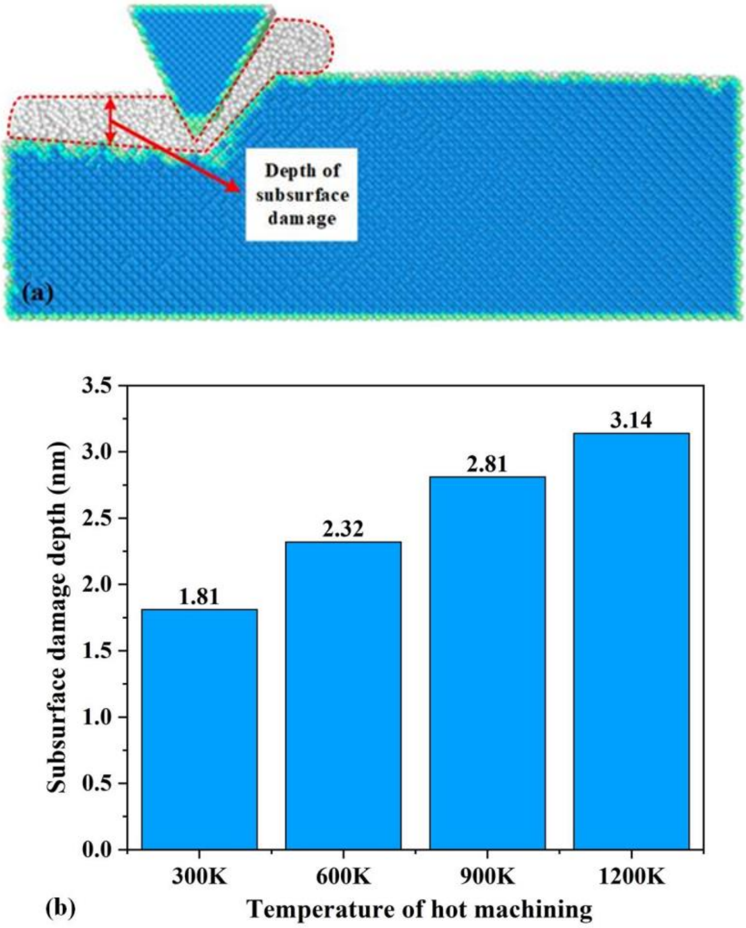

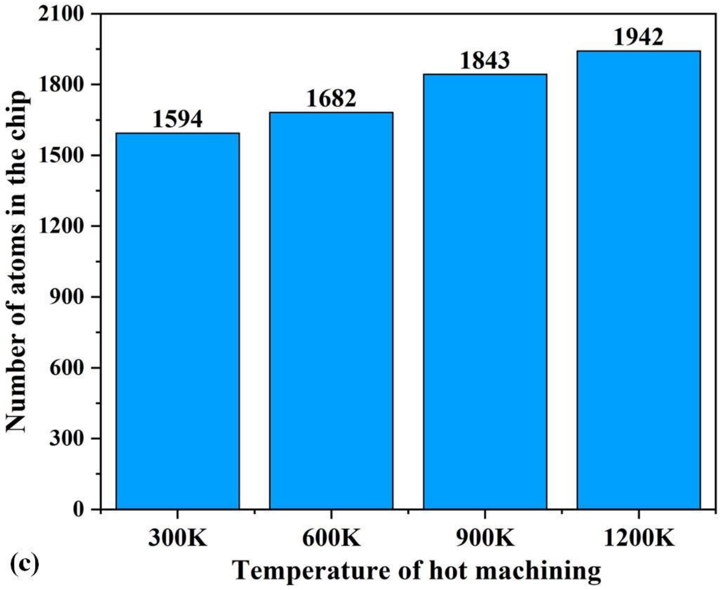

Figure 8.8 (a) Schematic diagram of the depth of sub-surface damage. (b) Variation in the sub-surface damage depth at different temperatures. (c) Evolution of the number of atoms in the cutting chips.

8.5 Summary

This chapter investigated the AFM tip-based hot cutting of single crystal GaAs at elevated temperature ranging from 300 K to 1200 K and benchmarked the cutting performance to its room temperature cutting using MD simulations. The results suggest hot machining approach can improve the machinability of hard-to-machine GaAs material through thermal softening but it causes an increase in the sub-surface damage than the room temperature cutting. Also, an increase in the machining temperature was found the accompany an increase in the friction coefficient. The rise of the GaAs substrate pre-heating temperature during hot machining resulted in reduced machining forces and thus a reduced cutting resistance which eases the material removal process. However, hot machining causes an increase in temperature at the apex of the tool tip and therefore, the diamond may graphitize during high temperature machining of GaAs. Additionally, the chip densification is observed under elevated cutting temperatures, in which the created cutting chip has more removal atoms than that of at room temperature. Finally, the shear plane angle reduces around 5° when the cutting performed at 1200 K in contrast to 300 K, which indicates the machinability of hard-to-machine GaAs material has been improved to some extent.

Chapter 9 Conclusions and Future Works

9.1 Conclusions

Gallium arsenide (GaAs) is one of the hard-brittle materials with desirable characteristics such as high-temperature resistance, large band-gap and higher electronic mobility making it superior to silicon as a second generation of semiconductor material. This PhD thesis investigated the atomic scale mechanics underpinning the nanomachining of GaAs through MD simulation and experimental studies. Chapter 4 and chapter 5 illustrated the difference between the single crystal and polycrystalline GaAs during SPDT process with experimental validation. Chapter 6 carried out MD simulations and AFM experiments to study the atomic scale friction. Chapter 7 included comparison results of orthogonal and oblique AFM nanoscratching of GaAs in both experiments and MD simulations. Also, it indicates the wear mechanism of diamond tip and formation mechanism of sub-surface damage during AFM-based nanomachining. Chapter 8 showed how the high temperature influences machinability of GaAs. This thesis addressed these knowledge gaps e.g. what is the incipient plasticity, how does the sub-surface damage form and how does the diamond cutting tool wear during nanomachining of GaAs and if the machinability of GaAs can be improved in thermally-assisted nanomachining. The main conclusions from the thesis can be summarised as follows:

1. Single crystal GaAs shows strong anisotropic machinability during SPDT. When cutting the (0 0 1) surface along the [1 1 0] direction, the simulated morphology shows more atoms pile-up on one side, compared to the other, while GaAs atoms are well-distributed on both sides when cutting the (1 1 1) surface along the [1 $\bar{1}$ 0] direction. With regards to cutting the (1 1 0) surface along the [0 0 1] direction,

almost all piled up GaAs atoms appeared on one side. The maximum friction coefficient is found when cutting the GaAs (0 0 1) surface along the [1 1 0] direction while cutting the (1 1 1) surface along the [1 $\bar{1}$ 0] direction possessed the minimum friction coefficient. The friction coefficient when cutting the (1 1 0) surface along the [0 0 1] direction is intermediate among these three typical crystalline orientations and cutting direction combinations.

2. The presence of grain boundaries eases the deformation of the polycrystalline GaAs as opposed to single crystal GaAs. It was discovered that the grain boundaries can become the incipient sites of dislocation nucleation and thus become the weak links in a polycrystal as opposed to a single crystal which has no such weaker links. The ease of plastic deformation of the grain boundaries compared to the individual grains makes polycrystals more easily deformed than the single crystals. The cutting forces showed a unique cyclic wave crest to wave troughs transition while cutting polycrystalline GaAs in contrast to the cutting of the single crystal GaAs. This was attributable to the periodic arrest of the dislocations in the grain boundaries followed by collapsed grain boundaries as a result of the continuous tool scratching.
3. The friction coefficient and the specific cutting energy were found to be higher for scratching single crystal GaAs than for polycrystalline GaAs and also the normal scratch force achieves a higher magnitude over the lateral scratch force once the scratching has achieved a steady state. Scratch forces and the sub-surface damage were observed to reduce with an increase in the scratch velocity and to increase with the increasing depth of scratch. However, the cutting temperature increases with the increase in scratch speed and the scratch depth. The 1/2<110>

was found to be the main type of dislocation responsible for incipient ductile plasticity in polycrystalline GaAs which splits into Shockley partials connected by an Internal Stacking Fault (ISF) leading to dissociation of the parent dislocation in 1/6<121> and 1/6<211> type dislocations.

4. It was found that while hot machining causes material’s thermal softening which improves material’s machinability evident from lower cutting stresses and cutting forces, the kinetic coefficient of friction between the tool and the workpiece increases with temperature which is in sharp contrast to the published literature.
5. It was surprisingly observed that the hot machining condition leads to an increased extent of sub-surface damage and there is also a trade-off with the use of cutting temperature as graphitization of diamond (even at low cutting stresses) can trigger by virtue of cutting temperature.
6. A new observation of chip densification is being reported for the first time i.e. the cutting chips obtained after machining at higher temperature were found to have more atoms than the chips obtained at lower cutting temperature and it showed a possibility of high density amorphization at higher cutting temperature.
7. A strong size effect was observed during nanoscraching at depths below 2 nm in the MD simulations and at depths below 15 nm in the AFM experiments. The tip sharpness used in the AFM was much higher than the one used in MD so it can be concluded that the size effect observed during nanoscratching is dependent on the geometry of the tip and the scratching depth. During steady-state scratching, when the scratching is performed in a size-effect-free regime, the value of the kinetic coefficient of friction revealed by the experiments and MD simulations was 0.55

and 0.62 respectively. In both cases, the value of the kinetic coefficient of friction increase to a value of unity when scratching is performed in the size-effect regime.

8. Likewise, a size effect was also observed in the specific scratch energy since the value obtained while scratching the (110) surface of GaAs was about 20 GPa in the size-effect free regime but it went upto 90 GPa at shallow scratch depths indicating a strong resistance from the workpiece to plastic deformation at narrower scratch depths. An interesting observation was that the specific scratch energy was seen to be insensitive to the scratch speed and geometry of the tip and good proximity was obtained between the MD simulations and experiments whereas the kinetic coefficient of friction showed some variations, albeit reasonably smaller variations. It was inferred that the specific scratch energy is a more reliable indicator over the friction coefficient to validate the simulation studies where differences in speed and geometry are involved.
9. The diamond tip alignment has a critical influence on the chip flow behavior, sidewall pileup morphology and material removal state on the single crystal GaAs material surface. A ploughing state is the responsibility for the plastic deformation of the single crystal GaAs material for oblique cutting with double sides and no chip formation. Conversely, the orthogonal cutting and oblique cutting with single side could form the chip. The burrs were observed for orthogonal cutting. However, belt-type chip formation of the oblique cutting with single side is smooth and continuous at the end of the nanogroove. The oblique cutting with double sides could lead to the highest magnitude of scratch force, coefficient of friction and specific cutting energy in the cutting zone while the oblique cutting with single side had the smallest magnitude. The orthogonal cutting was in the

intermediate. Furthermore, the oblique cutting with double sides was observed to provide stronger stability to the AFM tip resulting in lesser sub-surface damage with deeper machined depth.

10. Sub-surface damage of single crystal GaAs during nanomachining process was attributed to the dual slip mechanisms i.e. shuffle-set slip mechanism and glide-set slip mechanism, and the creation of dislocation loops, multi dislocation nodes, and dislocation junctions. Additionally, the incipient plasticity in single crystal GaAs during nanoscratching was subject to occurring due to the 1/2<110> type dislocation nucleated in the sub-surface of the GaAs.

9.2 Contributions to knowledge

The contributions to knowledge in this thesis can be listed as follows:

1. The fundamental reason of incipient plasticity during nanomachining of GaAs is the dislocation nucleation instead of phase transition. The 1/2<110> is the main type of dislocation responsible for incipient ductile plasticity in nanomachining of GaAs.
2. Dual slip mechanisms i.e. shuffle-set slip mechanism and glide-set slip mechanism, and dislocation loops, multi dislocation nodes, and dislocation junctions were discovered in sub-surface damage of nanomachining of GaAs process.
3. Graphitization was the dominant wear mechanism of the diamond tip during the nanometric cutting of single crystal GaAs. A new approach of quantifying the graphitization conversion rate of the diamond tip was proposed.

9.3 Recommendations for future works

This thesis provided an insight of mechanics of nanomachining of GaAs by employing (SPDT and AFM-based) nanomachining experiments and MD simulation. Material removal phenomenon, cutting forces, cutting temperature, flow stresses, anisotropic behaviour, tool wear and ductile plasticity deformation mechanism and sub-surface damage mechanism are studied. Such information supports the technological and scientific developments in the field of nanomachining of GaAs. However, the fact is MD simulation cannot break through its own limitations in time and special scales. The nanometric cutting model only has around hundreds of thousands of atomic scale for ~5 nm depth of cut. To this end, some future works are outlines as following:

1. A further scale up cutting model is required to carry out to reveal more insights in term of mesoscale MD simulation.
2. This thesis only performed on the nanoscratching process in all MD simulations. The nanoindentation of AFM tip-based model would be built up to further investigate the origin of ductile plasticity. The controversial issue on the reason to cause the incipient ductile plasticity governing by the dislocation nucleation or phase transition is required to justify.
3. In this thesis, all AFM tip-based nanomachining experiments were conducted under contact mode on the commercial AFM platform. The tapping mode, as a vibration assisted nanomachining method, would be employed to scratch GaAs. The comparison under contact mode and tapping mode nanoscratches experiments is required to further study in terms of sub-surface damage, cutting forces, and morphology of machined surface.

4. This thesis only established the diamond tip with constant rake angle. The fact is the rake angle of diamond cutting tool has significant influence on the tribological characteristics of nanomachining. Special edge geometry on the tool rake face can extend the tool life. What will be best geometry to prolong tool life? Multiscale cutting model is very useful to optimize the tool geometry (especially for diamond tool manufacturer) as diamond cutting experiment is costly. The optimization of rake angle of diamond tip is required with more MD simulation works.

Appendix A: Flow Stress Calculations

$$\textit{Stress tensor} = \begin{array}{ccc} \sigma_{xx} & \tau_{xy} & \tau_{xz} \\ \tau_{xy} & \sigma_{yy} & \tau_{yz} \\ \tau_{xz} & \tau_{xz} & \sigma_{zz} \end{array} \tag{1}$$

Invariants:

$$I_1 = \sigma_{xx} + \sigma_{yy} + \sigma_{zz} \tag{2}$$

$$I_2 = \sigma_{xx}\sigma_{yy} + \sigma_{yy}\sigma_{zz} + \sigma_{zz}\sigma_{xx} - {\tau_{xy}}^2 - {\tau_{xz}}^2 - {\tau_{yz}}^2 \tag{3}$$

$$I_3 = \sigma_{xx}\sigma_{yy}\sigma_{zz} + 2(\tau_{xy}\tau_{yz}\tau_{xz}) - {\tau_{xz}}^2\sigma_{yy} - {\tau_{yz}}^2\sigma_{xx} - {\tau_{xy}}^2\sigma_{zz} \tag{4}$$

$$A_1 = -I_1;\ A_2 = I_2;\ A_3 = -I_3; \tag{5}$$

$$Q = \frac{3A_2 - {A_1}^2}{9} \tag{6}$$

$$R = \frac{9A_1A_2 - 27A_3 - 2{A_1}^3}{54} \tag{7}$$

$$D = Q^3 + R^2 \tag{8}$$

If D<0 then as follows: else the condition is 2D stress

$$\theta = cos(\frac{R}{\sqrt{-Q^3}})^{-1} \tag{9}$$

$$R_1 = 2\sqrt{-Q} \times cos(\frac{\theta}{3}) - \frac{A_1}{3} \tag{10}$$

$$R_2 = 2\sqrt{-Q} \times cos(\frac{\theta + 4\pi}{3}) - \frac{A_1}{3} \tag{11}$$

$$R_3 = 2\sqrt{-Q} \times cos(\frac{\theta + 2\pi}{3}) - \frac{A_1}{3} \tag{12}$$

$$Major\ principal\ stress(\sigma_1) = max(R_1, R_2, R_3)\,; \tag{13}$$

$$Major\ principal\ stress(\sigma_3) = min(R_1, R_2, R_3)\,; \tag{14}$$

$$\sigma_{tresca} = \frac{\sigma_1 - \sigma_3}{2} \tag{15}$$

$$\sigma_{VON\ Mises} = \sqrt{\frac{(\sigma_{xx} - \sigma_{yy})^2 + (\sigma_{yy} - \sigma_{zz})^2 + (\sigma_{zz} - \sigma_{xx})^2 + 6({\tau_{xy}}^2 + {\tau_{yz}}^2 + {\tau_{xz}}^2)}{2}} \tag{16}$$

$$\sigma_{octahedral} = \sqrt{\frac{(\sigma_{xx}-\sigma_{yy})^2+(\sigma_{yy}-\sigma_{zz})^2+(\sigma_{zz}-\sigma_{xx})^2+6({\tau_{xy}}^2+{\tau_{yz}}^2+{\tau_{xz}}^2)}{2}} = \frac{\sqrt{2}}{3}\sigma_{VON\ Mises} \tag{17}$$

Appendix B: Bond-Order Potentials potential function parameters

Table B Bond-Order Potentials potential function parameters [273]

Symbol	Quantity	Ga-Ga	As-As	Ga-As
r_0	GSP reference radius (Å)	2.4235	2.1200	2.3800
r_c	GSP characteristic radius (Å)	2.4235	2.1200	2.3800
m	GSP attractive exponent	1.4509	1.3059	1.9652
n	GSP repulsive exponent	0.7255	0.6529	0.9826
n_c	GSP decay exponent	2.6234	2.6304	2.6234
r_l	Spline start radius (Å)	3.0000	3.0000	3.0000
r_{cut}	Spline cutoff radius (Å)	3.7000	3.6500	3.7000
φ_0	Repulsive energy prefactor (eV)	1.5520	3.9800	2.1000
$\beta_{\sigma,0}$	σ bond integral prefactor (eV)	1.5233	3.0877	1.7959
$\beta_{\pi,0}$	π bond integral prefactor (eV)	0.0975	0.9263	0.3233
c_σ	Empirical θ_σ parameter	1.5193	3.6016	0.8534
c_π	Empirical θ_π parameter	1.0000	1.0000	1.0000
f_σ	Band filling fraction ($e^-/8$)	0.4456	0.6558	0.5000
k_σ	Skewing prefactor	-25.6485	0.7600	0.0000

References

[1] S. K. Rao and R. Prasad, “Impact of 5G Technologies on Industry 4.0,” *Wirel. Pers. Commun.*, vol. 100, no. 1, pp. 145–159, 2018.

[2] A. Tăbuscă and S.-M. Tăbuscă, “Impact of 5G Technology in Global Economy. Cybersecurity and Legal Issues,” *J. Inf. Syst. Oper. Manag.*, vol. 13, no. 2, pp. 177–189, 2020.

[3] R. S. Nitesh, J. Rajendran, H. Ramiah, and A. Abd Manaf, “A 700MHz to 2.5GHz Cascode GaAs Power Amplifier for Multi-Band Pico-Cell Achieving 20dB Gain, 40dBm to 45dBm OIP3 and 66% Peak PAE,” *IEEE Access*, vol. 6, pp. 818–829, 2018.

[4] C. Chu and X. Liao, “One to 40 GHz ultra-wideband RF MEMS direct-contact switch based on GaAs MMIC technique,” *IET Microwaves, Antennas Propag.*, vol. 12, no. 6, pp. 879–884, 2018.

[5] H. Xie, Y. J. Cheng, and Y. Fan, “A K-Band High Interference-Rejection GaAs Low-Noise Amplifier Using Multizero Control Method for Satellite Communication,” *IEEE Microw. Wirel. Components Lett.*, vol. 30, no. 11, pp. 1–4, 2020.

[6] F. Z. Fang and Z. J. Yuan, “Ultra-precision cutting for gallium arsenide,” in *In Proc. ASPE Annual Meeting*, 1999, pp. 62–66.

[7] J. Chen, X. Luo, F. Ding, X. Rao, and J. Zhang, “Fundamental study of diamond turning of single crystal gallium arsenide,” *Precis. Eng.*, vol. 62, pp. 71–82, 2020.

[8] Y. H. Wu and L. Chang, “Chemical polishing method of GaAs specimens for transmission electron microscopy,” *Micron*, vol. 41, no. 1, pp. 20–25, 2010.

[9] K. Sasani, S. P. Abbasi, B. Sabrlouy Kolian, M. S. Zabihi, and J. Sabbaghzadeh, “Relationship between concentration, time and surface roughness of gaas wafer in lapping process: An experimental investigation,” in *2011 Symposium on Photonics and Optoelectronics, SOPO 2011*, 2011, pp. 1–4.

[10] S. G. Mcmeekin, M. Robertson, L. Mcgheeb, and J. M. Winfield, “Chemimechanical Polishing of Gallium Arsenide to Subnanometre Surface Finish,” *J. Mater. Chmistry*, vol. 2, no. 3, pp. 367–368, 1992.

[11] S. J. Prakash, R. Tyagi, and A. Gupta, “Backside thinning of GaAs wafer by lapping using DOE approach,” in *India International Conference on Power Electronics, IICPE 2010*, 2011, pp. 1–4.

[12] Y. Ma, G. Ballesteros, J. M. Zajac, J. Sun, and B. D. Gerardot, “Highly directional emission from a quantum emitter embedded in a hemispherical cavity,” *Opt. Lett.*, vol. 40, no. 10, p. 2373, 2015.

[13] T. Yu, D. Khatiwada, S. Sharma, M. D. Marquez, V. Selvamanickam, and T. R. Lee, “Microstructuring GaAs Using Reverse-Patterning Lithography: Implications for Transistors and Solar Cells,” *ACS Appl. Electron. Mater.*, vol. 3, no. 1, pp. 170–175, 2021.

[14] P. C. Kao *et al.*, “Fabrication of large-scaled organic light emitting devices on the flexible substrates using low-pressure imprinting lithography,” *IEEE Trans. Electron Devices*, vol. 52, no. 8, pp. 1722–1726, 2005.

[15] T. Kaehler, “Nanotechnology: Basic concepts and definitions,” *Clin. Chem.*, vol. 40, pp. 1797–1799, 1994.

[16] Y. Yan, Y. Geng, and Z. Hu, “Recent advances in AFM tip-based nanomechanical machining,” *Int. J. Mach. Tools Manuf.*, vol. 99, pp. 1–18, 2015.

[17] F. Fang *et al.*, “Towards atomic and close-to-atomic scale manufacturing,” *Int. J. Extrem. Manuf.*, vol. 1, no. 1, p. 012001, 2019.

[18] P. K. V. Babu and M. Radmacher, “Mechanics of brain tissues studied by atomic force microscopy: A perspective,” *Front. Neurosci.*, vol. 13, no. JUN, pp. 1–9, 2019.

[19] E. K. Antwi, K. Liu, and H. Wang, “A review on ductile mode cutting of brittle materials,” *Front. Mech. Eng.*, vol. 13, no. 2, pp. 251–263, 2018.

[20] V. C. Venkatesh, I. Inasaki, H. K. Toenshof, T. Nakagawa, and I. D. Marinescu, “Observations on Polishing and Ultraprecision Machining of Semiconductor Substrate Materials,” *CIRP Ann. - Manuf. Technol.*, vol. 44, no. 2, pp. 611–618, 1995.

[21] Y. Ma, G. Ballesteros, J. M. Zajac, J. Sun, and B. D. Gerardot, “Highly directional emission from a quantum emitter embedded in a hemispherical cavity,” *Opt. Lett.*, vol. 40, no. 10, p. 2373, 2015.

[22] C. K. Hyon, S. C. Choi, S. W. Hwang, D. Ahn, Y. Kim, and E. K. Kim, “Direct nanometer-scale patterning by the cantilever oscillation of an atomic force microscope,” *Appl. Phys. Lett.*, vol. 75, no. 2, pp. 292–294, 1999.

[23] W. S. Blackley and R. O. Scattergood, “Ductile-regime machining model for diamond turning of brittle materials,” *Precis. Eng.*, vol. 13, no. 2, pp. 95–103, 1991.

[24] S. Wang and P. Pirouz, “Mechanical properties of undoped GaAs. II: The brittle-to-ductile transition temperature,” *Acta Mater.*, vol. 55, no. 16, pp. 5515–5525, 2007.

[25] E. Binnig, G., Rohrer, H., Gerber, C. & Weibel, “Surface studies by scanning tunneling microscopy,” *Phys. Rev. Lett.*, vol. 49, no. 1, pp. 57–61, 1982.

[26] E. DM and S. EK, “Positioning single atoms with scanning tunnelling microscope,” *Nature*, vol. 344, no. April, p. 524, 1990.

[27] T. A. Jung *et al.*, “The atomic force microscope used as a powerful tool for machining surfaces,” *Ultramicroscopy*, vol. 42–44, no. PART 2, pp. 1446–1451, 1992.

[28] S. Tegen, B. Kracke, and B. Damaschke, “Surface modifications with a scanning force microscope,” *Rev. Sci. Instrum.*, vol. 68, no. 3, pp. 1458–1460, 1997.

[29] J. M. R. Weaver, “High resolution atomic force microscopy potentiometry,” *J. Vac. Sci. Technol. B Microelectron. Nanom. Struct.*, vol. 9, no. 3, p. 1559, 1991.

[30] U. Hartmann, “Magnetic force microscopy: Some remarks from the micromagnetic point of view,” *J. Appl. Phys.*, vol. 64, no. 3, pp. 1561–1564, 1988.

[31] A. Meister *et al.*, “FluidFM: Combining atomic force microscopy and nanofluidics in a universal liquid delivery system for single cell applications and beyond,” *Nano Lett.*, vol. 9, no. 6, pp. 2501–2507, 2009.

[32] A. Roelofs, U. Böttger, R. Waser, F. Schlaphof, S. Trogisch, and L. M. Eng, “Differentiating 180° and 90° switching of ferroelectric domains with three-

dimensional piezoresponse force microscopy," *Appl. Phys. Lett.*, vol. 77, no. 21, pp. 3444–3446, 2000.

[33] "https://blog.brukerafmprobes.com/." .

[34] M. Ternes, C. P. Lutz, C. F. Hirjibehedin, F. J. Giessibl, and A. J. Heinrich, "The Force Needed to Move an Atom on a Surface," *Science (80-.).*, vol. 1066, no. 111, pp. 1066–1070, 2008.

[35] G. Binnig, "In Touch with Atoms," *Rev. Mod. Phys.*, vol. 71, no. 2, pp. 324–330, 1999.

[36] J. Repp, G. Meyer, and F. E. Olsson, "Controlling the Charge State of individual Gold Adatoms," *Science (80-.).*, vol. 305, no. July, pp. 493–495, 2004.

[37] S. Y. Quek *et al.*, "Mechanically controlled binary conductance switching of a single-molecule junction," *Nat. Nanotechnol.*, vol. 4, no. 4, pp. 230–234, 2009.

[38] S. Fölsch, J. Martínez-Blanco, J. Yang, K. Kanisawa, and S. C. Erwin, "Quantum dots with single-atom precision," *Nat. Nanotechnol.*, vol. 9, no. 7, pp. 505–508, 2014.

[39] C. F. Hirjibehedin *et al.*, "Large Magnetic Anisotropy of a Single Atomic Spin Embedded in a Surface Molecular Network," *Science (80-.).*, vol. 317, no. August, pp. 1199–1203, 2007.

[40] S. Kawai, A. S. Foster, F. F. Canova, H. Onodera, S. I. Kitamura, and E. Meyer, "Atom manipulation on an insulating surface at room temperature," *Nat. Commun.*, vol. 5, pp. 1–7, 2014.

[41] Y. Sugimoto, M. Abe, S. Hirayama, N. Oyabu, O. Custance, and S. Morita, "Atom inlays performed at room temperature using atomic force microscopy," *Nat. Mater.*, vol. 4, no. 2, pp. 156–159, 2005.

[42] M. Rashidi *et al.*, "Initiating and Monitoring the Evolution of Single Electrons Within Atom-Defined Structures," *Phys. Rev. Lett.*, vol. 121, no. 16, p. 166801, 2018.

[43] J. a Dagata, "Device Fabrication by Scanned robe Oxidation cessing by wet dry a chemical is Small RNA Chaperones for Ribosome Biogenesis," *Science (80-.).*, vol. 270, no. December, pp. 1625–1627, 1995.

[44] T. Cramer, F. Zerbetto, and R. García, "Molecular mechanism of water bridge buildup: Field-induced formation of nanoscale menisci," *Langmuir*, vol. 24, no. 12, pp. 6116–6120, 2008.

[45] R. Garcia, R. V. Martinez, and J. Martinez, "Nano-chemistry and scanning probe nanolithographies," *Chem. Soc. Rev.*, vol. 35, no. 1, pp. 29–38, 2006.

[46] Y. K. Ryu and R. Garcia, "Advanced oxidation scanning probe lithography," *Nanotechnology*, vol. 28, no. 14, 2017.

[47] J. Germain, M. Rolandi, S. A. Backer, and J. M. J. Fréchet, "Sulfur as a novel nanopatterning material: An ultrathin resist and a chemically addressable template for nanocrystal self-assembly," *Adv. Mater.*, vol. 20, no. 23, pp. 4526–4529, 2008.

[48] L. Weng, L. Zhang, Y. P. Chen, and L. P. Rokhinson, "Atomic force microscope local oxidation nanolithography of graphene," *Appl. Phys. Lett.*, vol. 93, no. 9, pp. 1–4, 2008.

[49] J. Martinez, R. V. Martínez, and R. Garcia, “Silicon nanowire transistors with a channel width of 4 nm fabricated by atomic force microscope nanolithography,” *Nano Lett.*, vol. 8, no. 11, pp. 3636–3639, 2008.

[50] H. Li *et al.*, “Electrode-Free Anodic Oxidation Nanolithography of Low-Dimensional Materials,” *Nano Lett.*, vol. 18, no. 12, pp. 8011–8015, 2018.

[51] R. V. Martínez, J. Martínez, and R. Garcia, “Silicon nanowire circuits fabricated by AFM oxidation nanolithography,” *Nanotechnology*, vol. 21, no. 24, 2010.

[52] F. M. Espinosa, Y. K. Ryu, K. Marinov, D. Dumcenco, A. Kis, and R. Garcia, “Direct fabrication of thin layer MoS2field-effect nanoscale transistors by oxidation scanning probe lithography,” *Appl. Phys. Lett.*, vol. 106, no. 10, pp. 1–5, 2015.

[53] S. Bertolazzi, D. Krasnozhon, and A. Kis, “Nonvolatile memory cells based on MoS2/graphene heterostructures,” *ACS Nano*, vol. 7, no. 4, pp. 3246–3252, 2013.

[54] L. Wang, Y. Wang, J. I. Wong, T. Palacios, J. Kong, and H. Y. Yang, “Functionalized MoS2nanosheet-based field-effect biosensor for label-free sensitive detection of cancer marker proteins in solution,” *Small*, vol. 10, no. 6, pp. 1101–1105, 2014.

[55] A. I. Dago, Y. K. Ryu, and R. Garcia, “Sub-20 nm patterning of thin layer WSe2 by scanning probe lithography,” *Appl. Phys. Lett.*, vol. 109, no. 16, 2016.

[56] M. Lorenzoni and B. Torre, “Scanning probe oxidation of SiC, fabrication possibilities and kinetics considerations,” *Appl. Phys. Lett.*, vol. 103, no. 16, 2013.

[57] M. Cavallini *et al.*, “Additive nanoscale embedding of functional nanoparticles on silicon surface,” *Nanoscale*, vol. 2, no. 10, pp. 2069–2072, 2010.

[58] H. J. Mamin and D. Rugar, “Thermomechanical writing with an atomic force microscope tip,” *Appl. Phys. Lett.*, vol. 61, no. 8, pp. 1003–1005, 1992.

[59] D. Wang *et al.*, “Direct writing and characterization of poly(p -phenylene vinylene) nanostructures,” *Appl. Phys. Lett.*, vol. 95, no. 23, pp. 93–96, 2009.

[60] J. Lee, T. Beechem, T. L. Wright, B. A. Nelson, S. Graham, and W. P. King, “Electrical, thermal, and mechanical characterization of silicon microcantilever heaters,” *J. Microelectromechanical Syst.*, vol. 15, no. 6, pp. 1644–1655, 2006.

[61] J. Lee *et al.*, “Thermal conduction from microcantilever heaters in partial vacuum,” *J. Appl. Phys.*, vol. 101, no. 1, 2007.

[62] B. Lee, C. B. Prater, and W. P. King, “Lorentz force actuation of a heated atomic force microscope cantilever,” *Nanotechnology*, vol. 23, no. 5, 2012.

[63] R. Garcia, A. W. Knoll, and E. Riedo, “Advanced scanning probe lithography,” *Nat. Nanotechnol.*, vol. 9, no. 8, pp. 577–587, 2014.

[64] W. Ketterle *et al.*, “Nanoscale Three-Dimensional Patterning of Molecular Resists by Scanning Probes,” *Science (80-.).*, vol. 5, no. May, pp. 732–736, 2010.

[65] J. E. Shaw, P. N. Stavrinou, and T. D. Anthopoulos, “On-demand patterning of nanostructured pentacene transistors by scanning thermal lithography,” *Adv. Mater.*, vol. 25, no. 4, pp. 552–558, 2013.

[66] W. K. Lee *et al.*, “Chemically isolated graphene nanoribbons reversibly formed in fluorographene using polymer nanowire masks,” *Nano Lett.*, vol. 11, no. 12, pp. 5461–5464, 2011.

[67] X. Liu, S. T. Howell, A. Conde-Rubio, G. Boero, and J. Brugger, “Thermomechanical Nanocutting of 2D Materials,” *Adv. Mater.*, vol. 32, no. 31, 2020.

[68] Y. Wei, P. Liu, F. Zhu, K. Jiang, Q. Li, and S. Fan, “Efficient fabrication of carbon nanotube micro tip arrays by tailoring cross-stacked carbon nanotube sheets,” *Nano Lett.*, vol. 12, no. 4, pp. 2071–2076, 2012.

[69] S. T. Zimmermann, D. W. R. Balkenende, A. Lavrenova, C. Weder, and J. Brugger, “Nanopatterning of a Stimuli-Responsive Fluorescent Supramolecular Polymer by Thermal Scanning Probe Lithography,” *ACS Appl. Mater. Interfaces*, vol. 9, no. 47, pp. 41454–41461, 2017.

[70] H. J. Mamin, “Thermal writing using a heated atomic force microscope tip,” *Appl. Phys. Lett.*, vol. 69, no. 3, pp. 433–435, 1996.

[71] B. Gotsmann and U. Dürig, “Thermally Activated Nanowear Modes of a Polymer Surface Induced by a Heated Tip,” *Langmuir*, vol. 20, no. 4, pp. 1495–1500, 2004.

[72] R. A. Griffiths, A. Williams, I. Servin, and R. Tiron, “Corrigendum : Thermal scanning probe lithography for the directed self- assembly of block copolymers,” *Nanotechnology*, vol. 28, pp. 1–9, 2017.

[73] H. J. Kim *et al.*, “Ultrananocrystalline diamond tip integrated onto a heated atomic force microscope cantilever,” *Nanotechnology*, vol. 23, no. 49, pp. 0–9, 2012.

[74] Y. K. Ryu Cho *et al.*, “Sub-10 Nanometer Feature Size in Silicon Using Thermal Scanning Probe Lithography,” *ACS Nano*, vol. 11, no. 12, pp. 11890–11897, 2017.

[75] L. L. Cheong *et al.*, “Thermal probe maskless lithography for 27.5 nm half-pitch Si technology,” *Nano Lett.*, vol. 13, no. 9, pp. 4485–4491, 2013.

[76] C. Rawlings *et al.*, “Fast turnaround fabrication of silicon point-contact quantum-dot transistors using combined thermal scanning probe lithography and laser writing,” *Nanotechnology*, vol. 29, no. 50, 2018.

[77] H. Hu, Y. Zhuo, M. E. Oruc, B. T. Cunningham, and W. P. King, “Nanofluidic channels of arbitrary shapes fabricated by tip-based nanofabrication,” *Nanotechnology*, vol. 25, no. 45, 2014.

[78] M. Id *et al.*, “High-Speed Scanning Thermal Lithography for Nanostructuring of Electronic Devices Nanoscale Graphical and Textual Abstract A high-speed nanopatterning method is developed for the rapid prototyping of nanostructured active and passive components as well as,” *Nanoscale*, pp. 1–26, 2014.

[79] A. D. Ellington and J. W. Szostak, “Light-emiting diodes based on conjugated polymers,” *Nature*, vol. 346, pp. 818–822, 1990.

[80] O. Fenwick *et al.*, “Thermochemical nanopatterning of organic semiconductors,” *Nat. Nanotechnol.*, vol. 4, no. 10, pp. 664–668, 2009.

[81] P. Vettiger *et al.*, “The ‘millipede’-nanotechnology entering data storage,” *IEEE Trans. Nanotechnol.*, vol. 1, no. 1, pp. 39–54, 2002.

[82] J. H. Lim and C. A. Mirkin, “Electrostatically driven Dip-pen nanolithography of conducting polymers,” *Adv. Mater.*, vol. 14, no. 20, pp. 1474–1477, 2002.

[83] B. W. Maynor, S. F. Filocamo, M. W. Grinstaff, and J. Liu, “Direct-writing of polymer nanostructures: Poly(thiophene) nanowires on semiconducting and insulating surfaces,” *J. Am. Chem. Soc.*, vol. 124, no. 4, pp. 522–523, 2002.

[84] D. S. Ginger, H. Zhang, and C. A. Mirkin, “The Evolution of Dip-Pen Nanolithography,” *Angew. Chemie - Int. Ed.*, vol. 43, no. 1, pp. 30–45, 2004.

[85] X. Zhou, S. He, K. A. Brown, J. Mendez-Arroyo, F. Boey, and C. A. Mirkin, “Locally altering the electronic properties of graphene by nanoscopically doping it with rhodamine 6G,” *Nano Lett.*, vol. 13, no. 4, pp. 1616–1621, 2013.

[86] J. Zhao *et al.*, “Three-Dimensional Nanoprinting via Scanning Probe Lithography-Delivered Layer-by-Layer Deposition,” *ACS Nano*, vol. 10, no. 6, pp. 5656–5662, 2016.

[87] E. Bellido, R. De Miguel, J. Sesé, D. Ruiz-Molina, A. Lostao, and D. Maspoch, “Nanoscale positioning of inorganic nanoparticles using biological ferritin arrays fabricated by Dip-Pen Nanolithography,” *Scanning*, vol. 32, no. 1, pp. 35–41, 2010.

[88] Ki-Bum Lee1, So-Jung Park1, * Chad A. Mirkin1, Jennifer C. Smith2, and * Milan Mrksich2, “Protein Nanoarrays Generated By Dip-Pen Nanolithography,” *Science (80-.).*, vol. 295, no. 5560, pp. 1702–1705, 2002.

[89] I. Kuljanishvili, D. A. Dikin, S. Rozhok, S. Mayle, and V. Chandrasekhar, “Controllable patterning and CVD growth of isolated carbon nanotubes with direct parallel writing of catalyst using dip-pen Nanolithography,” *Small*, vol. 5, no. 22, pp. 2523–2527, 2009.

[90] C. M. Jewell and D. M. Lynn, “Multilayered polyelectrolyte assemblies as platforms for the delivery of DNA and other nucleic acid-based therapeutics,” *Adv. Drug Deliv. Rev.*, vol. 60, no. 9, pp. 979–999, 2008.

[91] C. Wu, D. N. Reinhoudt, C. Otto, A. H. Velders, and V. Subramaniam, “Protein Immobilization on Ni (II) Ion Patterns Prepared by Microcontact Printing and Dip-Pen Nanolithography,” *ACS Nano*, vol. 4, no. 2, pp. 1083–1091, 2010.

[92] K. Salaita, Y. Wang, and C. A. Mirkin, “Applications of dip-pen nanolithography,” *Nat. Nanotechnol.*, vol. 2, no. 3, pp. 145–155, 2007.

[93] M. Gabi *et al.*, “FluidFM: Combining Atomic Force Microscopy and Nanofuidics in a Universal Liquid Delivery System for Single Cell Applications and Beyond,” *Nano Lett.*, vol. 9, no. 6, pp. 2501–7, 2009.

[94] J. Zhong, G. Sun, and D. He, “Classic, liquid, and matrix-assisted dip-pen nanolithography for materials research,” *Nanoscale*, vol. 6, no. 21, pp. 12217–12228, 2014.

[95] S. C. Hung, O. A. Nafday, J. R. Haaheim, F. Ren, G. C. Chi, and S. J. Pearton, “Dip pen nanolithography of conductive silver traces,” *J. Phys. Chem. C*, vol. 114, no. 21, pp. 9672–9677, 2010.

[96] J. L. H. Peng-Cheng Chen, Xiaolong Liu, “Polyelemental nanoparticle libraries,” *Science (80-.).*, vol. 352, no. 6293, pp. 0–5, 2016.

[97] B. A. Nelson, W. P. King, A. R. Laracuente, P. E. Sheehan, and L. J. Whitman, “Direct deposition of continuous metal nanostructures by thermal dip-pen nanolithography,” *Appl. Phys. Lett.*, vol. 88, no. 3, pp. 1–3, 2006.

[98] W. K. Lee, Z. Dai, W. P. King, and P. E. Sheehan, “Maskless nanoscale writing of nanoparticle-polymer composites and nanoparticle assemblies using thermal nanoprobes,” *Nano Letters*, vol. 10, no. 1. pp. 129–133, 2010.

[99] S. Hong and C. A. Mirkin, “A nanoplotter with both parallel and serial writing capabilities,” *Science (80-.).*, vol. 288, no. 5472, pp. 1808–1811, 2000.

[100] Q. He, C. Tan, and H. Zhang, “Recent Advances in Cantilever-Free Scanning Probe Lithography: High-Throughput, Space-Confined Synthesis of Nanostructures and beyond,” *ACS Nano*, vol. 11, no. 5, pp. 4381–4386, 2017.

[101] W. M. Wang, R. M. Stoltenberg, S. Liu, and Z. Bao, “Direct Patterning of Gold Nanoparticles,” *Am. Chem. Soc. Nano*, vol. 2, no. 10, pp. 2135–2142, 2008.

[102] S. F. Lyuksyutov *et al.*, “Electrostatic nanolithography in polymers using atomic force microscopy,” *Nat. Mater.*, vol. 2, no. 7, pp. 468–472, 2003.

[103] M. Kaestner *et al.*, “Electric field scanning probe lithography on molecular glass resists using self-actuating, self-sensing cantilever,” *Proc. SPIE*, vol. 9049, no. July 2016, pp. 90490C–1, 2014.

[104] T. Thurn-albrecht and T. P. Russell, “Electrically induced structure formation and pattern transfer,” *Nature*, vol. 403, no. February, pp. 1998–2001, 2000.

[105] P. T. Mathew and F. Fang, “Advances in Molecular Electronics: A Brief Review,” *Engineering*, vol. 4, no. 6, pp. 760–771, 2018.

[106] J. M. Tour, J. Chen, M. A. Reed, and A. M. Rawlett, “Large On-Off Ratios and Negative Differential Resistance in a Molecular Electronic Device,” *Science (80-.).*, vol. 286, pp. 1550–1552, 1999.

[107] S. C. Esener, M. H. Kryder, W. D. Doyle, and D. A. Thompson, “The Future of Data Storage Technologies,” *WTEC*, no. June, pp. 48–62, 1999.

[108] J. Guo *et al.*, “Real-space imaging of interfacial water with submolecular resolution,” *Nat. Mater.*, vol. 13, no. 2, pp. 184–189, 2014.

[109] J. Guo, X. Z. Li, J. Peng, E. G. Wang, and Y. Jiang, “Atomic-scale investigation of nuclear quantum effects of surface water: Experiments and theory,” *Prog. Surf. Sci.*, vol. 92, no. 4, pp. 203–239, 2017.

[110] U. F. Keyser, H. W. Schumacher, U. Zeitler, R. J. Haug, and K. Eberl, “Fabrication of a single-electron transistor by current-controlled local oxidation of a two-dimensional electron system,” *Appl. Phys. Lett.*, vol. 76, no. 4, pp. 457–459, 2000.

[111] I. Suez, S. A. Backer, and J. M. J. Fréchet, “Generating an etch resistant ‘resist’ layer from common solvents using scanning probe lithography in a fluid cell,” *Nano Lett.*, vol. 5, no. 2, pp. 321–324, 2005.

[112] R. V. Martínez, N. S. Losilla, J. Martínez, Y. Huttel, and R. Garcia, “Patterning polymeric structures with 2 nm resolution at 3 nm half pitch in ambient conditions,” *Nano Lett.*, vol. 7, no. 7, pp. 1846–1850, 2007.

[113] Z. B. Wang, N. Joseph, L. Li, and B. S. Luk’Yanchuk, “A review of optical near-fields in particle/tip-assisted laser nanofabrication,” *Proc. Inst. Mech. Eng. Part C J. Mech. Eng. Sci.*, vol. 224, no. 5, pp. 1113–1127, 2010.

[114] R. Garcia *et al.*, “Nanopatterning of carbonaceous structures by field-induced carbon dioxide splitting with a force microscope,” *Appl. Phys. Lett.*, vol. 96, no. 14, pp. 2008–2011, 2010.

[115] S. DONG, “Nontraditional manufacturing technique-Nano machining technique based on SPM,” *Sci. China Ser. G*, vol. 47, no. 7, p. 51, 2004.

[116] G. Xiao, Y. He, Y. Geng, Y. Yan, and M. Ren, “Molecular dynamics and experimental study on comparison between static and dynamic ploughing lithography of single crystal copper,” *Appl. Surf. Sci.*, vol. 463, no. August 2018, pp. 96–104, 2019.

[117] Y. Da Yan, S. Dong, and T. Sun, “Investigation on Influencing Factors of AFM Micro Probe Nanomachining,” in *Advances in Materials Manufacturing Science and Technology*, 2004, vol. 471, pp. 816–820.

[118] M. Wendel, S. Kühn, H. Lorenz, J. P. Kotthaus, and M. Holland, “Nanolithography with an atomic force microscope for integrated fabrication of quantum electronic devices,” *Appl. Phys. Lett.*, vol. 65, no. 14, pp. 1775–1777, 1994.

[119] H. W. Schumacher, U. F. Keyser, U. Zeitler, R. J. Haug, and K. Eberl, “Nanomachining of mesoscopic electronic devices using an atomic force microscope,” *Appl. Phys. Lett.*, vol. 75, no. 8, pp. 1107–1109, 1999.

[120] V. Bouchiat and D. Esteve, “Lift-off lithography using an atomic force microscope,” *Appl. Phys. Lett.*, vol. 69, no. 20, pp. 3098–3100, 1996.

[121] J.-M. Lee, W.-H. Jin, and D.-E. Kim, “Application of single asperity abrasion process for surface micro-machining,” *Wear*, vol. 251, no. 1–12, pp. 1133–1143, 2001.

[122] J. M. Lee, I. H. Sung, and D. E. Kim, “Process development of precision surface micro-machining using mechanical abrasion and chemical etching,” *Microsyst. Technol.*, vol. 8, no. 6, pp. 419–426, 2002.

[123] Y. Yan, T. Sun, Y. Liang, and S. Dong, “Investigation on AFM-based micro/nano-CNC machining system,” *Int. J. Mach. Tools Manuf.*, vol. 47, no. 11, pp. 1651–1659, 2007.

[124] Y. Yan, Z. Hu, X. Zhao, T. Sun, S. Dong, and X. Li, “Top-down nanomechanical machining of three-dimensional nanostructures by atomic force microscopy,” *Small*, vol. 6, no. 6, pp. 724–728, 2010.

[125] Y. T. Mao *et al.*, “Research on three dimensional machining effects using atomic force microscope,” *Rev. Sci. Instrum.*, vol. 80, no. 6, 2009.

[126] Y. Sun, Y. Yan, Z. Hu, X. Zhao, and J. Yan, “3D polymer nanostructures fabrication by AFM tip-based single scanning with a harder cantilever,” *Tribol. Int.*, vol. 47, pp. 44–49, 2012.

[127] Y. He, Y. Yan, Y. Geng, and Z. Hu, “Fabrication of none-ridge nanogrooves with large-radius probe on PMMA thin-film using AFM tip-based dynamic plowing lithography approach,” *J. Manuf. Process.*, vol. 29, pp. 204–210, 2017.

[128] Y. He, Y. Yan, Y. Geng, and E. Brousseau, “Fabrication of periodic nanostructures using dynamic plowing lithography with the tip of an atomic force microscope,” *Appl. Surf. Sci.*, vol. 427, pp. 1076–1083, 2018.

[129] C. T. and R. G. Borislav Vasić1, Markus Kratzer2, Aleksandar Matković1, Andreas Nevosad2, Uroš Ralević1, Djordje Jovanović1, Christian Ganser2,3,

"Atomic force microscopy based manipulation of graphene using dynamic plowing lithography," *Nanotechnology*, vol. 24, 2013.

[130] Y. Yan, Y. He, G. Xiao, Y. Geng, and M. Ren, "Effects of diamond tip orientation on the dynamic ploughing lithography of single crystal copper," *Precis. Eng.*, vol. 57, no. December 2018, pp. 127–136, 2019.

[131] H. Taha *et al.*, "Protein printing with an atomic force sensing nanofountainpen," *Appl. Phys. Lett.*, vol. 83, no. 5, pp. 1041–1043, 2003.

[132] J. Deng, L. Zhang, J. Dong, and P. H. Cohen, "AFM-based 3D Nanofabrication Using Ultrasonic Vibration Assisted Nanomachining," *Procedia Manuf.*, vol. 1, pp. 584–592, 2015.

[133] J. Deng, J. Dong, and P. Cohen, "High Rate 3D Nanofabrication by AFM-based Ultrasonic Vibration Assisted Nanomachining," *Procedia Manuf.*, vol. 5, pp. 1283–1294, 2016.

[134] J. C. Gartside *et al.*, "Realization of ground state in artificial kagome spin ice via topological defect-driven magnetic writing," *Nat. Nanotechnol.*, vol. 13, no. 1, pp. 53–58, 2018.

[135] M. Holz *et al.*, "Tip-based electron beam induced deposition using active cantilevers," *J. Vac. Sci. Technol. B*, vol. 37, no. 6, p. 061812, 2019.

[136] K. Utada, K. Ishida, M. Nakamura, Y. Morimoto, S. Yamashita, and T. Sakabe, "Nanofabrication by scanning probe microscope lithography: A review," *J. Vac. Sci. Technol. B*, vol. 53, no. 12, pp. 1396–1403, 2005.

[137] I. W. Rangelow *et al.*, "Review Article: Active scanning probes: A versatile toolkit for fast imaging and emerging nanofabrication," *J. Vac. Sci. Technol.*

B, Nanotechnol. Microelectron. Mater. Process. Meas. Phenom., vol. 35, no. 6, p. 06G101, 2017.

[138] A. A. Tseng, “Three-dimensional patterning of nanostructures using atomic force microscopes,” *J. Vac. Sci. Technol. B, Nanotechnol. Microelectron. Mater. Process. Meas. Phenom.*, vol. 29, no. 4, p. 040801, 2011.

[139] E. Rani and L. S. Wong, “High-Resolution Scanning Probe Nanolithography of 2D Materials: Novel Nanostructures,” *Adv. Mater. Technol.*, vol. 4, no. 7, 2019.

[140] A. A. Tseng, “Removing material using atomic force microscopy with single- and multiple-tip sources,” *Small*, vol. 7, no. 24, pp. 3409–3427, 2011.

[141] S. Goel, “An atomistic investigation on the nanometric cutting mechanism of hard, brittle materials,” Heriot-Watt University, 2013.

[142] K. M. Carroll *et al.*, “Parallelization of thermochemical nanolithography,” *Nanoscale*, vol. 6, no. 3, pp. 1299–1304, 2014.

[143] F. Hui and M. Lanza, “Scanning probe microscopy for advanced nanoelectronics,” *Nat. Eletronics*, pp. 221–229, 2019.

[144] M. Kaestner, M. Hofer, and I. W. Rangelow, “Nanolithography by scanning probes on calixarene molecular glass resist using mix-and-match lithography,” *J. Micro/Nanolithography, MEMS, MOEMS*, vol. 12, no. 3, p. 031111, 2013.

[145] S. Goel *et al.*, “Horizons of modern molecular dynamics simulation in digitalized solid freeform fabrication with advanced materials,” *Mater. Today Chem.*, vol. 18, p. 100356, 2020.

[146] Y. Yan, T. Sun, S. Dong, and Y. Liang, “Study on effects of the feed on AFM-based nano-scratching process using MD simulation,” *Comput. Mater. Sci.*, vol. 40, no. 1, pp. 1–5, 2007.

[147] R. Komanduri, N. Chandrasekaran, and L. M. Raff, “MD simulation of indentation and scratching of single crystal aluminum,” *Wear*, vol. 240, no. 1–2, pp. 113–143, 2000.

[148] D. Christopher, R. Smith, and A. Richter, “Atomistic modelling of nanoindentation in iron and silver,” *Nanotechnology*, vol. 12, no. 3, pp. 372–383, 2001.

[149] X. Liu, Z. Liu, and Y. Wei, “Ploughing friction and nanohardness dependent on the tip tilt in nano-scratch test for single crystal gold,” *Comput. Mater. Sci.*, vol. 110, pp. 54–61, 2015.

[150] H. Dai, S. Li, and G. Chen, “Molecular dynamics simulation of subsurface damage mechanism during nanoscratching of single crystal silicon,” *Proc. Inst. Mech. Eng. Part J J. Eng. Tribol.*, vol. 0, no. 0, pp. 1–13, 2018.

[151] Y. Liu, B. Li, and L. Kong, “A molecular dynamics investigation into nanoscale scratching mechanism of polycrystalline silicon carbide,” *Comput. Mater. Sci.*, vol. 148, pp. 76–86, 2018.

[152] D. Yuan, P. Zhu, F. Fang, and C. Qiu, “Study of nanoscratching of polymers by using molecular dynamics simulations,” *Sci. China Physics, Mech. Astron.*, vol. 56, no. 9, pp. 1760–1769, 2013.

[153] Q. Zhang, D. Diao, and M. Kubo, “Nanoscratching of multi-layer graphene by molecular dynamics simulations,” *Tribol. Int.*, vol. 88, pp. 85–88, 2015.

[154] Y. Geng, J. Zhang, Y. Yan, B. Yu, L. Geng, and T. Sun, “Experimental and theoretical investigation of crystallographic orientation dependence of nanoscratching of single crystalline copper,” *PLoS One*, vol. 10, no. 7, pp. 1–15, 2015.

[155] X. L. Junjie Zhang, Tao Sun, Yongda Yan, Dong Shen, “Atomistic investigation of scratching- induced deformation twinning in nanocrystalline Cu,” *J. Appl. Phys.*, vol. 073526, no. September 2012, 2012.

[156] A. Noreyan, J. G. Amar, and I. Marinescu, “Molecular dynamics simulations of nanoindentation of β-SiC with diamond indenter,” *Mater. Sci. Eng. B Solid-State Mater. Adv. Technol.*, vol. 117, no. 3, pp. 235–240, 2005.

[157] S. Goel, W. Bin Rashid, X. Luo, A. Agrawal, and V. K. Jain, “A theoretical assessment of surface defect machining and hot machining of nanocrystalline silicon carbide,” *J. Manuf. Sci. Eng. Trans. ASME*, vol. 136, no. 2, pp. 1–12, 2014.

[158] S. Z. Chavoshi and X. Luo, “Molecular dynamics simulation study of deformation mechanisms in 3C-SiC during nanometric cutting at elevated temperatures,” *Mater. Sci. Eng. A*, vol. 654, pp. 400–417, 2016.

[159] S. Z. Chavoshi and X. Luo, “Atomic-scale characterization of occurring phenomena during hot nanometric cutting of single crystal 3C-SiC,” *RSC Adv.*, vol. 6, no. 75, pp. 71409–71424, 2016.

[160] S. Z. Chavoshi, S. Goel, and X. Luo, “Molecular dynamics simulation investigation on the plastic flow behaviour of silicon during nanometric cutting,” *Model. Simul. Mater. Sci. Eng.*, vol. 24, no. 1, 2015.

[161] S. Z. Chavoshi and X. Luo, “An atomistic simulation investigation on chip related phenomena in nanometric cutting of single crystal silicon at elevated temperatures,” *Comput. Mater. Sci.*, vol. 113, pp. 1–10, 2016.

[162] S. Z. Chavoshi, S. Goel, and X. Luo, “Influence of temperature on the anisotropic cutting behaviour of single crystal silicon: A molecular dynamics simulation investigation,” *J. Manuf. Process.*, vol. 23, pp. 201–210, Aug. 2016.

[163] S. Z. Chavoshi, S. Xu, and X. Luo, “Dislocation-mediated plasticity in silicon during nanometric cutting: A molecular dynamics simulation study,” *Mater. Sci. Semicond. Process.*, vol. 51, pp. 60–70, 2016.

[164] H. W. Schumacher, U. F. Keyser, U. Zeitler, R. J. Haug, and K. Eberl, “Controlled mechanical AFM machining of two-dimensional electron systems: Fabrication of a single-electron transistor,” *Phys. E Low-Dimensional Syst. Nanostructures*, vol. 6, no. 1, pp. 860–863, 2000.

[165] M. Versen, B. Klehn, U. Kunze, D. Reuter, and A. D. Wieck, “Nanoscale devices fabricated by direct machining of GaAs with an atomic force microscope,” *Ultramicroscopy*, vol. 82, no. 1–4, pp. 159–163, 2000.

[166] S. Goel, X. Luo, A. Agrawal, and R. L. Reuben, “Diamond machining of silicon: A review of advances in molecular dynamics simulation,” *Int. J. Mach. Tools Manuf.*, vol. 88, pp. 131–164, 2015.

[167] P. Hirel, “Atomsk: A tool for manipulating and converting atomic data files,” *Comput. Phys. Commun.*, vol. 197, pp. 212–219, 2015.

[168] G. Lejeune Dirichlet, “Über die Reduction der positiven quadratischen Formen mit drei unbestimmten ganzen Zahlen.,” *J. für die reine und Angew. Math.*, vol. 40, pp. 209–227, 1850.

[169] G. Voronoi, “Nouvelles applications des paramètres continus à la théorie des formes quadratiques. Deuxième mémoire. Recherches sur les parallélloèdres primitifs,” *J. für die reine und Angew. Math.*, vol. 1908, no. 134, pp. 198–208, 2009.

[170] S. Nose, “A unified formulation of the constant temperature molecular-dynamics methods,” *J. Chem. Phys.*, vol. 81, pp. 511–519, 1984.

[171] S. J. Plimpton, “Fast parallel algorithms for short range molecular dynamics,” *J. Comput. Phys.*, vol. 117, pp. 1–19, 1995.

[172] J. Tersoff, “Modeling solid-state chemistry: Interatomic potentials for multicomponent systems,” *Phys. Rev. B*, vol. 39, no. 8, pp. 5566–5568, 1989.

[173] D. K. Ward, X. W. Zhou, B. M. Wong, F. P. Doty, and J. A. Zimmerman, “Analytical bond-order potential for the cadmium telluride binary system,” *Phys. Rev. B - Condens. Matter Mater. Phys.*, vol. 85, no. 11, pp. 1–19, 2012.

[174] D. G. Pettifor and I. I. Oleinik, “Analytic bond-order potential for open and close-packed phases,” *Phys. Rev. B - Condens. Matter Mater. Phys.*, vol. 65, no. 17, pp. 1–4, 2002.

[175] L. Goodwin, C. M. Goringe, D. R. Bowler, A. P. Sutton, and M. W. Finnis, “Generating Transferable Tight-Binding Parameters: Application to Silicon,” *Europhys. Lett.*, vol. 9, no. 7, pp. 701–706, 1989.

[176] J. F. Ziegler, M. D. Ziegler, and J. P. Biersack, “SRIM - The stopping and range of ions in matter (2010),” *Nucl. Instruments Methods Phys. Res. Sect. B Beam Interact. with Mater. Atoms*, vol. 268, no. 11–12, pp. 1818–1823, 2010.

[177] D. T. Infield *et al.*, “Main-chain mutagenesis reveals intrahelical coupling in an ion channel voltage-sensor,” *Nat. Commun.*, vol. 9, no. 1, pp. 1–10, 2018.

[178] A. Stukowski, “Visualization and analysis of atomistic simulation data with OVITO-the Open Visualization Tool,” *Model. Simul. Mater. Sci. Eng.*, vol. 18, no. 1, 2010.

[179] A. Stukowski and K. Albe, “Extracting dislocations and non-dislocation crystal defects from atomistic simulation data,” *Model. Simul. Mater. Sci. Eng.*, vol. 18, no. 085001, p. 13pp, 2010.

[180] A. Stukowski, V. V. Bulatov, and A. Arsenlis, “Automated identification and indexing of dislocations in crystal interfaces,” *Model. Simul. Mater. Sci. Eng.*, vol. 20, no. 8, 2012.

[181] A. Stukowski and A. Arsenlis, “On the elastic – plastic decomposition of crystal deformation at the atomic scale,” *Model. Simul. Mater. Sci. Eng.*, vol. 20, no. 035012, p. 18pp, 2012.

[182] A. Stukowski, J. Markmann, and J. Weissmu, “Atomistic origin of microstrain broadening in diffraction data of nanocrystalline solids,” *Acta Mater.*, vol. 57, pp. 1648–1654, 2009.

[183] J. Wang, X. Zhang, and F. Fang, “Molecular dynamics study on nanometric cutting of ion implanted silicon,” *Comput. Mater. Sci.*, vol. 117, pp. 240–250, 2016.

[184] S. Goel, W. Bin Rashid, X. Luo, A. Agrawal, and V. K. Jain, “A Theoretical Assessment of Surface Defect Machining and Hot Machining of Nanocrystalline Silicon Carbide,” *J. Manuf. Sci. Eng.*, vol. 136, no. 2, p. 021015, 2014.

[185] P. A. Romero, G. Anciaux, A. Molinari, and J. F. Molinari, “Insights into the thermo-mechanics of orthogonal nanometric machining,” *Comput. Mater. Sci.*, vol. 72, pp. 116–126, 2013.

[186] X. Q. B. Liu, “How to compute the atomic stress objectively?,” *J. Comput. Theor. Nanosci.*, vol. 6, no. 5, pp. 1081–1089, 2009.

[187] H. Dai, G. Chen, C. Zhou, Q. Fang, and X. Fei, “A numerical study of ultraprecision machining of monocrystalline silicon with laser nano-structured diamond tools by atomistic simulation,” *Appl. Surf. Sci.*, vol. 393, pp. 405–416, 2017.

[188] Y. S. Noriyuki Miyazaki, “Calculation of Mechanical Properties of Solids Using Molecular Dynamics Method,” *JSME Int. journal. Ser. A, Mech. Mater. Eng.*, vol. 39, no. 4, pp. 606–612, 1996.

[189] F. Wakai, Y. Shinoda, and T. Akatsu, “Tensor-virial equation for deformation of a particle in viscous sintering,” *J. Am. Ceram. Soc.*, vol. 95, no. 9, pp. 2785–2787, 2012.

[190] T. W. Lion and R. J. Allen, “Computing the local pressure in molecular dynamics simulations,” *J. Phys. Condens. Matter*, vol. 24, no. 28, pp. 1–6, 2012.

[191] S. Goel, A. Kovalchenko, A. Stukowski, and G. Cross, “Influence of microstructure on the cutting behaviour of silicon,” *Acta Mater.*, vol. 105, pp. 464–478, 2016.

[192] P. N. Blake and R. O. Scattergood, “Ductile-Regime Machining of Germanium and Silicon,” *J. Am. Ceram. Soc.*, vol. 73, no. 4, pp. 949–957, 1990.

[193] Z. Li and X. Zhang, “Subsurface deformation of germanium in ultra-precision cutting: characterization of micro-Raman spectroscopy,” *Int. J. Adv. Manuf. Technol.*, vol. 91, no. 1–4, pp. 213–225, 2017.

[194] S. Goel, X. Luo, and R. L. Reuben, “Wear mechanism of diamond tools against single crystal silicon in single point diamond turning process,” *Tribol. Int.*, vol. 57, pp. 272–281, 2013.

[195] S. Goel, X. Luo, P. Comley, R. L. Reuben, and A. Cox, “Brittle-ductile transition during diamond turning of single crystal silicon carbide,” *Int. J. Mach. Tools Manuf.*, vol. 65, pp. 15–21, 2013.

[196] A. Mir, X. Luo, K. Cheng, and A. Cox, “Investigation of influence of tool rake angle in single point diamond turning of silicon,” *Int. J. Adv. Manuf. Technol.*, vol. 94, no. 5–8, pp. 2343–2355, 2018.

[197] R. G. Jasinevicius, “Influence of cutting conditions scaling in the machining of semiconductors crystals with single point diamond tool,” *J. Mater. Process. Technol.*, vol. 179, no. 1–3, pp. 111–116, 2006.

[198] Z. Tong, Y. Liang, X. Jiang, and X. Luo, “An atomistic investigation on the mechanism of machining nanostructures when using single tip and multi-tip diamond tools,” *Appl. Surf. Sci.*, vol. 290, pp. 458–465, 2014.

[199] A. N. Gulluoglu and C. T. Tsai, “Dislocation generation in GaAs crystals grown by the vertical gradient freeze method,” *J. Mater. Process. Technol.*, vol. 102, no. 1, pp. 179–187, 2000.

[200] F. M. Kiessling, M. Albrecht, K. Irmscher, R. Krause-Rehberg, W. Ulrici, and P. Rudolph, “Defect distribution in boron-reduced GaAs crystals grown by vapour-pressure-controlled Czochralski technique,” *J. Cryst. Growth*, vol. 310, no. 7–9, pp. 1418–1423, 2008.

[201] R. K. Ahrenkiel, S. W. Johnston, B. M. Keyes, and D. J. Friedman, “Transport properties of GaAs1-xNx thin films grown by metalorganic chemical vapor deposition,” *Appl. Phys. Lett.*, vol. 77, no. 23, pp. 3794–3796, 2000.

[202] S. Zhou, L. Ai, M. Qi, S. Wang, A. Xu, and Q. Guo, “Bi-induced highly n-type carbon-doped InGaAsBi films grown by molecular beam epitaxy,” *J. Mater. Sci.*, vol. 53, no. 5, pp. 3537–3543, 2018.

[203] S. Blin *et al.*, “Wireless communication at 310 GHz using GaAs high-electron-mobility transistors for detection,” *J. Commun. Networks*, vol. 15, no. 6, pp. 559–568, 2013.

[204] K. Alberi, B. Fluegel, H. Moutinho, R. G. Dhere, J. V Li, and A. Mascarenhas, “Measuring long-range carrier diffusion across multiple grains in polycrystalline semiconductors by photoluminescence imaging,” *Nat. Commun.*, pp. 1–7, 2013.

[205] D. M. Wilt, M. A. Smith, W. Maurer, D. Scheiman, and P. P. Jenkins, “GaAs photovoltaics on polycrystalline Ge substrates,” *Conf. Rec. 2006 IEEE 4th World Conf. Photovolt. Energy Conversion, WCPEC-4*, vol. 2, no. June 2006, pp. 1891–1894, 2006.

[206] M. Yamaguchi and Y. Itoh, “Efficiency considerations for polycrystalline GaAs thin-film solar cells,” *J. Appl. Phys.*, vol. 60, no. 1, pp. 413–417, 1986.

[207] M. K. Sharma and D. P. Joshi, “Electrical conduction model for polycrystalline GaAs films,” *J. Appl. Phys.*, vol. 102, no. 3, pp. 1–8, 2007.

[208] M. Imaizumi *et al.*, “Low-temperature growth of GaAs polycrystalline films on glass substrates for space solar cell application,” *J. Cryst. Growth*, vol. 221, no. 1–4, pp. 688–692, 2000.

[209] J. C. Bourgoin, “Polycrystalline GaAs for large area imaging detectors,” *Nucl. Instruments Methods Phys. Res. Sect. A Accel. Spectrometers, Detect. Assoc. Equip.*, vol. 466, no. 1, pp. 9–13, 2001.

[210] J. H. Epple, K. L. Chang, C. F. Xu, G. W. Pickrell, K. Y. Cheng, and K. C. Hsieh, “Formation of highly conductive polycrystalline GaAs from annealed amorphous (Ga,As),” *J. Appl. Phys.*, vol. 93, no. 9, pp. 5331–5336, 2003.

[211] J. D. Song, W. J. Choi, J. I. Lee, J. M. Kim, K. S. Chang, and Y. T. Lee, “Optical and structural properties of InGaAs/InP double quantum wells grown by molecular beam epitaxy with polycrystalline GaAs and GaP decomposition sources,” *Phys. E Low-Dimensional Syst. Nanostructures*, vol. 32, no. 1-2 SPEC. ISS., pp. 234–236, 2006.

[212] S. Z. Chavoshi, S. Xu, and S. Goel, “Addressing the discrepancy of finding the equilibrium melting point of silicon using molecular dynamics simulations,” *Proc. R. Soc. A Math. Phys. Eng. Sci.*, vol. 473, no. 2202, pp. 1–9, 2017.

[213] S. Goel, N. Haque Faisal, X. Luo, J. Yan, and A. Agrawal, “Nanoindentation of polysilicon and single crystal silicon: Molecular dynamics simulation and experimental validation,” *J. Phys. D. Appl. Phys.*, vol. 47, no. 27, 2014.

[214] S. Goel, J. Yan, X. Luo, and A. Agrawal, “Incipient plasticity in 4H-SiC during quasistatic nanoindentation,” *J. Mech. Behav. Biomed. Mater.*, vol. 34, pp. 330–337, 2014.

[215] E. Maras, O. Trushin, A. Stukowski, T. Ala-Nissila, and H. Jónsson, “Global transition path search for dislocation formation in Ge on Si(001),” *Comput. Phys. Commun.*, vol. 205, pp. 13–21, 2016.

[216] S. Goel and A. Stukowski, “Comment on ‘incipient plasticity of diamond during nanoindentation’ by C. Xu, C. Liu and H. Wang,: RSC Advances, 2017, 7, 36093,” *RSC Adv.*, vol. 8, no. 10, pp. 5136–5137, 2018.

[217] Z. Li and R. C. Picu, “Shuffle-glide dislocation transformation in Si,” *J. Appl. Phys.*, vol. 113, no. 8, pp. 1–7, 2013.

[218] S. H. He, B. B. He, K. Y. Zhu, and M. X. Huang, “Evolution of dislocation density in bainitic steel: Modeling and experiments,” *Acta Mater.*, vol. 149, pp. 46–56, 2018.

[219] S. Goel, “The current understanding on the diamond machining of silicon carbide,” *J. Phys. D. Appl. Phys.*, vol. 47, no. 24, 2014.

[220] R. Komanduri and N. Chandrasekaran, “Molecular dynamics simulations of atomic-scale friction,” *Phys. Rev. B*, vol. 61, no. 20, pp. 167–172, 2000.

[221] S. Goel, A. Stukowski, X. Luo, A. Agrawal, and R. L. Reuben, “Anisotropy of single-crystal 3C-SiC during nanometric cutting,” *Model. Simul. Mater. Sci. Eng.*, vol. 21, no. 6, 2013.

[222] J. Qu, P. J. Blau, T. R. Watkins, O. B. Cavin, and N. S. Kulkarni, “Friction and wear of titanium alloys sliding against metal, polymer, and ceramic counterfaces,” *Wear*, vol. 258, no. 9, pp. 1348–1356, 2005.

[223] M. Z. Butt, M. Khaleeq-Ur-Rahman, and D. Ali, “Kinetics of flow stress in ultra-pure tantalum single crystals in stress/temperature regime III,” *J. Mater. Sci.*, vol. 45, no. 22, pp. 6046–6051, 2010.

[224] S. V. Prasad, J. R. Michael, C. C. Battaile, B. S. Majumdar, and P. G. Kotula, “Tribology of single crystal nickel: Interplay of crystallography, microstructural evolution, and friction,” *Wear*, vol. 458–459, no. July, p. 203320, 2020.

[225] R. Takagi and Y. Tsuya, “Static friction between clean copper single crystal surfaces,” *Wear*, vol. 4, no. 3, pp. 216–227, 1961.

[226] D. Gu, L. Zhang, S. Chen, K. Song, and S. Liu, “Significant reduction of the friction and wear of PMMA based composite by filling with PTFE,” *Polymers (Basel).*, vol. 10, no. 9, 2018.

[227] H. T. Liu, M. H. Zhao, C. Lu, and J. W. Zhang, “Characterization on the yield stress and interfacial coefficient of friction of glasses from scratch tests,” *Ceram. Int.*, vol. 46, no. 5, pp. 6060–6066, 2020.

[228] C. Chen, M. Lai, and F. Fang, “Study on the Crack Formation Mechanism in Nano-cutting of Gallium Arsenide,” *Appl. Surf. Sci.*, vol. 540, no. P2, p. 148322, 2020.

[229] Y. H. Chen, H. Huang, M. Y. Lu, Y. Q. Wu, F. Z. Fang, and X. T. Hu, “Molecular Dynamics Simulation of the Deformation of Single Crystal Gallium Arsenide,” *Appl. Mech. Mater.*, vol. 553, pp. 60–65, 2014.

[230] D. Yi, J. Li, and P. Zhu, “Study of Nanoscratching Process of GaAs Using Molecular Dynamics,” *Crystals*, vol. 8, no. 8, p. 321, 2018.

[231] R. S. J. Al-Musawi, E. B. Brousseau, Y. Geng, and F. M. Borodich, “Insight into mechanics of AFM tip-based nanomachining: Bending of cantilevers and machined grooves,” *Nanotechnology*, vol. 27, no. 38, 2016.

[232] S. Goel, F. D. Martinez, S. Z. Chavoshi, N. Khatri, and C. Giusca, “Molecular dynamics simulation of the elliptical vibration-assisted machining of pure iron,” *J. Micromanufacturing*, vol. 1, no. 1, pp. 6–19, 2018.

[233] Y. Pan *et al.*, “New insights into the methods for predicting ground surface roughness in the age of digitalisation,” *Precis. Eng.*, vol. 67, no. October 2020, pp. 393–418, 2021.

[234] G. E. Dieter, “Mechanical Metallurgy,” *McGraw-Hill B. Co., New York*, 1986.

[235] T. H. Fang, W. J. Chang, and C. M. Lin, “Nanoindentation and nanoscratch characteristics of Si and GaAs,” *Microelectron. Eng.*, vol. 77, no. 3–4, pp. 389–398, 2005.

[236] F. Ericson, S. Johansson, and J. Å. Schweitz, “Hardness and fracture toughness of semiconducting materials studied by indentation and erosion techniques,” *Mater. Sci. Eng.*, vol. 105–106, no. PART 1, pp. 131–141, 1988.

[237] L. Xu, L. Kong, H. Zhao, S. Wang, S. Liu, and L. Qian, “Mechanical behavior of undoped n-type GaAs under the indentation of berkovich and flat-tip indenters,” *Materials (Basel).*, vol. 12, no. 7, pp. 1–10, 2019.

[238] D. Chrobak, M. Trebala, A. Chrobak, and R. Nowak, “Origin of Nanoscale Incipient Plasticity in GaAs and InP Crystal,” *Crystals*, 2019.

[239] S. Ono and T. Kikegawa, “Phase transformation of GaAs at high pressures and temperatures,” *J. Phys. Chem. Solids*, vol. 113, pp. 1–4, 2018.

[240] J. M. Besson, J. P. Itié, A. Polian, G. Weill, J. L. Mansot, and J. Gonzalez, “High-pressure phase transition and phase diagram of gallium arsenide,” *Phys. Rev. B*, vol. 44, no. 9, pp. 4214–4234, 1991.

[241] S. V. Ovsyannikov and V. V. Shchennikov, “Observation of a new high-pressure semimetal phase of GaAs from pressure dependence of the thermopower,” *J. Phys. Condens. Matter*, vol. 18, no. 42, pp. 2–9, 2006.

[242] Y. Geng *et al.*, “Processing outcomes of the AFM probe-based machining approach with different feed directions,” *Precis. Eng.*, vol. 46, pp. 288–300, 2016.

[243] A. Mir, X. Luo, and J. Sun, “The investigation of influence of tool wear on ductile to brittle transition in single point diamond turning of silicon,” *Wear*, vol. 364–365, pp. 233–243, 2016.

[244] S. Saketi, U. Bexell, J. Östby, and M. Olsson, “On the diffusion wear of cemented carbides in the turning of AISI 316L stainless steel,” *Wear*, vol. 430–431, no. March, pp. 202–213, 2019.

[245] B. M. Lane, T. A. Dow, and R. Scattergood, “Thermo-chemical wear model and worn tool shapes for single-crystal diamond tools cutting steel,” *Wear*, vol. 300, no. 1–2, pp. 216–224, 2013.

[246] M. Binder, F. Klocke, and B. Doebbeler, “Abrasive wear behavior under metal cutting conditions,” *Wear*, vol. 376–377, pp. 165–171, 2017.

[247] L. Zou, J. Yin, Y. Huang, and M. Zhou, “Essential causes for tool wear of single crystal diamond in ultra-precision cutting of ferrous metals,” *Diam. Relat. Mater.*, vol. 86, no. 174, pp. 29–40, 2018.

[248] G. Li, M. Zula, W. Pan, C. Wen, and S. Ding, “The manufacturing and the application of polycrystalline diamond tools – A comprehensive review,” *J. Manuf. Process.*, vol. 56, pp. 400–416, 2020.

[249] M. Ganchenkova and R. M. Nieminen, *Mechanical Properties of Silicon Microstructures*. Elsevier Inc., 2015.

[250] N. Adachi, N. Wu, Y. Todaka, H. Sato, and R. Ueji, “Phase transformation in Fe - Mn – C alloys by severe plastic deformation under high pressure,” *Mater. Lett.*, vol. 185, pp. 109–111, 2016.

[251] J. Gasc *et al.*, “High-pressure, high-temperature plastic deformation of sintered diamonds,” *Diam. Relat. Mater.*, vol. 59, pp. 95–103, 2015.

[252] S. Goel, X. Luo, and R. L. Reuben, “Molecular dynamics simulation model for the quantitative assessment of tool wear during single point diamond turning of cubic silicon carbide,” *Comput. Mater. Sci.*, vol. 51, no. 1, pp. 402–408, 2012.

[253] A. Silverman, J. Adler, and R. Kalish, “Diamond membrane surface after ion-implantation-induced graphitization for graphite removal: Molecular dynamics simulation,” *Phys. Rev. B - Condens. Matter Mater. Phys.*, vol. 83, no. 22, pp. 1–9, 2011.

[254] K. Cheng, X. Luo, R. Ward, and R. Holt, “Modeling and simulation of the tool wear in nanometric cutting,” *Wear*, vol. 255, no. 7–12, pp. 1427–1432, 2003.

[255] Y. G. Gogotsi, A. Kailer, and K. G. Nickel, “Transformation of diamond to graphite,” *Nature*, vol. 401, no. 6754, pp. 663–664, 1999.

[256] M. Popov, “Stress-induced phase transitions in diamond,” *High Press. Res.*, vol. 30, no. 4, pp. 670–678, 2010.

[257] H. Chacham and L. Kleinman, “Instabilities in diamond under high shear stress,” *Phys. Rev. Lett.*, vol. 85, no. 23, pp. 4904–4907, 2000.

[258] A. D. Freed, “Hencky strain and logarithmic rates in Lagrangian analysis,” *Int. J. Eng. Sci.*, vol. 81, pp. 135–145, 2014.

[259] G. L. W. Cross, “Silicon nanoparticles: Isolation leads to change,” *Nat. Nanotechnol.*, vol. 6, no. 8, pp. 467–468, 2011.

[260] S. Goel, X. Luo, R. L. Reuben, and H. Pen, “Influence of temperature and crystal orientation on tool wear during single point diamond turning of silicon,” *Wear*, vol. 284–285, pp. 65–72, 2012.

[261] N. S. Xu, J. Chen, and S. Z. Deng, “Effect of heat treatment on the properties of nano-diamond under oxygen and argon ambient,” *Diam. Relat. Mater.*, vol. 11, no. 2, pp. 249–256, 2002.

[262] K. Maekawa and A. Itoh, “Friction and tool wear in nano-scale machining-a molecular dynamics approach,” *Wear*, vol. 188, pp. 115–122, 1995.

[263] I. Durazo-Cardenas, P. Shore, X. Luo, T. Jacklin, S. A. Impey, and A. Cox, “3D characterisation of tool wear whilst diamond turning silicon,” *Wear*, vol. 262, no. 3–4, pp. 340–349, 2007.

[264] F. Ericson, S. Johansson, and J.-Å. Schweitz, “Hardness and fracture toughness of semiconducting materials studied by indentation and erosion techniques,” *Mater. Sci. Eng. A*, vol. 105–106, no. Part 1, pp. 131–141, 1988.

[265] H. Huang, B. R. Lawn, R. F. Cook, and D. B. Marshall, “Critique of materials-based models of ductile machining in brittle solids,” *J. Am. Ceram. Soc.*, vol. 103, no. 11, pp. 6096–6100, 2020.

[266] N. Huang, Y. Yan, P. Zhou, R. Kang, D. Guo, and S. Goel, “Elastic recovery of monocrystalline silicon during ultra-fine rotational grinding,” *Precis. Eng.*, vol. 65, no. February, pp. 64–71, 2020.

[267] S. Z. Chavoshi, “An investigation on the mechanics of nanometric cutting for hard- brittle materials at elevated temperatures,” University of Strathclyde, 2016.

[268] S. Goel, A. Stukowski, G. Goel, X. Luo, and R. L. Reuben, “Nanotribology at high temperatures,” *Beilstein J. Nanotechnol.*, pp. 586–588, 2012.

[269] D. Ceresoli and E. Tosatti, “Peak Effect versus Skating in High Temperature Nanofriction,” *Nat. Mater.*, vol. 6, no. 3, pp. 230–234, 2007.

[270] F. Shimizu, S. Ogata, and J. Li, “Theory of shear banding in metallic glasses and molecular dynamics calculations,” *Mater. Trans.*, vol. 48, no. 11, pp. 2923–2927, 2007.

[271] M. L. Falk and J. S. Langer, “Dynamics of viscoplastic deformation in amorphous solids,” *Phys. Rev. E*, vol. 57, no. 6, p. 14, 1998.

[272] S. Goel, N. H. Faisal, V. Ratia, A. Agrawal, and A. Stukowski, “Atomistic investigation on the structure-property relationship during thermal spray nanoparticle impact,” *Comput. Mater. Sci.*, vol. 84, pp. 163–174, 2014.

[273] D. A. Murdick, X. W. Zhou, H. N. G. Wadley, D. Nguyen-Manh, R. Drautz, and D. G. Pettifor, “Analytic bond-order potential for the gallium arsenide

system," *Phys. Rev. B - Condens. Matter Mater. Phys.*, vol. 73, no. 4, pp. 1–20, 2006.